Università della Calabria

Dipartimento di Fisica

UNIVERSITÀ DELLA CALABRIA

Dottorato di ricerca in

Scienze e Tecnologie Fisiche, Chimiche e dei Materiali

Ciclo XXXIV

Ph.D. Thesis

Multifunctional mesogenic microparticles: optomechanics and photonics

Settore Scientifico-Disciplinare: FIS/07

Coordinatrice: Ch.ma Prof.ssa Gabriella Cipparrone

Firma oscurata in base alle linee guida del Garante della privacy

Supervisori: Dott. Alfredo Mazzulla e Prof. Pasquale Pagliusi

Firma oscurata in base alle linee guida del Garante della privacy

Candidato: Dott. Nicola Pellizzi

Firma oscurata in base alle linee guida del Garante della privacy

Università della Calabria

Dipartimento di Fisica

UNIVERSITÀ DELLA CALABRIA

Dottorato di ricerca in

Scienze e Tecnologie Fisiche, Chimiche e dei Materiali

Ciclo XXXIV

Ph.D. Thesis

Multifunctional mesogenic microparticles: optomechanics and photonics

Settore Scientifico-Disciplinare: FIS/07

Coordinatrice: Ch.ma Prof.ssa Gabriella Cipparrone

Supervisori: Dott. Alfredo Mazzulla e Prof. Pasquale Pagliusi

Candidato: Dott. Nicola Pellizzi

Ad Angioletta

Prefazione

Nel corso degli anni di studio e ricerche del percorso di dottorato, ho avuto la fortuna di esplorare e apprezzare il campo della fotonica. L'aspetto che più mi ha affascinato è stato l'inusuale oltre che difficile da esplorare, capacità di trasferimento di quantità di moto e momento angolare tra luce e materia. Nel corso dei secoli questo fenomeno appassionò molti grandi scienziati, a iniziare da I. Newton per finire al recente premio Nobel A. Ashkin. Il percorso che ha portato a definire e utilizzare queste potenzialità è stato molto arduo per via delle forze di piccola entità e diversa natura in gioco. Questo fenomeno dapprima è stato solo teorizzato matematicamente da J. C. *Maxwell* per poi essere osservato nella coda secondaria delle comete che transitano vicine al sole. Ma è solo nella seconda metà del 900, con l'avvento dei laser e con l'intuizione di Ashkin di focalizzarlo all'interno di un microscopio, che si è potuto studiare in maniera sistematica questo tipo di interazione. Da qui è nata tutta una branca, l'optomeccanica è diventata progressivamente sempre più sofisticata.

Ringraziamenti

Vorrei ringraziare tutte le persone che ho incontrato lungo il mio percorso di dottorato all'Università della Calabria. Va a ciascuno di loro la mia gratitudine perché ognuno a suo modo ha contribuito in maniera positiva alla mia crescita.

In particolare, voglio esprimere tutta la mia riconoscenza e affetto per la Prof.ssa Gabriella Cipparrone, il Dott. Alfredo Mazzulla ed il Prof. Pasquale Pagliusi, le persone con cui ho lavorato tutti i giorni per tre anni, che ritengo un po' la mia famiglia cosentina e che grazie alla loro sapiente guida, dedizione e abilità nella ricerca mi hanno introdotto e fatto innamorare del mondo della Fotonica. Il loro incessante impegno nei miei confronti ha fatto in modo che si superassero i momenti di impasse sempre in maniera brillante e istruttiva.

Un ringraziamento speciale va al Dott. Biagio Audia, compagno di laboratorio che ha saputo alleggerire le giornate di lavoro, portando idee, spunti e tanta allegria sempre comodi per accendere un faro nella mente in un laboratorio di fotonica tipicamente sempre al buio.

Inoltre, è doveroso per me ringraziare la mia famiglia, i miei genitori, mia sorella e mio fratello, costantemente presenti e sempre pronti a venirmi in aiuto favorendo ogni mia scelta.

É con stima e amicizia che ringrazio Rosalba, Bruno, Sasà, Claudia, Marcella, Luisa, Pierpaolo, Mek, Domenico, Sonia, Federica, Ciccio, Giancarlo, Cristian, Alessandro, Nicola e l'infinita lista di amici del collettivo Azadì e della Agiuropicala, le persone che mi hanno accolto con sincera amicizia quando sono arrivato a Rende per la prima volta e mi hanno costantemente tenuto di buon umore.

Chiudo esprimendo tutto il mio amore e la mia gratitudine per Agar, per il suo amore e per il suo aiuto, per la sua capacità di riuscire a spingermi sempre oltre il mio limite e per avermi sostenuto nella scelta di intraprendere questo percorso nonostante ciò significasse vivere lontani.

Abstract

The development of efficient and cost-effective micromachines is a challenge for applied and fundamental science given their wide fields of interest. Light has become a suitable tool to move small objects in a non-contact way, given its capabilities in exerting forces and torques. However, when complex machining is required, the assembly of micro-objects with proper architecture able to play a specific role in the dynamics, is extremely helpful.

To this aim, the design of opto-responsive micrometric devices was carried out by exploiting the dielectric-metal coupling. Such structures are able to couple with different forces carried by the optical field, and selectively acquire orbital and rotational momentum, depending on the presence of a raspberry-like gold nanoparticles shell.

Furthermore, the particles can have a chiral supramolecular structure due to the cholesteric nature of the mesogenic precursor. This allows the study of collective optomechanical phenomena and to the use of these as laser resonance cavities. The study, therefore, of how these microparticles under appropriate structures of the field are able to couple with it, giving rise to the birth of collective phenomena of angular momentum transfer.

The addition of fluorescent molecules in the polymeric core enables laser emission and demonstrate higher resistance to degradation of the core-shell particles, which represents the current limit of similar organic microresonators. Bragg and whispering gallery emissive modes were observed and an increase in operating cycles was obtained.

The thesis is completed with a detailed part concerning the production protocol and variants useful for obtaining versatile structures in both photonic and optomechanical fields. A profound characterization was carried out in order to appropriately exploit the different properties offered by this technology.

Riassunto

Lo sviluppo di micromacchine efficienti ed economiche è una sfida per la scienza di base e applicata offre un largo ventaglio di utilizzo. La luce è diventata un uno strumento efficiente per muovere piccoli oggetti senza contatto, capace di imprimere forze e momenti a questi oggetti. Tuttavia, quando sono richieste lavorazioni complesse, l'assemblaggio di microoggetti con una corretta architettura in grado di svolgere un ruolo specifico nella dinamica, è estremamente utile.

Per fare ciò si è provveduto alla progettazione di dispositivi micrometrici optoresponsivi sfruttando l'accoppiamento dielettrico-metallo. Tali strutture sono in grado di accoppiarsi con differenti forze indotte dal campo ottico, e acquisire selettivamente momento orbitale e di spin. Questo è dovuto alla presenza o meno di un guscio *raspberry-like* in oro.

Le particelle realizzate possono disporre di una struttura supramolecolare chirale dovuta alla loro natura colesterica. Ciò permette di accedere allo studio di fenomeni collettivi optomeccanici e all'utilizzo di queste come microcavità risonanti per emissione laser. È riportato lo studio, dunque, di come queste microparticelle sotto opportune strutturazioni del campo riescono ad accoppiarsi con esso dando origine alla nascita di fenomeni collettivi di trasferimento di momento angolare.

Grazie all'impiego di molecole fluorescenti è stato possibile verificare l'emissione laser e le migliorate capacità di resistenza alla degradazione in particelle core-shell, limite attuale di questo tipo di strutture. Si sono osservati modi emissivi alla Bragg e di tipo WGM e si è ottenuto un aumento dei cicli di funzionamento.

La tesi si completa con una dettagliata sezione che riguarda il protocollo di produzione ed alcune sue varianti utili a ottenere strutture versatili in campo sia fotonico che

optomeccanico. Una profonda caratterizzazione è stata effettuata al fine di sfruttare in maniera opportune le diverse proprietà offerte da questa tecnologia.

Table of Contents

Introduction

Micro and nanoparticles possess some advantages compared to large scale particles or bulk materials due to their high surface to volume ratio. Indeed, they have become an important class of materials for both everyday applications and basic research, while the increasing area of usage has led to new demands for tailored preparation with controlled size, functionalities, and morphologies. In the meantime, these structures have found widespread applications in materials science, in biomedical and pharmaceutical fields [1-5] as well as imaging, sensing, photonics [6-12].

Core-shell structures are a class of particles whose design provides the opportunity to acquire features and properties not achievable by the individual materials of the core and the shell [13-17]. Micro and nano core-shell particles have demonstrated unique properties resulting from the proper combination of outer (shell) and inner (core) materials and the size control of these structures [13-23]. By selecting the materials of the core and the shell, chemical, magnetic, and optical properties of these microparticles can be affected and finely tuned.

A variety of materials has been exploited for the core taking into account their chemical and physical features as important factors for specific applications, compatibility, environmental condition, delivery and release of molecules. The core material can be liquid or solid. Solid core typically consists of metals, metal oxides, silica, rubbers or polymers, which require different fabrication methods and enable applications [13, 21-23]. Microcapsules with liquid core and solid shell [17-21] have been mainly investigated for the development of delivery systems, cell biology and sensors, and generated by employing different physical and chemical methods.

Materials exploited for the shell can be even organic, as carbon-based compounds, or inorganic, like metals, metal salts or metal oxides. The shell plays a significant role, for example in increasing dispersibility or biocompatibility, as well as in inducing surface modification of the core, or affecting particles functionalities and physicochemical properties (as for example to improve thermal stability, electrical, optical or magnetic response). Over the last few years, metal shells have attracted great attention due to the barrier properties [14]. Depending on the size and composition of the nanoshell, particles can be designed to either absorb or scatter light over wide visible and infrared spectral range. [13, 21-23] Gold is one of the most used metals for this scope [24-26]. This inert metal enhances the physicochemical properties of the core and protects it from degradations, also it is biocompatible and exhibits good electronic and optical properties, becoming a good candidate for applications in several fields involving life science and photonics.

REFERENCES

1. Veerapandian, S., Jang, W., Seol, J.B., Wang, H., Kong, M., Thiyagarajan, K., Kwak, J., Park, G., Lee, G., Suh, W., You, I., Kılıç, M.E., Giri, A., Beccai, L., Soon, A., Jeong, U., 2021. Hydrogen-doped viscoplastic liquid metal microparticles for stretchable printed metal lines. Nat. Mater. 20, 533–540. https://doi.org/10.1038/s41563-020-00863-7
2. Witwer, K.W., Wolfram, J., 2021. Extracellular vesicles versus synthetic nanoparticles for drug delivery. Nat. Rev. Mater. https://doi.org/10.1038/s41578-020-00277-6

3. Manzano, M., Vallet-Regí, M., 2020. Mesoporous Silica Nanoparticles for Drug Delivery. Adv. Funct. Mater. 30, 1902634. https://doi.org/10.1002/adfm.201902634
4. Chung, Y.H., Cai, H., Steinmetz, N.F., 2020. Viral nanoparticles for drug delivery, imaging, immunotherapy, and theranostic applications. Adv. Drug Deliv. Rev. 156, 214 https://doi.org/10.1016/j.addr.2020.06.024
5. Zhang, L., Sun, L., Zhang, Z., Wang, Y., Yang, Z., Liu, C., Li, Z., Zhao, Y., 2020. Bioinspired superhydrophobic surface by hierarchically colloidal assembling of microparticles and colloidal nanoparticles. Chem. Eng. J. 394, 125008. https://doi.org/10.1016/j.cej.2020.125008
6. Carregal-Romero, S., Caballero-D'Iaz, E., Beqa, L., Abdelmonem, A.M., Ochs, M., Ḧuhn, D., Suau, B.S., Valcarcel, M., Parak, W.J., 2013. Multiplexed sensing and imaging with colloidal nano- and microparticles. Annu. Rev. Anal. Chem. 6, 53–81. https://doi.org/10.1146/annurev-anchem-062012-092621
7. Han, X., Xu, K., Taratula, O., Farsad, K., 2019. Applications of nanoparticles in biomedical imaging. Nanoscale 11, 799-819. https://doi.org/10.1039/c8nr07769j
8. Moßhammer, M., Kasper, Brodersen, E., Kühl, M., Koren, K., 2016. Nanoparticle- and microparticle-based luminescence imaging of chemical species and temperature in aquatic systems: a review. Microchimica Acta 186, 126. https://doi.org/10.1007/s00604-018-3202-y

9. Gao, H., Xu, Y., Yao, K., Liu, Y., 2021. Self-Assembly of Silica-Gold Core-Shell Microparticles by Electric Fields Toward Dynamically Tunable Metamaterials. ACS Appl. Mater. Interfaces 13, 14417–14422. https://doi.org/10.1021/acsami.1c02724
10. Zhang, D., De, J., Lei, Y., Fu, H., 2021. Organic multicomponent microparticle libraries. Nat. Commun. 12, 1–10. https://doi.org/10.1038/s41467-021-22060-z
11. Cheng, K., Guo, Jiuchuan, Fu, Y., Guo, Jinhong, 2021. Active microparticle manipulation: Recent advances. Sensors Actuators, A Phys. 322, 112616. https://doi.org/10.1016/j.sna.2021.112616
12. Chu, G., Chen, F., Zhao, B., Zhang, X., Zussman, E., Rojas, O.J., 2021. Self-Assembled Nanorods and Microspheres for Functional Photonics: Retroreflector Meets Microlens Array. Adv. Opt. Mater. 9, 2002258. https://doi.org/10.1002/adom.202002258
13. Ramli, R.A., Laftah, W.A., Hashim, S., 2013. Core-shell polymers: A review. RSC Adv. https://doi.org/10.1039/c3ra41296b
14. Galogahi, F.M., Zhu, Y., An, H., Nguyen, N.T., 2020. Core-shell microparticles: Generation approaches and applications. J. Sci. Adv. Mater. Devices. https://doi.org/10.1016/j.jsamd.2020.09.001
15. Yazdian Kashani, S., Afzalian, A., Shirinichi, F., Keshavarz Moraveji, M., 2020. Microfluidics for core-shell drug carrier particles - a review. RSC Adv. https://doi.org/10.1039/d0ra08607j
16. Li, W., Zhang, L., Ge, X., Xu, B., Zhang, W., Qu, L., Choi, C.H., Xu, J., Zhang, A., Lee, H., Weitz, D.A., 2018. Microfluidic fabrication of

microparticles for biomedical applications. Chem. Soc. Rev. https://doi.org/10.1039/c7cs00263g

17. Yow, H.N., Routh, A.F., 2006. Formation of liquid core-polymer shell microcapsules. Soft Matter. https://doi.org/10.1039/b606965g
18. Liu, Y., Zhang, W., Wang, H., 2021. Synthesis and application of core-shell liquid metal particles: A perspective of surface engineering. Mater. Horizons. https://doi.org/10.1039/d0mh01117g
19. Mytnyk, S., Ziemecka, I., Olive, A.G.L., Van der Meer, J.W.M., Totlani, K.A., Oldenhof, S., Kreutzer, M.T., Van Steijn, V., Van Esch, J.H., 2017. Microcapsules with a permeable hydrogel shell and an aqueous core continuously produced in a 3D microdevice by all-aqueous microfluidics. RSC Adv. 7, 11331–11337. https://doi.org/10.1039/c7ra00452d
20. Kim, S.H., Kim, J.W., Cho, J.C., Weitz, D.A., 2011. Double-emulsion drops with ultra-thin shells for capsule templates. Lab Chip 11, 3162–3166. https://doi.org/10.1039/c1lc20434c
21. Shahabadi, V., Madadi, E., Abdollahpour, D., 2021. Optimized anti-reflection core-shell microspheres for enhanced optical trapping by structured light beams. Sci. Rep. 11, 4996. https://doi.org/10.1038/s41598-021-84665-0
22. Zhang, Y.J., Radjenovic, P.M., Zhou, X.S., Zhang, H., Yao, J.L., Li, J.F., 2021. Plasmonic Core–Shell Nanomaterials and their Applications in Spectroscopies. Adv. Mater. https://doi.org/10.1002/adma.202005900

23. Sun, S., Rasskazov, I.L., Carney, P.S., Zhang, T., Moroz, A., 2020. Critical Role of Shell in Enhanced Fluorescence of Metal-Dielectric Core-Shell Nanoparticles. J. Phys. Chem. C 124, 13365–13373. https://doi.org/10.1021/acs.jpcc.0c03415
24. Tianhao Ji, B., Lirtsman, Vladislav G, Avny, Yair, Davidov, Dan, Davidov, D, Ji, T., Lirtsman, V G, Avny, Y, 2001. Preparation, Characterization, and Application of Au-Shell/Polystyrene Beads and Au-Shell/ Magnetic Beads**, Adv. Mater. https://doi.org/10.1002/1521-4095
25. Graf, C., Van Blaaderen, A., 2002. Metallodielectric colloidal core-shell particles for photonic applications. Langmuir 18, 524–534. https://doi.org/10.1021/la011093g
26. Oćwieja, M., Lupa, D., Adamczyk, Z., 2018. Gold Nanoparticle Layers on Polystyrene Microspheres of Controlled Structure and Electrokinetic Properties. Langmuir 34, 8489–8498. https://doi.org/10.1021/acs.langmuir.8b01491

Chapter 1: Core-shell self-assembled solid microspheres

INTRODUCTION TO LIQUID CRYSTAL MICROPARTICLES

Liquid crystal is a material that exhibit unique functional properties due to its well-defined ordered structure [1]. Moreover, it has soft nature with long-range molecular interactions enabling supramolecular architectures. Based on these features it has been investigated as suitable environment to hierarchical assemble microparticles (MPs), both isotropic and anisotropic [2, 3]. Recent hot trends of chirality-related sciences have addressed investigations based on supramolecular chemistry as well as on 3D printing methods, in order to achieve properly designed chiral components and materials [4]. A small amount of chiral dopant in a mesogenic material (e.g. a nematic liquid crystal), enables to self-organize chiral helicoidal arrangement of the molecules with a significant structural circular dichroism in the visible range [1]. Such features have been widely exploited in the past decades to develop organic microlasers with tunable emission wavelength, circular polarizers, chiral mirrors [5-9]. In form of microdroplets and polymerized microparticles they have demonstrated unique performances in experiments of chiral optomechanics, micro-optics and photonics [10-12].

1.1 MATERIALS AND METHODS

This thesis focuses on the photonics and optomechanical properties of core-shell MPs, based on a dielectric core and a metal (gold nanoparticles, AuNPs) shell. They are composed of a polymeric mesogenic core with bipolar or spherulitic configuration obtained by the UV induced cross-linking of either a pure or chiral nematic reactive

mesogen [13], and an AuNPs shell in which the nanoparticles are assembled in a raspberry-like structure on the core surface. This approach relies on the combination of two processes occurring during UV exposure of the reactive mesogenic aqueous emulsion: 1) photopolymerization of the mesogenic droplets (which constitute the solid core of the particles); 2) photoreduction of chloroauric ions and precipitation of AuNPs that aggregate on the surface of the dielectric core.

By exploiting the thermodynamic properties of a photoreactive liquid crystal, the core-shell MPs are prepared via light induced polymerization of reactive mesogenic droplets, obtained by emulsification process in aqueous solution with a small amount of chloroauric acid ($HAuCl_4$). The subsequent UV light exposure contextually induces the polymerization of the dielectric core and the precipitation of AuNPs. The process is schematically depicted in Figure 1.1.

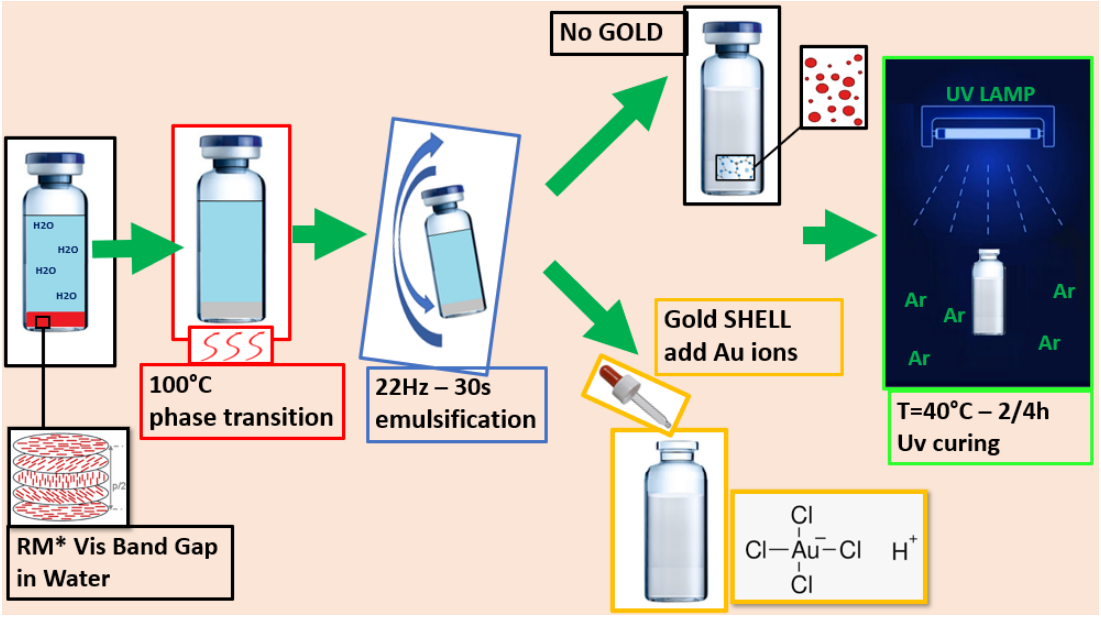

Figure 1.1 Production steps representation of polymerized liquid crystal core-shell microparticles.

The production process common to all kind of MPs is as follows: MPs emulsions are prepared by adding 0.4 wt% of the reactive mesogen to pure water. The glass vial containing the mixture is then heated at 100°C and shaken at 22 Hz for 30 s, in a

laboratory vortex mixer. In order to obtain the AuNPs shell on the MPs, the emulsion is mixed with an equivalent volume of water containing $HAuCl_4$ at specific concentrations in the range 0.1- 0.5 mM. Afterwards, the emulsions are polymerized using an UV lamp (Mega Electronics mod. LV202-E) with light intensity 2 $mWcm^{-2}$ and emission band centered at ≈350 nm. To obtain a homogeneous reaction, the UV curing is performed placing a large section vial between the two fluorescent tubes of the UV lamp. The processes occur under dry nitrogen flux at 40°C, for exposure times ranging from 2 to 5 hours.

After polymerization most of the particles lays down at the vial bottom. To remove polymerization residuals, the supernatant is taken away and replaced by new water and sonicated, helping to prevent MPs clustering. The suspension of core-shell MPs acquires a grey tint, as expected due to the AuNPs aggregation on the MPs surface, which becomes darker for higher HAuCl4 concentration in water.

1.1.1 Birefringent microparticles (NMPs)

The reactive mesogen used for these particles is extracted from RMS03-001C Licrivue^{TM} (Merck, Germany). This mesogen is a mixture of high viscosity nematic liquid crystals, whose molecules are functionalized with acrylate groups that crosslink when exposed to UV radiation. The reactive mesogen is obtained removing the propylene glycol monomethyl ether acetate (PGMEA) solvent, from RMS03-001C by vacuum evaporation at 90°C overnight. Due to the mesogen hydrophobicity, nematic droplets with size in the range 1-20 μm can be obtained by emulsification process in water. Indeed, the parallel anchoring of the molecules at the water interface promotes an internal bipolar configuration [14] compelling the particle to an ellipsoidal shape.

As previously described, the subsequent UV light exposure contextually induces the polymerization of the dielectric core and the precipitation of AuNPs.

1.1.2 Chiral microparticles (CMPs)

The second kind of MPs produced provides a chiral nematic supramolecular arrangement. To this aim the reactive mesogen is mixed with a chiral dopant (ZLI-811 or ZLI-3786) in a weight fraction ranging from 19 to 25%.

The left-handed enantiomer ((S)-2-Octyl 4-[4-(Hexyloxy)benzoyloxy]benzoate, ZLI-811, and the right-handed enantiomer ((R)-2-Octyl 4- [4-(Hexyloxy)benzoyloxy]benzoate, ZLI-3786, were purchased from Merck, Germany.

The parallel anchoring of the molecules at the water interface promotes an internal spherulitic configuration that, depending on the mesogen parameters (i.e., elastic constant, viscosity, etc.), can be preserved even in the low chirality regime, for droplets diameter down to twice the helical pitch [15]. Due to the internal radial orientation of the cholesteric axis, the chiral droplets obtained by emulsification process in water, acquire a spherical shape. Depending on the dopant concentration the pitch of the helicoidal supramolecular arrangement can be tuned in the range 400-250nm, giving rise to a selective Bragg reflection phenomenon for circularly polarized light, with the same handedness of the dopant, in the visible spectrum (650-400 nm) [13]. Analogous to NMPs the UV exposure induces core polymerization and AuNPs precipitation. After polymerization, a small blue shift (about 10nm) of the selective reflection band is observed, compatible with the occurrence of shrinkage effects.

1.2 MICROPARTICLES CHARACTERIZATION

1.2.1 Scanning Electron microscopy (SEM)

SEM analyses are performed using a FEI-Philips ESEM-FEG Quanta 200F apparatus operating in the range 5–20 kV with a working distance of 6–15 mm.

The measurements are carried out on MPs deposited on a flat surface and covered with a thin layer of graphite in order to investigate the core-shell morphology, surface and distribution of the MPs. The investigations clearly prove the presence of AuNPs over the polymeric MPs surfaces and support the hypothesis that, during the UV irradiation, AuNPs nucleate on the surface, favored by its roughness. Images in figure 1.2 show MPs covered by AuNPs that uniformly aggregate on the surface forming a shell.

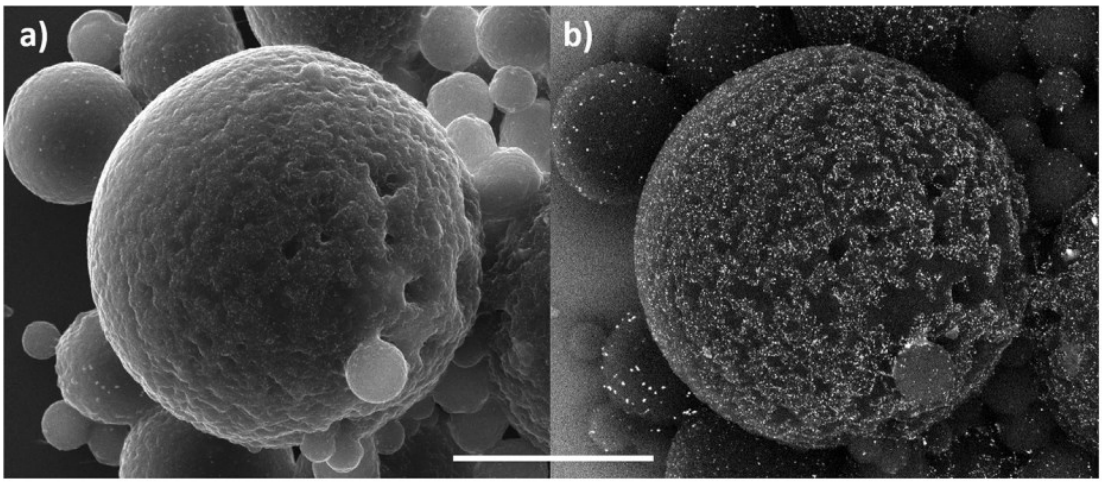

Figure 1.2 SEM image of chiral MPs with shell of AuNPs. a) secondary electron signal; b) back-scattered electron signal. White bar scale is 10 μm.

The MPs size distribution, either without or with AuNPs shell, were determined by SEM imaging (figure 1.3a and 1.3c) and represented through the histograms shown in figure 1.3b and 1.3d.

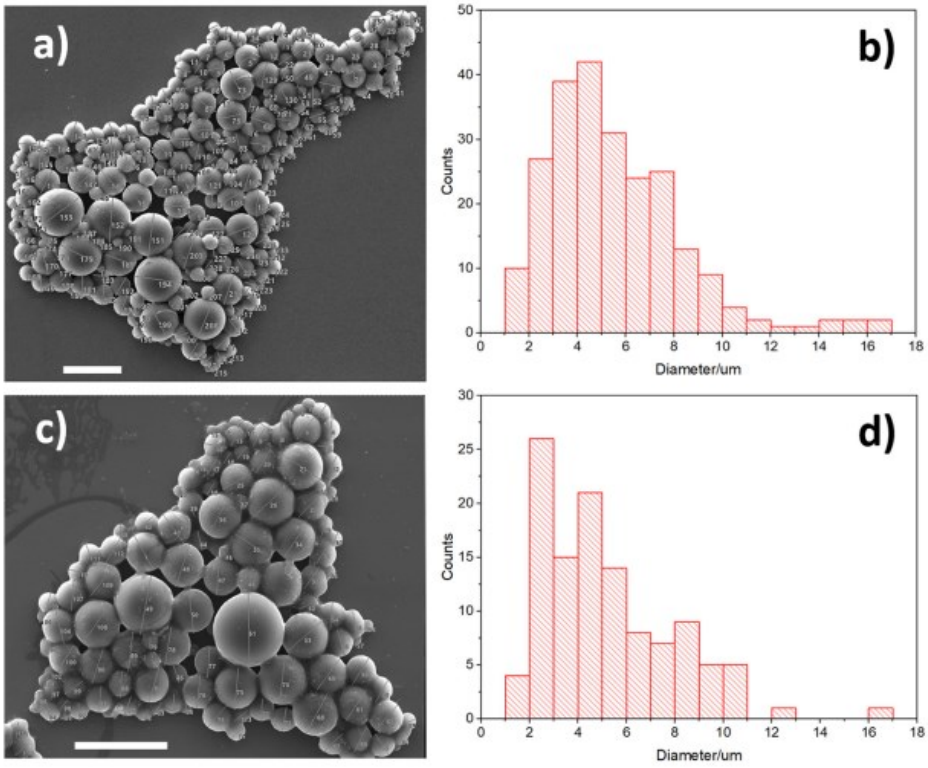

Figure 1.3 a) SEM images and b) diameter distribution a collection of bare MPs. c) SEM images and d) diameter distribution of a collection of MPs with AuNPs shell. White bar scales are 20 μm for a) and c).

A large heterogeneity of the particles size is displayed in both cases, MPs diameters range from 1 μm to 20 μm. The mean diameter values evaluated from the histograms for the bare and the core-shell MPs, 5.6 ± 0.7 μm and 5.2 ± 0.8 μm respectively, are consistent within the uncertainties. Such results support that the MPs size is determined by the emulsification process and not affected by the $HAuCl_4$ in aqueous solution or the NPs precipitation process.

SEM images in figure 1.4, shows MPs obtained at different $HAuCl_4$ concentrations: a) 0.00mM; b) 0.10mM; c) 0.25mM; d) 0.50mM, respectively. As expected, different AuNPs coverages are displayed, growing with the $HAuCl_4$ concentration values. For lower concentrations, the isolated AuNPs are visible on the polymeric core surface,

while for the higher ones aggregates of AuNPs are also found, whose diameter is less than 100 nm.

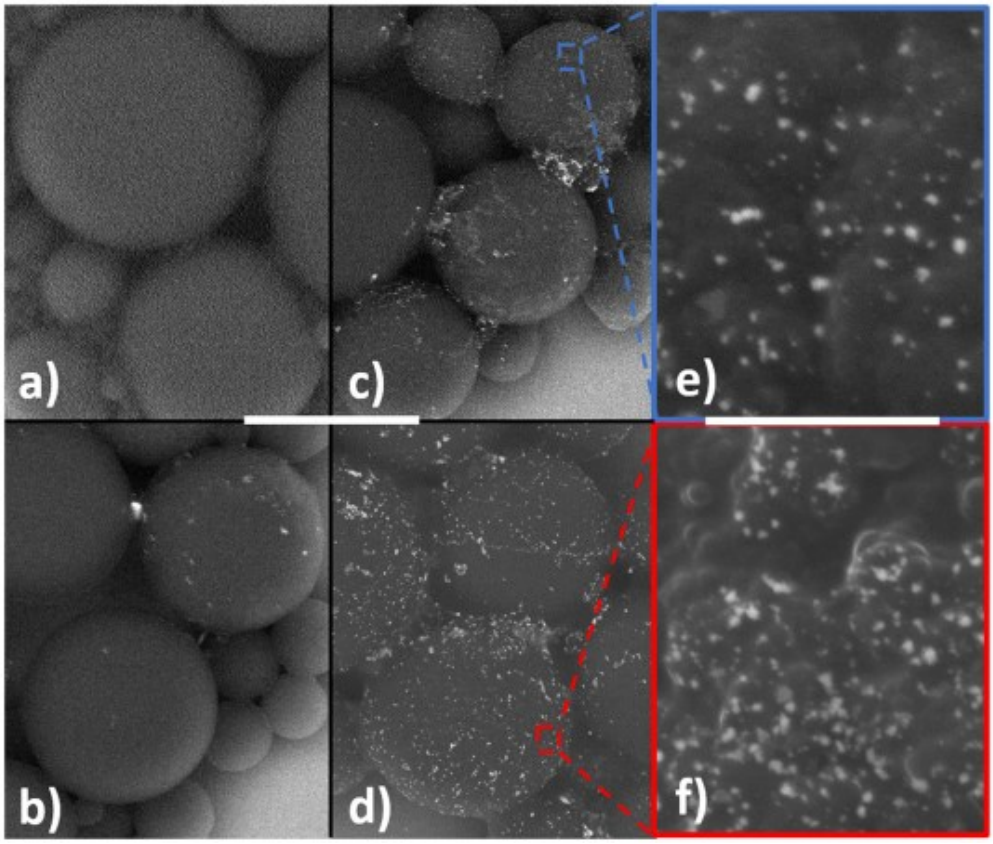

Figure 1.4. Back-scattered electron SEM images taken on the sample without chloroauric acid a) and for samples with increasing concentration of chloroauric acid, b) 0.10mM, c) 0.25mM, d) 0.50mM. e) and f) are magnifications of c) and d) respectively. White bar scales are 10 µm for a)-d) and 1 µm for e) and f).

1.2.2 Transmission Electron microscopy (TEM)

TEM imaging is carried out to investigate the internal structure of MPs and the distribution of the AuNPs on their surface. The solid MPs were first embedded in an epoxy resin (Araldite, Fluka) and successively cut into ultrathin sections of about 100 nm by means of a diamond knife. The ultrathin sections were collected on copper grids then examined with a Zeiss EM10 transmission electron microscope at 80 kV acceleration voltage.

In figures 1.5 a-b) are reported sections images of three different AuNMPs that display anyway an ellipsoidal shape. It is possible to estimate the particles elongation through the ratio between their larger and smaller diameter. For both particles in figure 1.5a the ratio is about 0.75, while for the particle in figure 1.5b is 0.82. An assessment of this ratio for both kinds of spheroidal MPs (with and without AuNPs shell) shows that its value is independent from the AuNPs coverage, as expected, and ranges from 0.75 to 0.95.

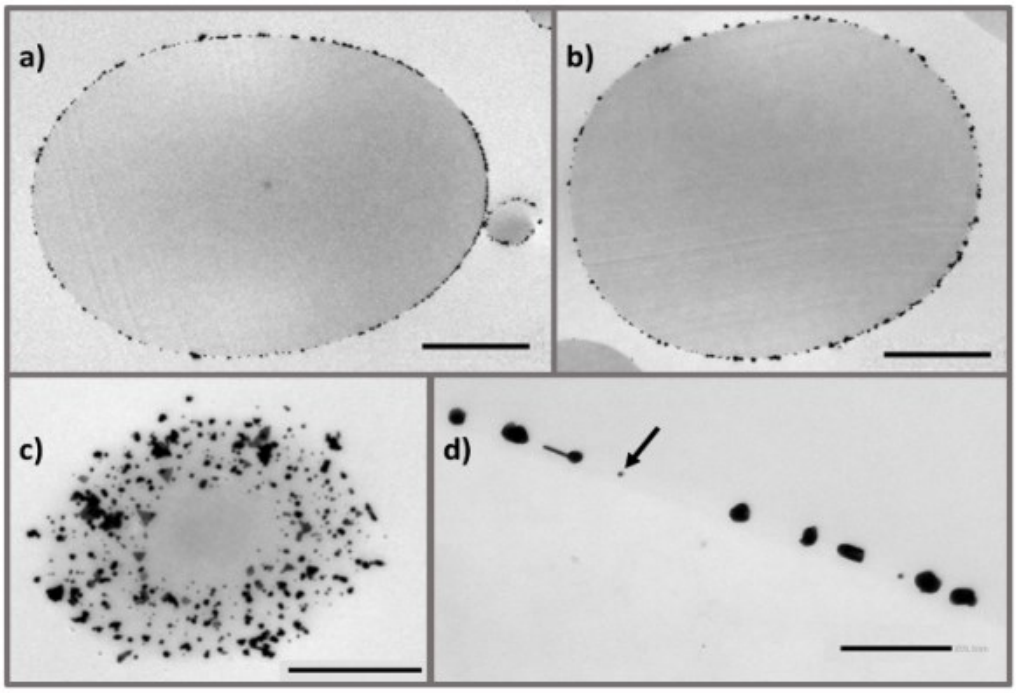

Figure 1.5 a) and b) different AuNMPs TEM thin central section images, bar scales 2μm. c) section of area close to a pole, note the AuNPs distribution on the surface, bar scale 1μm. d) AuNPs shell on the surface of nematic microparticles, bar scale 200nm.

Figures. 1.5 a-b) also clearly show that the AuNPs aggregate almost uniformly in a shell around the dielectric core. The TEM image in figure 1.5c shows the section of a particle sliced near a pole, where a large portion of the MP surface allows visualizing the distribution of the AuNPs. AuNPs clusters of different shape and size can be found with an almost uniform distribution within the shell. Figure 1.5d shows a magnification

of the shell section; here spherical AuNPs of about 10nm (see the arrows in figure) can be clearly seen, as well as clusters with size of 30-50nm.

Regarding the CMPs, TEM images offer also the opportunity to evaluate the internal supramolecular structure. In figure 1.6 are reported the sections images of different AuCMPs, that always display the typical internal particle architecture with highly ordered concentric lamellar structure.

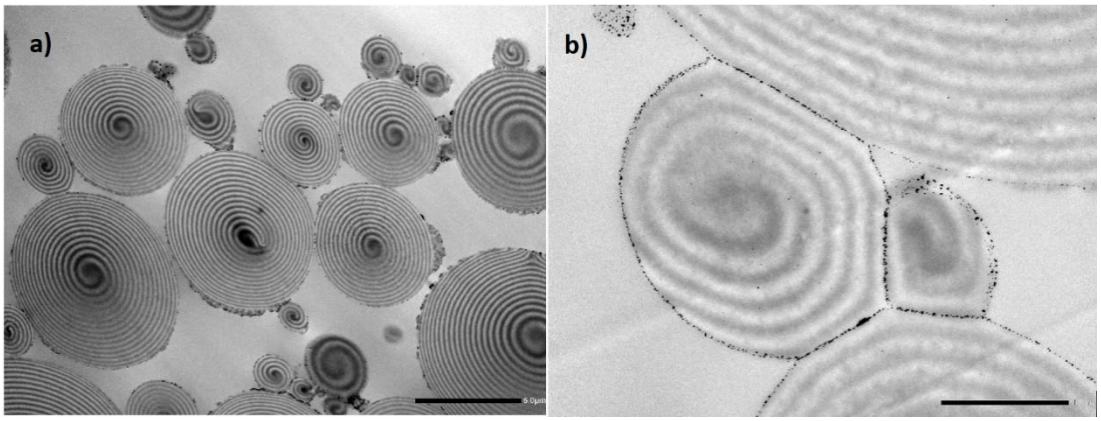

Figure 1.6 a) and b) different AuCMPs TEM thin section images, bar scales are 5μm and 1μm respectively.

As reported in [16], the rings are due to the topography of the sections. These corrugations, which occur at certain orientation of the director **n**, are due to the cutting process. Indeed, the knife bends the polymer chains or cuts them, depending on their orientations, producing surface fractures that reveal the structure of the specimen.

1.2.3 Chemical analysis

Analysis on chemical elements is performed using the JEOL JXA 8230 Electron Probe Microanalyzer, with a tungsten source gun, equipped with five wavelength-dispersive spectrometers (WDS) and one silicon drift detector energy-dispersive spectrometer (SDD, EDS).

Results on elements presence are reported in figure 1.7, where comparative analysis of the spectra of CMPs produced in water without (1.7a) and with $HAuCl_4$ (1.7b) support the AuNPs shell formation. Indeed, the Au characteristic X-ray energy peaks M and Lα at 2.120 and 9.712keV, respectively, are evidently displayed only in the MPs specimen with AuNPs shell.

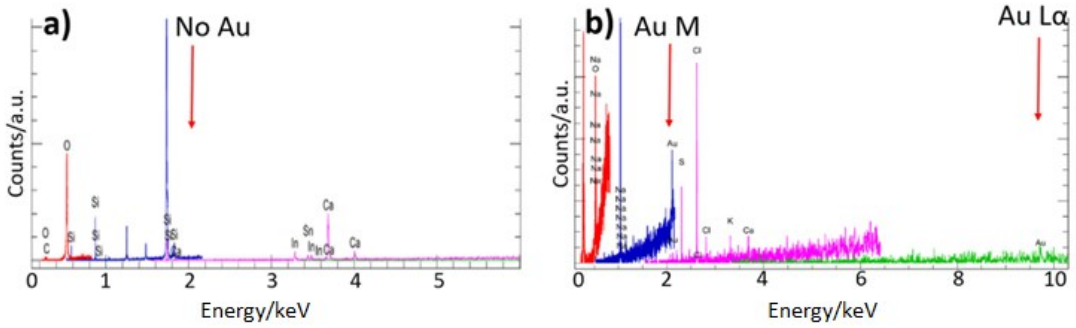

Figure 1.7 EDX spectra element microanalysis of chiral MPs without (a) and with (b) AuNPs shell, where M and Lα X-ray energy values are indicated by red arrows.

1.2.4 Spectroscopy

The UV-VIS-IR optical spectroscopy has been used to investigate both kinds of MPs, with and without AuNPs shell. To perform the measurements two samples have been prepared, collecting the MPs on glass substrates. Reflectance spectra of the two specimens are acquired by a Cary 5E spectrophotometer equipped with an integrating sphere.

For the NMPs, reflectance spectra of the two kinds of MPs, show a noticeable difference in the whole investigated spectral range that can be significantly ascribed to the AuNPs shell (see figure 1.8). Indeed, the spectrum of the bare MPs exhibits a quite constant value over the whole range, while AuNMPs one exhibits a clearly different trend, with a substantial increase in the red-near IR region of the spectrum (above 600nm), as expected, due to the gold shell.

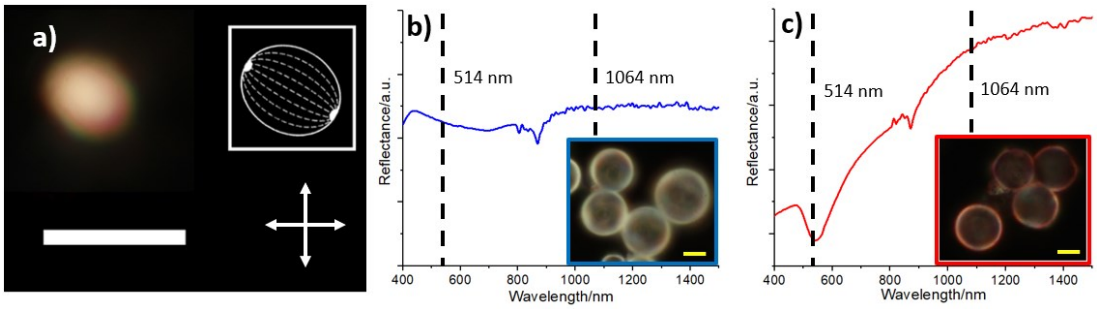

Figure 1.8 Optical microscope transmission images of a NMP with cross polarizers, bar scale 5 μm. In the inset the bipolar configuration scheme is shown. Reflectance spectra of NMPs (blue line in b) and AuNMPs (red line in c). In the inset the optical reflection microscopy images of NMPs (b) and AuNMPs (c), bar scales 2 μm.

Moreover, the evident depletion around 560nm can be definitely associated to the plasmonic resonance.

AuNPs absorbance spectrum is estimated starting from the transmittance and reflectance spectra through the following equation [17]

$$A_{Au}(\lambda) = A_{AuNMPs}(\lambda) - A_{NMPs}(\lambda) = -\log(T_{AuNMPs} + R_{AuNMPs}) + \log(T_{NMPs} + R_{NMPs}) = -\log\frac{T_{AuNMPs}+R_{AuNMPs}}{T_{NMPs}+R_{NMPs}} \quad (1.1)$$

where $A_{AuNMPs}(\lambda)$ and $A_{NMPs}(\lambda)$ are the total absorbance of the core-shell MPs-AuNPs and the bare NMPs, respectively, taking for granted the similar particles densities among the specimens.

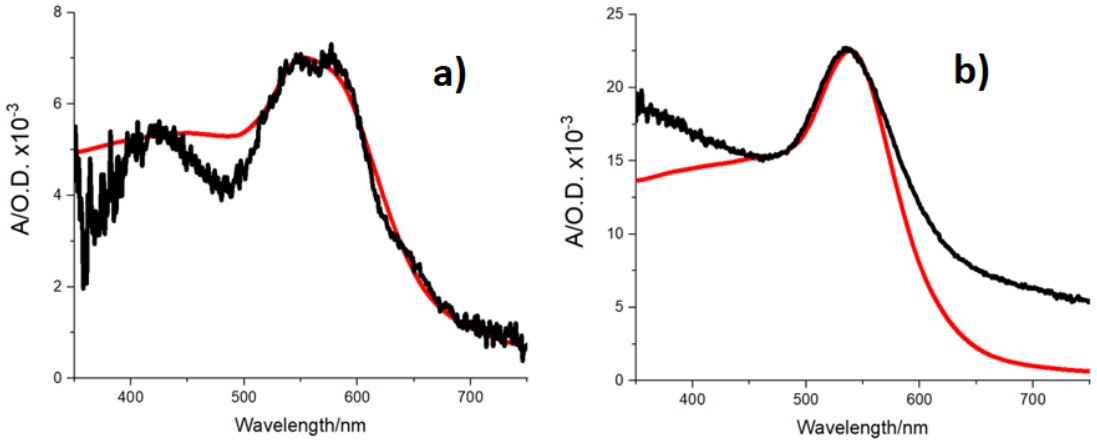

Figure 1.9 a) Absorbance (Optical Density) of AuNPs shell (black line) obtained from the total transmittance and reflectance (eq.1). b) Absorbance (Optical Density) of AuNPs (black line) in water suspension obtained by eq.1. The red line in a) and b) is the absorbance calculated from Mie scattering model.

In Figure 1.9a (black line) the absorbance evaluated from equation 1.1 clearly shows a peak at 560 nm which can be attributed to the dipole plasmon resonance of the AuNPs. A usually adopted approach for modeling the optical response of spherical NPs dispersion in a surrounding media is based on the Mie theory. Such approach can be implemented considering that MPs diameter is generally two orders of magnitude larger than the NPs ones. The Mie scattering model for AuNPs [18] provides a fair approximation of the measured absorbance. Here, Mie absorbance

$$A_{Mie} = \frac{\frac{\pi}{4}D^2 Q_{abs} a}{\ln 10}, \qquad (1.2)$$

is evaluated from the absorption efficiency Q_{abs}, by Mie plot v4.6.24 software [19], using a Log-normal dispersion of the NPs diameter and by setting to 1.63 the average refractive index of the reactive mesogen. $\frac{\pi}{4}D^2 Q_{abs}$ represents the absorbance cross section, D is the diameter of the AuNPs corresponding to the peak of the distribution, and a is the surface density of AuNPs. The best approximation, figure 1.9a (red line), is obtained for D=90 nm and a=10^8 #/cm^2. It is worthy to note that the D value coming

from the simulation is compatible with the SEM investigation results where NPs population has a diameter of the same order of magnitude.

The simulation of the absorbance spectrum is in good agreement with the absorbance evaluated from the spectrophotometric investigations (figure 1.9a), and both show a peak at 560 nm located at the typical wavelength of the gold plasmonic resonance in the polymeric environment.

In order to validate the results obtained for the AuNMPs, an analysis of just AuNPs was also performed, as reported in figure 1.9b where absorbance of AuNPs water suspension is shown. Preparation of AuNPs suspension has been done in the same experimental conditions of the MPs emulsion but stopping the UV irradiation after one hour, before the MPs polymerization is completed. The AuNPs are subsequently separated from the unpolymerized MPs by centrifugation. Transmission and reflection spectra are made in a 1mm thick quartz cuvette. Figure 1.9b displays a peak at 535nm as expected for the plasmonic resonance of AuNPs in aqueous environment (black line). The best approximation, figure 1.9b (red line), is obtained for D=90 nm and a = $2.6 \cdot 10^8$ #/cm^2, in excellent agreement with the measurements made on the AuNMPs.

As far as CMPs are concerned, the optical properties of these particles depend on the concentration of chiral dopant within the nematic mixture. As shown in figure 1.10, for this type of materials it is possible to select the photonic band gap in a very fine way.

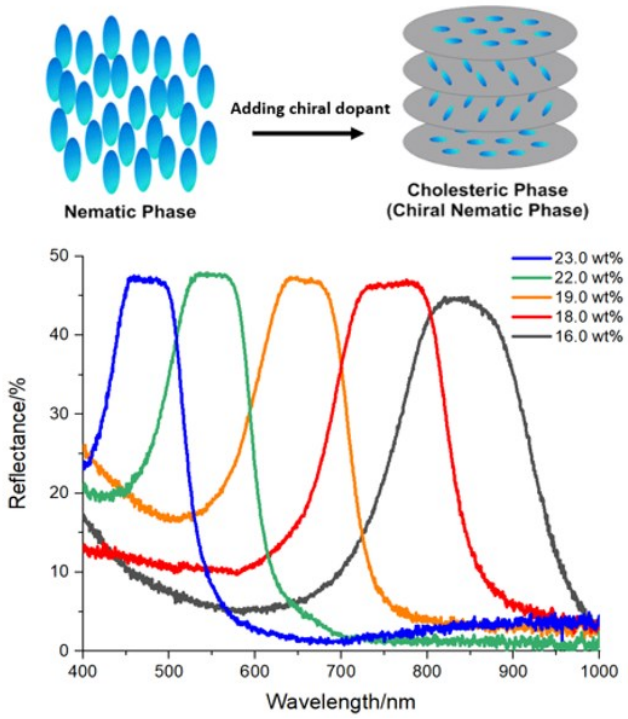

Figure 1.10 Reflectance of reactive mesogenic films at different concentration of chiral dopant.

In figure 1.11 are reported images CMPs with and without AuNPs shell where concentration of chiral dopant ZLI-811 is 24.5 wt%. The typical Maltese cross observed in transmission mode between crossed polarizers for the two kinds of particles demonstrates that addition of $HAuCl_4$ in the water emulsion before the photoinduced polymerization does not modify the mesogenic molecules orientation at the water interface. As a result, it does not affect the spherulitic configuration of the precursor droplets. Indeed, in reflection mode, a blue-violet colored spot coming from the center is observed for the CMPs, displaying an omnidirectional Bragg reflection, confirmed by the CMPs reflection spectrum (figure 1.11b). The reflection spectrum of CMPs covered by AuNPs shell shows that the Bragg reflection band related to the pitch of the core structure is not modified. Nevertheless, the spectrum shows differences in the green and red regions that can be both accounted for the AuNPs contribution.

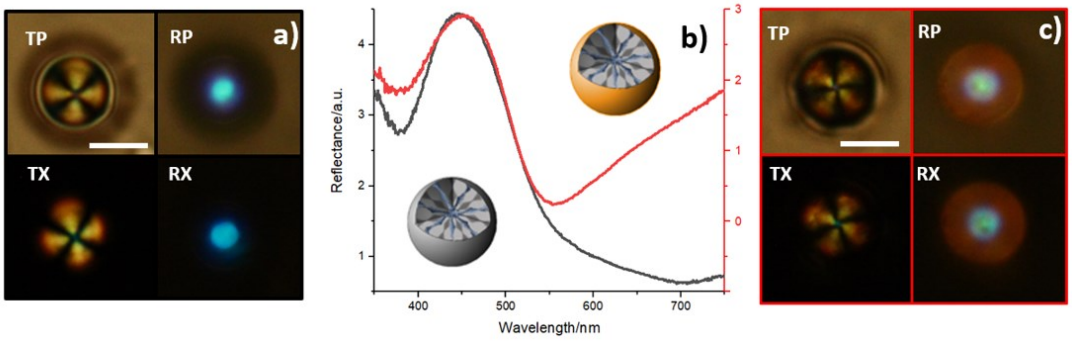

Figure 1.11 CMPs, without a) and with c) gold shell NPs, observed in transmission and reflection modes (T: transmission, R: reflection, P: parallel polarizers, X: cross polarizers). White scale bar is 5 μm. In b) the reflection spectra of a collection of CMPs on a glass substrate with (red line) andμ without (black line) AuNPs shell are reported. In the insets the schematic representations of the internal structure.

REFERENCES

1. L. M. Blinov, *Structure and properties of liquid crystals*. Springer Science & Business Media, 2010.
2. Rodarte, A.L., Cao, B.H., Panesar, H., Pandolfi, R.J., Quint, M., Edwards, L., Ghosh, S., Hein, J.E., Hirst, L.S., 2015. Self-assembled nanoparticle micro-shells templated by liquid crystal sorting. Soft Matter 11, 1701–1707. https://doi.org/10.1039/C4SM02326A
3. Kim, D.S., Lee, W., Lopez-Leon, T., Yoon, D.K., 2019. Self-Regulated Smectic Emulsion with Switchable Lasing Application. Small 15, 1903818. https://doi.org/10.1002/SMLL.201903818
4. Ariga, K., Mori, T., Kitao, T., Uemura, T., 2020. Supramolecular Chiral Nanoarchitectonics. Adv. Mater. https://doi.org/10.1002/adma.201905657
5. Kopp, V.I., Fan, B., Vithana, H.K.M., Genack, A.Z., 1998. Low-threshold lasing at the edge of a photonic stop band in cholesteric

liquid crystals. Opt. Lett. 23, 1707. https://doi.org/10.1364/ol.23.001707

6. Chanishvili, A., Chilaya, G., Petriashvili, G., Barberi, R., Bartolino, R., Cipparrone, G., Mazzulla, A., Oriol, L., 2003. Phototunable lasing in dye-doped cholesteric liquid crystals. Appl. Phys. Lett. 83, 5353–5355. https://doi.org/10.1063/1.1636818
7. Inoue, Y., Moritake, H., 2020. Lasing stability of quasi-CW driven cholesteric liquid crystal lasers. Jpn. J. Appl. Phys. 59, 052006. https://doi.org/10.35848/1347-4065/ab864f
8. Petriashvili, G., Chanishvili, A., Wardosanidze, Z., 2021. Cholesteric liquid crystal mirror-based imaging Stokes polarimeter. Appl. Opt. 60, 3187. https://doi.org/10.1364/ao.422814
9. Ryabchun, A., Bobrovsky, A., 2018. Cholesteric Liquid Crystal Materials for Tunable Diffractive Optics. Adv. Opt. Mater. 6, 1800335. https://doi.org/10.1002/adom.201800335
10. Tkachenko, G., Brasselet, E., 2014. Helicity-dependent three-dimensional optical trapping of chiral microparticles. Nat. Commun. 5, 1–8. https://doi.org/10.1038/ncomms5491
11. Humar, M., Muševič, I., 2010. 3D microlasers from self-assembled cholesteric liquid-crystal microdroplets. Opt. Express 18, 26995. https://doi.org/10.1364/oe.18.026995
12. Hernández, R.J., Mazzulla, A., Provenzano, C., Pagliusi, P., Cipparrone, G., 2015. Chiral resolution of spin angular momentum in linearly polarized and unpolarized light. Sci. Rep. 5, 1–11. https://doi.org/10.1038/srep16926

13. Cipparrone, G., Mazzulla, A., Pane, A., Hernandez, R.J., Bartolino, R., 2011. Chiral self-assembled solid microspheres: A novel multifunctional microphotonic device. Adv. Mater. 23, 5773–5778. https://doi.org/10.1002/adma.201102828
14. Tjipto, E., Cadwell, K. D., Quinn, J. F., Johnston, A. P., Abbott, N. L., & Caruso, F. (2006). Tailoring the interfaces between nematic liquid crystal emulsions and aqueous phases via layer-by-layer assembly. *Nano letters*, *6*(10), 2243-2248. https://doi.org/10.1021/nl061604p
15. Shi, Y., Zhu, T., Zhang, T., Mazzulla, A., Tsai, D.P., Ding, W., Liu, A.Q., Cipparrone, G., Sáenz, J.J., Qiu, C.W., 2020. Chirality-assisted lateral momentum transfer for bidirectional enantioselective separation. Light Sci. Appl. 9, 2047–7538. https://doi.org/10.1038/s41377-020-0293-0
16. Provenzano, C.; Mazzulla, A.; Pagliusi, P.; De Santo, M. P.; Desiderio, G.; Perrotta, I.; Cipparrone, G. Self-Organized Internal Architectures of Chiral Micro-Particles. APL Mater. 2014, 2 (2), 022103. https://doi.org/10.1063/1.4863837.
17. Swinehart, D.F., 1962. The Beer-Lambert law. J. Chem. Educ. 39, 333. https://doi.org/10.1021/ed039p333
18. Doak, J., Gupta, R.K., Manivannan, K., Ghosh, K., Kahol, P.K., 2010. Effect of particle size distributions on absorbance spectra of gold nanoparticles. Phys. E Low-dimensional Syst. Nanostructures 42, 1605–1609. https://doi.org/10.1016/J.PHYSE.2010.01.004

19. Laven, P., 2011. MiePlot (A computer program for scattering of light from a sphere using Mie theory & the Debye series). http://www.philiplaven.com/mieplot.htm.

Chapter 2: Optomechanics

INTRODUCTION

The optical manipulation of small particles provides both an important tool and a very flexible method for investigation of processes at the micro- and nano-scale [1-5], as well for technological development of driving micromachines [6-11]. These features enable applications in several fields ranging from cell surgery, microinjection, micro-rheology, etc.. Through the use of different spatial configurations of the incident light beam, different trapping profiles can be created [12], this leads to different motions of the trapped objects which can be rotational or orbiting depending on the structure of the light [13-17]. Nevertheless, the use of Gaussian beams in simplified geometries can provide some opportunities enabling easier and wider applications. In this view, the fabrication of complex micro and nano objects which undergo multiple motions when illuminated with light can offer several opportunities for mechanics at small scale.

Rotation at the microscale is one of the tasks that has been widely investigated [18]. Microrheology has taken several advantages from these studies with applications in several fields ranging from hydrodynamics to biology. Birefringent particles were firstly investigated since their spinning can be easily controlled by the optical torque induced by polarized light [19,20]. However, the magnitude of the torques that can be induced by light to birefringent particles is small.

Recent investigations have demonstrated that spherical particles with eccentric core–shell geometry can be used to generate considerable optical torques able to induce noticeable rotation rates in spherical particles of nanometric size opening opportunities for nano-rheology and biophotonics [21].

Indeed core-shell architecture enables to impart unique customized properties to MPs, through the proper selection of composition and aggregation of the inner and outer materials.

They are a class of particles whose design provides the opportunity to acquire features and properties not achievable by the individual materials of the core and the shell [22-28].

2.1 THEORY

When a microparticle is illuminated by a tightly focused laser beam, optical trapping and manipulation can be performed thanks to the optical force, $F_{opt,}$ originating from the exchange of linear momentum between the light beam and the particle [1]. However, in case of structured light beams and/or birefringent or absorbing particles angular momentum can be also transferred, generating a torque that induces a rotational motion of the particle [20]. For particles size larger than the laser wavelength, a geometric/ray optics approximation can be considered to discuss the optical trapping condition and the induced dynamical behavior. In such approach the light beam is decomposed into individual rays that propagate in straight lines inside the media. Each ray reflects and refracts at the particle interface according to Snell's law, with reflection and transmission amplitudes proportional to the Fresnel coefficients. [1] The linear momentum exchange between the incident ray and the reflected or refracted ones induces a force on the particle. The total optical force is obtained by the sum over all the incident rays. Dielectric particles can be trapped in 3D providing that their refractive index is larger than the surrounding fluid one. Moreover, the 3D trapping stability also depends on the experimental geometry and focusing condition of the laser beam. When the beam focus is located inside the

chamber where is the particle suspension, 3D trapping occurs; conversely, if the beam focus is positioned before or after the chamber and the illuminated area of the sample is larger than the particle size, the particle is trapped in a plane perpendicular to the beam axis, the so-called 2D trapping [29].

In case of absorbing or reflecting particles, a large radiation pressure is generally produced, and the particles are pushed out from the irradiated region [30,31] preventing the optical trapping.

Rotational motion is produced by the transfer of angular momentum from the light to the particles, in the form of spin angular momentum (SAM), related to the light polarization (circular), or orbital angular momentum (OAM), associated with the light wavefront shape [13,18].

Particles features also allow this transfer: absorbing particles or particles with anisotropic shape, like the ellipsoidal ones, or with anisotropic optical properties (like birefringence), can experience a torque due to SAM transfer. In these cases, spinning of the particles is typically induced, while light with OAM (i.e., Laguerre-Gauss, Bessel beams, etc.) generates orbital motion [18 and references therein]. In all cases, the spin and orbital velocities of the particle result from the balance between the optical and the viscous torques and forces [18,19].

2.1.1 Transfer of linear momentum

For the study of the optomechanical properties of particles treated in this chapter, the theory known as the ray optics model will be used. This is possible due to the micrometric dimensions of the objects in question, which are therefore greater than the wavelength of the radiation used. As demonstrated by the studies of A. Ashkin [1],

this type of approach offers an excellent prediction of the forces exerted on dielectric particles placed in an optical trap.

An optical trap can be seen as a photon flow, each carrying linear momentum $p = \frac{h}{\lambda}$, where h is the Plank's constant and λ is the wavelength of the incident light.

This momentum can be transferred to the particle through the reflection and refraction processes.

When a non-absorbent dielectric particle is hit by a beam, a small amount of power will be reflected, while the rest will be refracted inside it.

In the case of reflection, considering an elastic collision, there will be a change in the linear momentum of the incident light which, according to Newton's second law, will exert a force on the particle that push it in the direction of the incident light. This force is called the *optical scattering force*.

As for refracted rays inside the particle, we simplify the description by considering the case in which the refractive index of the particle is greater than that of the medium, and the incident laser beam is Gaussian.

Since refraction is a change in the light direction and therefore in speed, also in this case a force will arise acting on the particle which, due to the difference in refractive indices, is directed towards the region of the trap with greater intensity. The latter force is known as the *optical gradient force*.

In order to have a complete description it is useful to consider the multiple reflections that occur inside the particle when the refracted rays try to leave the object.

In the ray optics regime, the optical field is described as a collection of N rays, each one associated with a portion, P_i, of the incident power, the total power is $P = S_i P_i$, and carries a linear momentum $\frac{n_m P_i}{c}$, fixed a section, in unit time, where n_m is a

medium refractive index and c is the light speed. The resulting force F_{Opt} on the particle will be expressed by [32]:

$$\overrightarrow{F_{Opt}} = \frac{n_m P_i}{c}\widehat{r_i} - \frac{n_m P_r}{c}\widehat{r_{r,0}} - \sum_{j=1}^{+\infty}\frac{n_m P_{r,j}}{c}\widehat{r_{r,J}} \qquad \text{(eqn. 2.1)}$$

Where $\widehat{r_i}, \widehat{r_r}, \widehat{r_{r,J}}$, are unit vectors representing the direction of the incident ray and the *jth* reflected and transmitted rays, respectively, calculated using Fresnel's reflection and transmission coefficients. Generally, most of the momentum transferred from the ray to the particle is due to only the first two scattering events, especially for small angle of incidence.

From the previous equation we obtain that the scattering and gradient forces balance determines the position of the particle inside the trap.

2.1.2 Transfer of angular momentum

In addition to linear momentum, light can carry angular momentum (SAM).

To determine this quantity, it is useful to describe the light through its circular components:

$$E = (E_L\widehat{e_L} + E_R\widehat{e_R})e^{i(kz-\omega t)} \qquad \text{(eqn. 2.2)}$$

where E_L and E_R are the complex amplitude of the left and right circular component of the electromagnetic field. When $|E_L| = |E_R|$, the beam is linearly polarized, with the plane of polarization given by the phase angle between the complex amplitudes E_L and E_R. If $E_L = 0$ and $E_R \neq 0$, the light is right circularly polarized, and left circularly polarized if $E_R = 0$ *and* $E_L \neq 0$.

Accordingly as described by Nieneminen et al. [20] is possible to write the intensity as follows:

$$I = \frac{c\epsilon_0 E_L^* E_L}{2} + \frac{c\epsilon_0 E_R^* E_R}{2} = I_L + I_R \qquad \text{(eqn.2.3)}$$

and to evaluate the total angular momentum flux, M_z, of the incident beam taking into account that the angular momentum of circularly polarized photons is ±ħ, the photon flux per unit area, N, is

$$N = \frac{I}{\hbar\omega} = \frac{I_L}{\hbar\omega} + \frac{I_R}{\hbar\omega} \quad \text{(eqn. 2.4)}$$

giving an angular momentum flux density of

$$m_z = \frac{I_L - I_R}{\omega} \quad \text{(eqn. 2.5)}$$

The net circularly polarized component is $|I_L\text{-}I_R|$ and is the only contribution to the light angular momentum. We can define a coefficient of circular polarization σ_z:

$$\sigma_z = \frac{I_L - I_R}{I} \quad \text{(eqn. 2.6)}$$

and the angular momentum flux density:

$$m_z = \frac{\sigma_z I}{\omega} \quad \text{(eqn. 2.7)}$$

Integrating the intensity on the beam area we will obtain the total angular momentum flux of the beam as a function of the power:

$$M_z = \frac{\sigma_z P}{\omega} \quad \text{(eqn. 2.8)}$$

If the beam passes through a birefringent material his polarization changes. The incident light will have an initial circular polarization coefficient σ_{zin}, and a different output coefficient σ_{zout}. This change of polarization will have as result a reaction torque on the birefringent material. The reaction torque is equal to the change in the angular momentum flux:

$$\tau_{op} = (\sigma_{zin} - \sigma_{zout})\frac{P}{\omega} \quad \text{(eqn. 2.9)}$$

2.2 ENHANCED ROTATIONAL DYNAMICS OF ANISOTROPIC CORE-SHELL POLYMERIC-METALLIC PARTICLES

The aim of this case study is the analysis of the rotational motion induced by light on core-shell MPs made by a birefringent polymeric core and a nanometric shell of AuNPs. For this purpose, birefringent microparticles (NMPs) with and without a gold

shell are used. Based on the core-shell structure, the optical manipulation with circularly polarized light displays a peculiar rotational motion of these MPs originating from the coupling of the AuNPs optical response and the core anisotropies [33]. A simple Gaussian beam induces a synchronous spinning and orbital motion. Interesting features are also observed when the laser wavelength lies in the plasmonic resonance region. The optical torque originating from the plasmonic absorption, involving the nanometric shell, strongly affects the rotational frequency of the MPs whose spin kinetic energy reaches values two order of magnitude larger than the bare MPs one. Meanwhile, the heating side effect due to the absorption is prevented, enabling enhanced rotation of particles with size of tens of micrometer.

Based on the NMPs anisotropic shape and optical properties, both bare and core-shell NMPs are expected to rotate. The goal is to compare the rotational motions produced in the same experimental condition for both kinds of NMPs, addressing the role of their different optical properties, as reported in figure 1.7 (in the previous chapter).

The bipolar superstructure with which the nematic molecules are arranged and polymerized is supported by the pronounced optical anisotropy (i.e. birefringence in figure 1.7a) of the NMPs. The optical characteristics of the two types of particles are shown in figure 1.7b) and c). From the reflection curves, we see that for the bare NMPs (in blue) there is a uniform scattering for the region between 400nm and 1400 nm.

For AuNMPs, the typical trend of gold reflection is observed, low in the blue spectral region (<500nm) and rising up to the maximum in the IR region. Furthermore, there is a pronounced depletion at 550 nm which indicates the plasmonic absorption peak of the AuNPs in the shell.

2.2.1 Optical tweezer setup

Standard optical tweezers set-up, based on Gaussian laser beam, is employed, as shown in 2.1. In order to investigate the optomechanical behavior of the AuNMPs in the spectral regions where they display the main differences with respect to the bare NMPs, two continuous wave laser sources are used. An Argon-ion laser (Innova 90c, Coherent) at $\lambda = 514$ nm has been chosen to probe how the plasmonic absorption of the AuNPs (figure 2.7) affects the optical trapping and the rotational dynamics. A solid-state source (Ventus HP, Laser Quantum) with lasing wavelength at 1064 nm is used to explore the optomechanics in the spectral region where the AuNMPs exhibit a larger reflectivity (figure 1.7). A 60x microscope objective (numerical aperture NA = 0.85) focuses the Gaussian beam on the 200μm thick sample chamber, containing the NMPs dispersed in water. The beam radius at the sample plane is estimated to be about 7 μm for the Argon laser (514 nm) and about 10 μm for the Nd:YAG (1064 nm). A quarter-wave plate ($\lambda/4$), placed before the objective imposes the circular polarization state of the beam. A beam expander before a dichroic mirror controls the laser focus position with respect to the sample chamber.

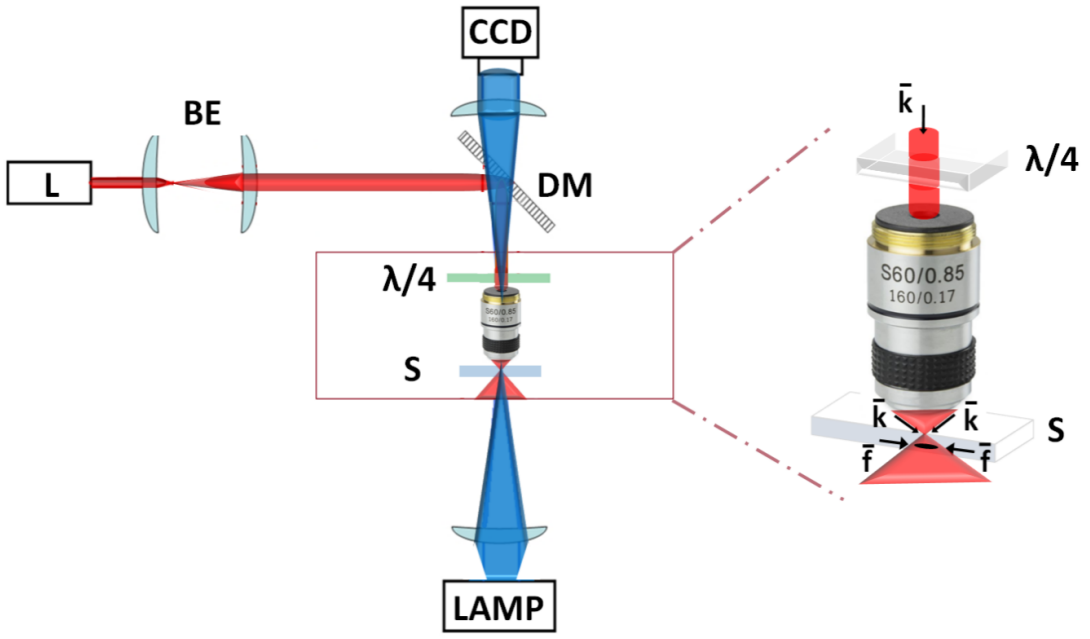

Figure 2.1. Optical tweezers scheme. L laser source, BE beam expander, CCD camera, DM dichroic mirror, λ/4 quarter-wave plate, 60X objective, S sample, LAMP illumination. In the inset detail of the propagation directions of the wave vectors **k** and the gradient optical force **f**. The scheme is not to scale.

The sample position is adjusted by a three-axis translation stage. A fiber illuminator and a charge-coupled detector (CCD) camera are used to illuminate and image the sample.

The longitudinal position of the laser beam focus with respect to the sample chamber is adjusted to provide a 2D trapping of the NMPs close to the bottom chamber surface. The optical force has a component perpendicular to the beam axis, mainly induced by the gradient of the intensity beam profile (force **f** in figure 2.1), and a weaker axial component (scattering force). The latter is generally responsible of the repulsive force on metallic particles, which could prevent their trapping [31, 34]. Nevertheless, given the distance between the focal point and the lower chamber substrate, the scattering force does not push the AuNMPs away from the illuminated region, although it is expected to be more effective with respect to the bare NMPs.

In addition, it should be mentioned that AuNMPs may experience a lower friction with the close glass surface with respect to the bare NMPs, possibly due to electrostatic forces. Indeed, after several days the NMPs stick to the glass surface, unlike the AuNMPs.

2.2.2 Rotational motion of birefringent microparticles (NMPs)

Birefringent dielectric MPs can be easily trapped due to a gradient force, moreover, also SAM transfer from light to particles is allowed that produces a reaction torque [18,35]. Then, when they are trapped by circularly polarized light to the region of highest intensity (i.e., the Gaussian beam axis), they undergo a continuous spinning. The exerted optical torque [20] induced by the change of the beam's photon polarization state σ, travelling within the birefringent particle, is expressed by (eqn. 2.9). The trapped particle reaches a steady state when the optical torque τ_{op} and the rotational viscous torque τ_{vis} balance each other. In the simplified spherical geometry $\tau_{vis} = K\Omega = 8\pi R^3 \eta \Omega$, where η is the kinematic viscosity of the surrounding medium, R is the average radius of the particle and $\Omega = 2\pi\nu$ its angular velocity.

For a non-spherical particle, as in the present case, also a shape-induced birefringence contribution has to be considered; the torque arises due to the asymmetric scattering forces when the principal axis of the particle is not parallel to the light's electric field [36].

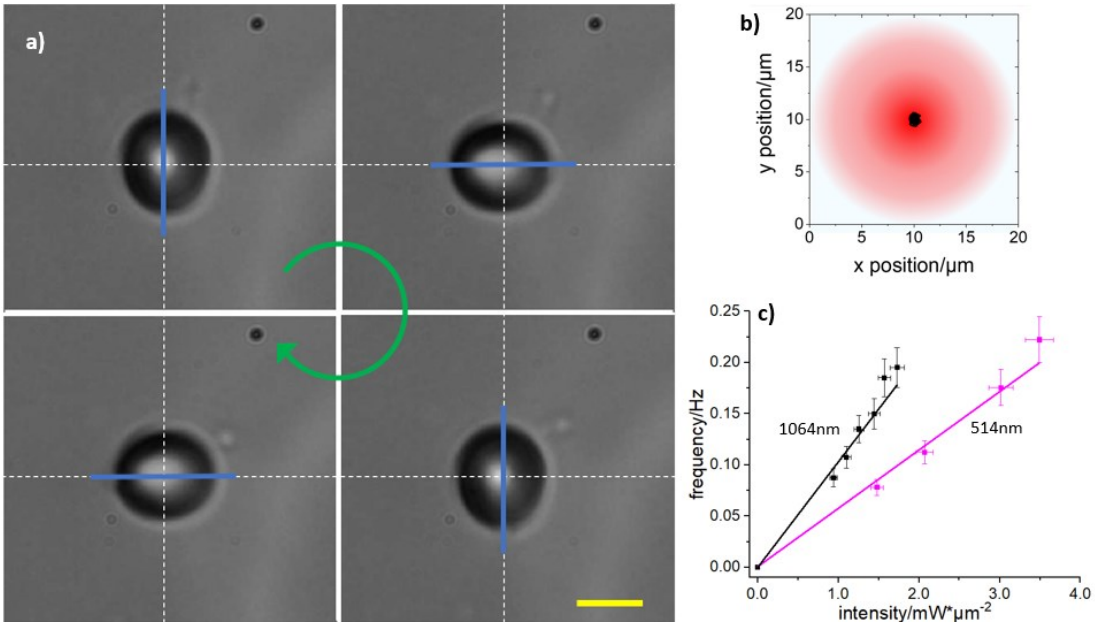

Figure 2.2. a) Sequence of snapshots for a spinning bare NMP when irradiated by a left circularly polarized beam. The blue line represents the long axis of the ellipsoidal NMP. The yellow scale bar is 3µm. b) Track of the central position of a bare NMP which undergoes five full spinning rotations. c) Spin frequency dependence of a bare NMP (average radius 2.8µm) vs beam intensity, at 514nm (magenta) and 1064 nm (black).

Bare NMPs are weakly trapped on axis with the laser beam, for both visible and near IR wavelengths. Spinning occurs clockwise or counterclockwise, according to the handedness of the circularly polarized light.

In figure 2.2a a frames sequence (from video Video_1.avi at the link https://drive.google.com/drive/folders/1ckO2wfEhVpV5GMVElV41S0VvoMvYzUxb?usp=sharing) showing the spinning of a NMP over a period of 3.3 s, is reported. The investigated NMP has a mean radius of 2.8±0.2 µm and is illuminated with a left circularly polarized laser source, at 1064 nm, with a power density of 1.7 mW/µm^2. The major axis of the particle (denoted in blue in figure 2.2a) lays perpendicular to the beam axis and rotates around it. The graph in figure 2.2b shows the position of the particle center of mass during 20s (about 5 full turns) superimposed to the light spot in the trapping plane, demonstrating that the particle is stably trapped at the beam axis position during the rotational motion.

In figure 2.2c the rotational frequencies of NMPs with similar mean radius (2.8±0.2μm) are reported versus the incident beam intensity, for both the 514nm and 1064nm laser. The linear trends of the frequency ν observed for both wavelengths agree with the literature [20]

$$\nu = \frac{\tau_{op}}{2\pi K} \qquad \text{(eqn. 2.10)}$$

Higher rotational frequency is observed for the longer radiation wavelength in the same range of power density, in according to eqn. 2.9. The slopes of the best fit lines, as reported in figure 2.2c, are 0.104 $\mu m^2(mWs)^{-1}$ and 0.057 $\mu m^2(mWs)^{-1}$ at 1064 nm and 514 nm wavelengths, respectively. These values are in excellent agreement with the expectation of eqs. 2.9 and 2.10, since all experimental parameters are the same (particle size, surrounding fluid, etc..) except for the wavelengths.

2.2.3 Rotational motion of AuNMPs

Under the same Vis and near IR circularly polarized laser irradiation, core-shell AuNMPs undergo different rotational dynamics with respect to the bare NMPs, which can be accounted for by the peculiar optical properties introduced by the metallic nanoparticles shell (figure 1.7c). First, the equilibrium position relocates from the beam axis to an annular region around it, whose radius is almost independent from the beam intensity. Only above a certain intensity value (i.e., about 4.0 and 2.0 $mW/\mu m^2$ at 514 nm and 1064 nm, respectively) the circular orbit becomes unstable and the AuNMPs are pushed out from the illuminated region. Below these values, due to the circular polarization of the light, the particles constrained in the annular region simultaneously spin and orbit around the beam axis. Such behavior has been observed in the intensity ranges 1.5-4.0 and 1.0-2.0$mW/\mu m^2$ for λ = 514 nm and 1064nm,

respectively, while no rotation has been detected for lower intensity values. In figure 2.3a a frames sequence (from video Video_2.avi at the link https://drive.google.com/drive/folders/1ckO2wfEhVpV5GMVElV41S0VvoMvYzUxb?usp=sharing) shows the rotational motion, with a period of about 1.7 s, of an AuNMP with a mean radius 2.8±0.2 μm illuminated by the 1064 nm laser source at 1.7 mW/μm^2 intensity. The white dashed lines cross at the position of the beam axis (i.e., the peak intensity position of the Gaussian beam). A peculiar feature of the AuNMPs rotational motion emerges at each orbital position, the particle optical axis keeps the same angle with the radial direction (i.e., the line connecting the particle center with the beam center) indicative of the synchronous spinning and orbital motion performed by the AuNMP. The graph in figure 2.3b shows the orbits described by the AuNMP center of mass in nine seconds (about 5 full turns) superimposed to the light beam spatial distribution in the trapping plane. The orbits show an almost elliptical shape with a major and minor semiaxis of 5.5±0.5 μm and 4.5±0.5 μm. respectively. In figure 2.3c are reported the rotational frequencies measured as a function of the light beam intensity for both wavelengths.

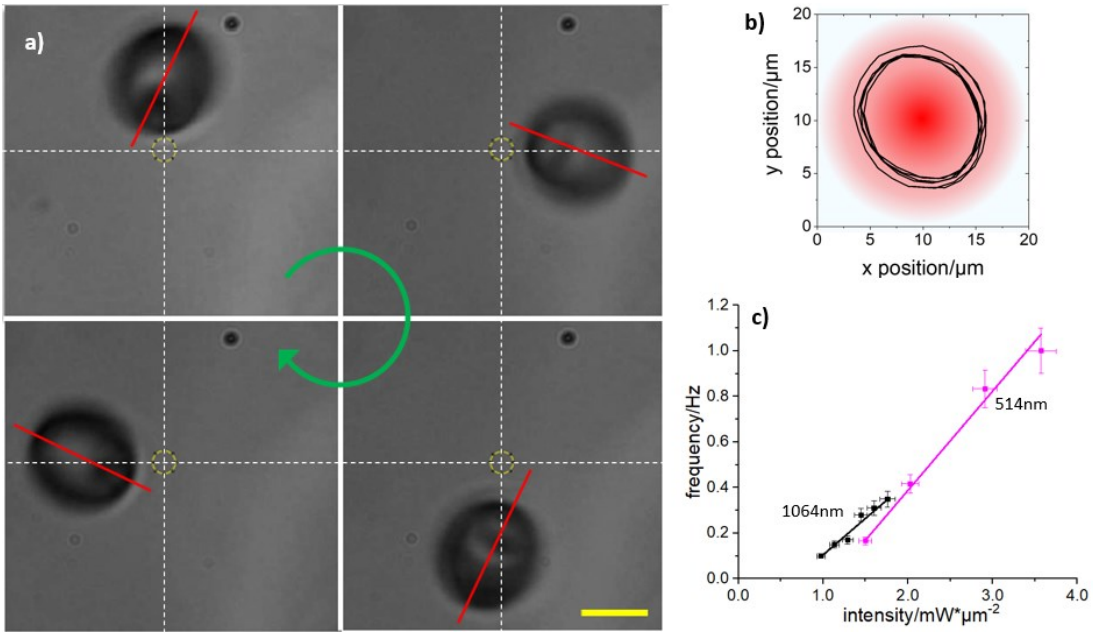

Figure 2.3 a) Sequence of snapshots for a spinning AuNMP when irradiated by a left circularly polarized beam. The red line represents the long axis of the ellipsoidal AuNMP. The yellow scale bar is 3µm. b) Track of the central position of the AuNMP which undergoes five full spinning rotations. c) Spin frequency dependence vs beam intensity of 3.2µm and 2.8µm radius AuNMPs, at 514nm (magenta) and 1064 nm (black), respectively.

Comparing these measurements with the ones of the bare NMPs, makes it clear that the presence of a shell of AuNPs around the polymeric NMP boosts its rotational dynamics at both beam trap wavelengths. The rotational frequency enhancement is even more distinct for the 514 nm beam; the fitting line slope (figure 2.3c) is here 0.44 $\mu m^2(mWs)^{-1}$, even slightly higher than the one at 1064nm, the latter being 0.32 $\mu m^2(mWs)^{-1}$. Depending on the above mentioned threshold behavior, the fitting line does not cross the origin.

Starting from the above considerations, we discuss the observed dynamics and relate it to the optical and geometrical features of the NMPs as well as to the trapping configuration.

The bare NMPs are confined in a plane (2D trapping) near the bottom glass substrate. For this trapping geometry the longitudinal scattering force is reduced while the

transverse gradient force exerted by the laser beam confines the NMPs on its axis, where they spin due to the SAM transfer of the circularly polarized light. Preventing 3D trapping, that would align the ellipsoidal particle along the beam axis [37], the NMPs orient with the major axis parallel to the glass substrate (exhibiting a larger birefringence) and rotate around their minor axis parallel to the beam's one.

On the other hand, we observe that the AuNPs shell significantly alters the entrapment position and the motion of AuNMPs. For the 1064 nm laser source wavelength, where the AuNMPs display an increased reflectance (see spectra in figure 1.7), the scattering force contribution is expected to increase in the propagation direction (wavevector $\boldsymbol{k}$, figure 2.1). Indeed, due to the trap geometry, its transverse component, pointing radially out of the trap, is balanced by the gradient force, pointing toward the beam axis, at the highest light intensity value. This condition determines a new equilibrium position of the particle, out of the beam axis and with the particle major axis oriented radially [38]. The equilibrium distance from the beam axis remains almost unchanged increasing the light intensity within the above-mentioned range, as it mainly depends on the particle's reflectance. Optical forces and trap stiffness as a function of microparticles reflectance has been previously investigated and reported in ref. 39. The numerical simulations assess the stability condition of the optical trap as a function of the reflectance, considering a spherical particle of the same polymer and a radius of 2.5μm. The simulations revealed that in the reflectance range 0.2-0.3, there is a threshold that separates two opposite dynamics passing from attractive to repulsive forces. The behavior of the transverse force for a reflectance below this threshold, is such that the slope of the trapping force calculated at the equilibrium position is in fact always negative. As the reflectance increases, the strength of the trap reduces and an inversion of the slope, which corresponds to an instability condition of the trap, is

expected for higher values. In a narrow region of the reflectance around 0.23 the trap varies from a single stable equilibrium position centered at the beam axis, into two symmetric stable equilibrium positions, at the half maximum of the Gaussian beam intensity. Due to the rotational symmetry of the gradient force in the transverse plane (x, y), those equilibrium positions form an annular region of stable trapping. In the present case, a value of the reflectance giving off axis trapping, is plausible considering the value of the gold refractive index at 1064 nm (n=0.71) and the type of coverage of the NMP (a thin layer of polymer embedded AuNP).

Such AuNMPs trapping is observed until the longitudinal component of the force becomes relevant, after that the particle is expelled from the trap; this effect occurs for light intensities above 2 $mW/\mu m^2$.

The shell reflectance also affects the rotational motion. Due to the circular polarization of the light beam, the particle rotates around its minor axis and contextually moves on a circular trajectory displaying an orbital motion that cannot be accounted for by the OAM of the light beam. A plausible explanation could be put forward considering the optical forces in the transverse plane and the SAM transfer, when the particle starts to rotate it also moves along the orbit, following its equilibrium position in the annular trap. Based on this feature, at any orbit position the particle has the same orientation with respect to the beam center, see figure 2.3a, expressing a synchronous rotation. By consequence, the orbital motion is triggered by the ellipsoidal AuNMPs spinning within the specific trapping potential field.

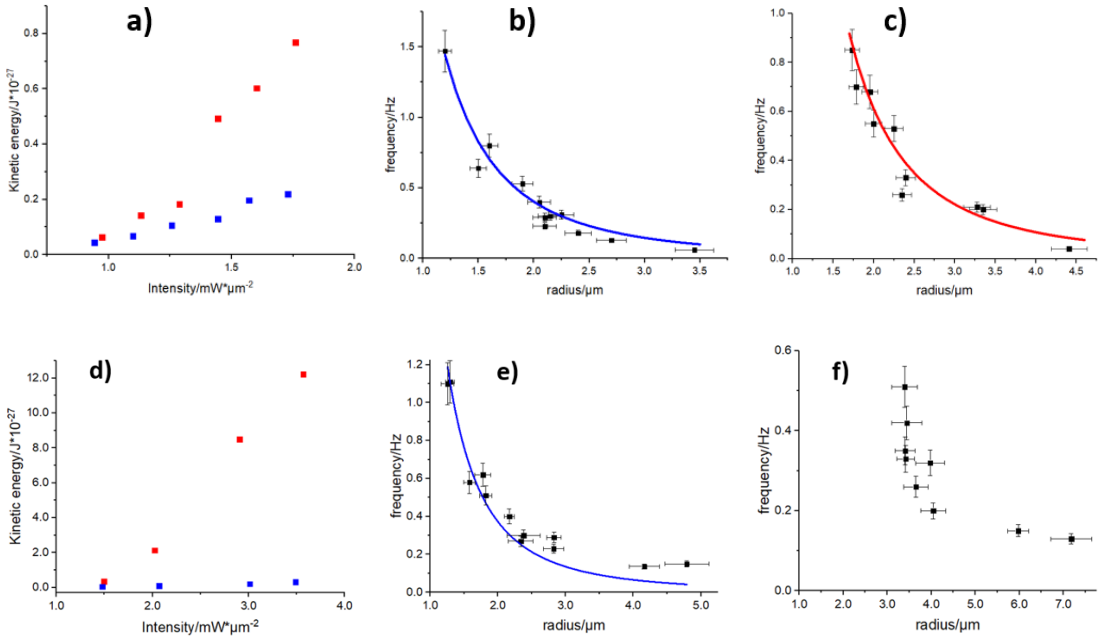

Figure 2.4 a) Rotational kinetic energy of the bare NMPs (blue solid squares) and AuNMPs (red solid squares) as a function of the light intensity at 1064 nm. Rotational frequencies versus particle radius for b) NMPs and c) AuNMPs irradiated at 1064 nm and 1.7 mW/μm^2. d) Rotational kinetic energy of the bare NMPs (blue solid squares) and AuNMPs (red solid squares) as a function of the light intensity at 514 nm. Rotational frequencies versus particle radius for e) NMPs and f) AuNMPs irradiated at 514 nm and 1.7 mW/μm^2. Solid lines represent curve fitting according to eqn. 2.11. The fit parameters used are the following: b): P=50 mW; σ_{in}=0.90; α_{eff}=100 m^{-1}; Δn=0.13. c): P=50 mW; σ_{in}=0.90; α_{eff}=230 m^{-1}; Δn=0.13. e): P=87 mW; σ_{in}=0.90; α_{eff}=120 m^{-1}; Δn=0.16.

In figure 2.4a and 2.4d the kinetic energy as a function of the light intensity, at 1064 nm and 514 nm wavelength respectively, is reported for a bare NMP and a AuNMP, with the same radius (2.8 μm). Although the trend is linear for both NMPs, the slope is steeper for the AuNMPs, suggesting the occurrence of an additional contribution to the optical torque in eqn. 2.10. Since no transfer of angular momentum is expected due to the reflection at the water/AuNMP interface, we can assume that the increased reflectance at the interface between the dielectric core and the AuNPs shell favors a greater circulation of light within the AuNMPs, which is responsible of the increased optical torque, and consequently of the higher rotational frequency with respect to the bare NMPs. Such interpretation is supported by the rotational frequency measurements

of the NMPs and AuNMPs as a function of the particle radius, at 1064 nm laser wavelength and 1.7 mW/μm^2 intensity (see figure 2.4b and 2.4c). As expected from eqn. 2.10, for both particles the rotational frequency is inversely proportional to the NMPs cubic radius and its value is higher for the NMPs covered by the AuNPs. The solid lines in figure 2.5b and 2.5c represent the theoretical fits of the experimental data and have been carried out considering the rigid body approximation, suitable for polymerized NMPs, and two contributions to the optical torque [40], including an effective absorption parameter, α_{eff}, involving the whole particle, in addition to the birefringence. According to ref. 40, the rotational frequency takes the following expression:

$$\nu = \nu_0 \sigma_{in} (1 - e^{-2\alpha_{eff} R} \cos \Delta\varphi)^2 \qquad \text{(eqn. 2.11)}$$

where $\nu_o = {}^{P}/_{2\pi K\omega}$ and $\Delta\varphi = 2kR\Delta n$ is the total birefringence retardation phase, where $k = {}^{2\pi}/_{\lambda_0}$ and Δn is the polymer birefringence.

The fitting curves in figure 2.4b and 2.4c, accounts for an enhanced optical torque associated to a doubled effective absorption (α_{eff} =230 m^{-1}) of the AuNMPs with respect to the NMPs one (α_{eff} =100 m^{-1}), see figure caption. This parameter can be rationalized by a stronger light trapping inside the nematic core, i.e. the circulating light enhancement effect inside a cavity, which results in an increased transfer of SAM. A greater contribution to the rotational frequency of the AuNMPs and, consequently, to the kinetic energy is obtained for the 514 nm laser beam, as shown in figure 2.4d. Moreover, it should be mentioned that the measurements performed as a function of the radius make evidence of an interesting different behavior of the AuNMPs at the two laser wavelengths. The 514 nm laser beam cannot stably trap AuNMPs with a radius lower than 3 μm, which instead experience a repulsive force that pushes them

out of the illuminated area. Considering the reflectance spectra in figure 1.7, the optical properties at 514 nm suggest the optical torque enhancement as the only responsible of the rotational frequency increase due to the photons absorbed by the plasmonic nano-shell, see figure 2.2c and 2.3c. In fact, compared to 1064 nm wavelength, plasmonic resonance and lower reflectance at 514 nm are clearly observed (figure 1.7). In figure 2.4d the acquired rotational kinetic energy as a function of the light intensity is reported for a bare NMP and an AuNMP of comparable size. A more efficient angular momentum transfer from the absorption-mediated process enables to increase the rotational kinetic energy of the core-shell AuNMPs by two orders of magnitude with respect to the bare NMPs.

In figures 2.4e and 2.4f the frequency is reported as a function of the particle's radius. While for bare NMPs the trend is the one described by eqns. 2.9 and 2.10, the AuNMPs exhibit a different behavior, being stably trapped only if their radius is larger than 3 μm. Here, the optical force is expected to have a further contribution due to the transferred liner momentum from the absorbed light, that is opposite to the one due to the refracted rays [1, 30] and reduces the trap stability. Nevertheless, due to the core-shell structure, the absorption process does not involve the whole AuNMPs, but only the nanolayer of the MPs surface including the AuNPs. Hence, for large values of the surface-to-volume ratio (i.e., for smaller particles) at fixed surface density of the AuNP, this contribution prevails, pushing the AuNMPs out of the irradiated region. With the increase of the particle radius this effect reduces, thus enabling stable trapping within an annular region, at even higher light intensity values with respect to the 1064 nm beam, see figure 2.3c.

The absorbed photons, differently from the reflected one, may transfer SAM giving a further contribution to the optical torque applied to the particle [18]. Such contribution

compensates the lower values of the rotational frequency at 514nm, as expected from eqns. 2.10 and 2.11. The graph in figure 2.4c shows that, for particles with 3.2±0.2 μm radius, the optical torque caused by the light absorption at the plasmon resonance gives a contribution about six times larger than the one due to the sole birefringence (bare NMP, figure 2.2c). In addition, the slope of the fitting line is now even steeper than the one at 1064 nm. However, since a very small surface layer of the AuNMPs is involved in the process, a larger effect is expected for particles with higher surface-to-volume ratio. By consequence, particles with a radius just above 3 μm can achieve a larger increase of frequency.

Beside the ones investigated in the present work, a further advantage of the core-shell structure emerged by this investigation is linked to the heating phenomena caused by light absorption. Such side effects must be usually avoided since the structural modifications, that the temperature increase may induce in both the environment and/or the MPs itself, limit the power value that can be used and the rotation rates that can be achieved [41]. Here, the resonant absorption involving the gold NPs in the nanometric shell is able to significantly enhance the optical torque on the MPs, whereas the core-shell structure reduces the temperature rise of the whole particle and improves the heat dissipation processes.

2.2.4 Conclusion

Dielectric-metallic core-shell structure of birefringent MPs enhances the rotational rates and enables further rotational modes in basic Gaussian beam optomechanical setup. The comparative investigation between bare NMPs and AuNMPs, at different beam wavelengths, rationalizes the rotational dynamical features of the latter in term of the optical properties of the AuNPs shell.

The increased reflectance expressed in the near IR region (at 1064 nm) modifies the rotational motion: bare NMPs spin, while the AuNMPs show a synchronous spinning and orbital motion. The efficient absorption expressed in the visible region at the plasmonic resonance of the AuNPs (at 514 nm) also enhances the rotational rates that can be achieved at the same light intensity: the core-shell AuNMPs exhibit a rotational kinetic energy that is two orders of magnitude larger than the bare NMPs one. Finally, the core-shell structure could also represent a useful approach to limit the heating side effects generally linked to the light absorption. Therefore, the reported results reveal a novel strategy to improve the rotational control of microparticles and can have direct implications in applications involving light guided rotating micro-objects, like micromechanics (micromotors and microrotors) and microrehology.

2.3 COLLECTIVE MOTION OF CHIRAL BROWNIAN PARTICLES CONTROLLED BY A CIRCULARLY-POLARIZED LASER BEAM

The focus of this section is on the emergence of circular collective motion in a system of spherical light-propelled Brownian particles. Light-propulsion occurs as consequence of the coupling between the chirality of cholesteric microparticles (CMPs) – left (L)- or right (R)-type – and the circularly-polarized light that irradiates them. Irradiation with light that has the same helicity of the particle material leads to a circular cooperative vortical motion of the chiral Brownian particles. In contrast, opposite circular-polarization does not induce such coupling among the particles but only affects their Brownian motion. The mean angular momentum of each particle has a value and sign that distinguishes between chiral activity dynamics and typical Brownian motion. These outcomes have relevant implications for chiral separation technologies and provide new strategies for optical torque tunability in mesoscopic

optical array systems, micro- and nanofabrication of light-activated engines with selective control and collective motion.

In order to study this particular motion, MPs in the low chirality regime have been selected, where the chiral reflectance is low enough to prevent particle rejection from the trap. This condition occurs for CMPs that have a ratio between radius (a) and pitch of the helix (p) lower than 3, in this situation in fact the reflectivity of the relevant circularly polarized light component, L or R depending on the chiral dopant used, is not complete [42,43,44]. The collective circular motion of j CMPs (with $j \geq 3$) emerges for particles having $a/p \sim 2$ and a sub-micrometric radius [45-46]. We used R-type and L-type particles, as well as non-chiral birefringent (B-type) particles of the same size, under illumination of circularly polarized light; see figure 2.5. Only light with the same helicity of the particles photo-activates the propulsion mode of j CMPs, which organize themselves in a collective circular motion generating a mass of whirling fluid or vortex in a non-inertial fluid. Conversely, CMPs illuminated by light with the opposite circular polarization, as well as non-chiral birefringent particles irradiated by any circularly polarized light, behave as passive Brownian particles; albeit, with effective transport properties induced by the illuminating polarized light.

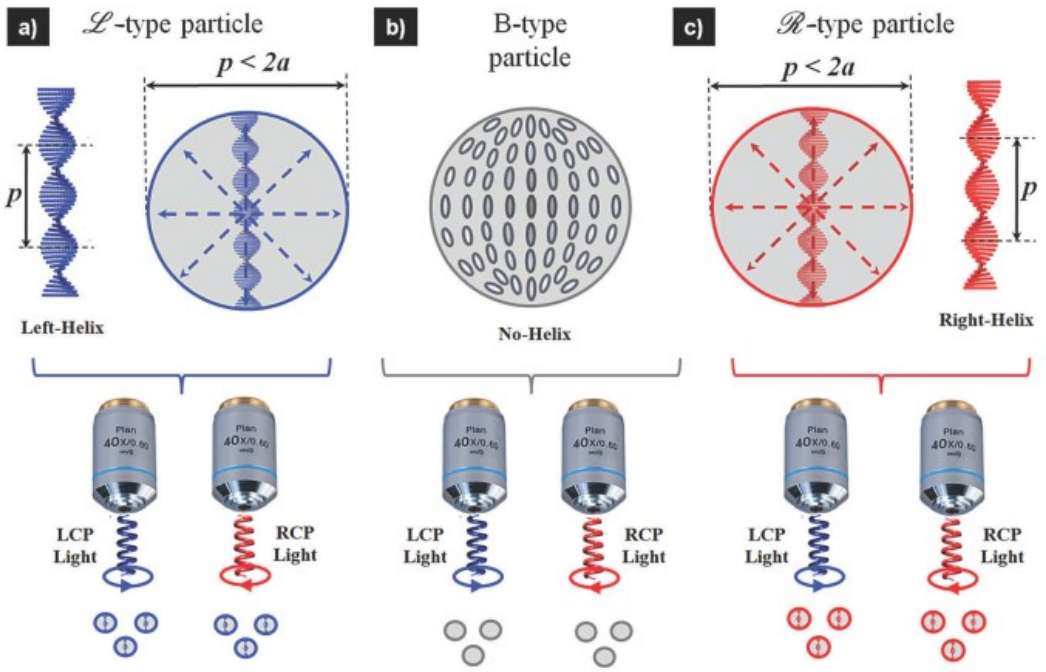

Figure 2.5 Top: Diagram of the molecular internal structure in our three types of spherical particles: (a) L-type CMPs (blue color), (b) B-type non-chiral birefringent particles (gray color), and (c) R-type CMPs (red color), with their corresponding cholesteric pitch p and radius a. Bottom: Representation of the six configurations investigated here for the two circular polarizations, LCP and RCP, and three types of particles.

2.3.1 Experimental Section

We investigated water suspensions of polymeric particles with spherical shape and radius $a \sim 0.5$ μm. The procedure for obtaining B-type nematic particles is that described in section 1.2.1 birefringent microparticles (NMPs), while for L- and R- type chiral particles, reference is made to 1.2.2 chiral microparticles (CMPs). As described in the 1.2.2, chiral particles self-organize in supramolecular helicoidal structures of mesogenic units with the same chirality of the dopant. The latter are characterized by a spatial periodicity (pitch, p) that depends on the fraction of the chiral dopant added to the mesogenic blend. In this case p ~ 330 nm, which corresponds to a selective reflection band in the range of 470–500 nm. Even in the low chirality regime (a/p ~ 1), onion-shell shaped cholesteric layers form with a radial configuration of the helical

axes (figures 2.5a and 2.5c). The samples are obtained by centrifugation and filtering of the suspensions, removing particles with a radius larger than 0.5 μm. The suspension is confined into a micro chamber made by a microscope slide, 150 μm spacers and a coverslip.

The collective rotating motion of the Brownian particles in water suspension under irradiation of circularly polarized light, has been investigated by video microscopy (the experimental setup is the same of the 2.3.1 section, depicted in Figure 2.1), but in this case an Ar^+ laser TEM 00 beam with wavelength of 488 nm is used to illuminate the suspensions through a 40X microscope objective (N.A. 0.65), with 20 $mW*\mu m^{-2}$ intensity at the sample. A dichroic mirror (DM) reflects the laser beam and a quarter wave-plate (QWP) is placed before the objective to set the circular polarization light state (LCP or RCP).

ImageJ (http://imagej.net) and Tracker (http://physlets.org/tracker/) software have been used to analyze the images captured from the video and to extract the position of $\vec{r}_i^{\,j} = x_i^j\hat{x} + y_i^j\hat{y}$ the j^{th} particle tracked in the experiments at the i^{th} time step with respect to the initial center of mass.

2.3.2 Results and discussion

When three L-type CMPs are illuminated with LCP light, they exhibit an intermittent clockwise (cw) circular motion within the illuminated region (see figure 2.6a–c, sequence from video Video_3.mp4 at the link https://drive.google.com/drive/folders/1ckO2wfEhVpV5GMVElV41S0VvoMvYzUxb?usp=sharing), resulting in a collective vortex. Later, when the light is switched to RCP (figure 2.6d–f, sequence from video Video_4.mp4 at the link https://drive.google.com/drive/folders/1ckO2wfEhVpV5GMVElV41S0VvoMvYzUx

b?usp=sharing), the vortical motion stops and each individual particle moves approximately as a passive Brownian particle following a confined random walk.

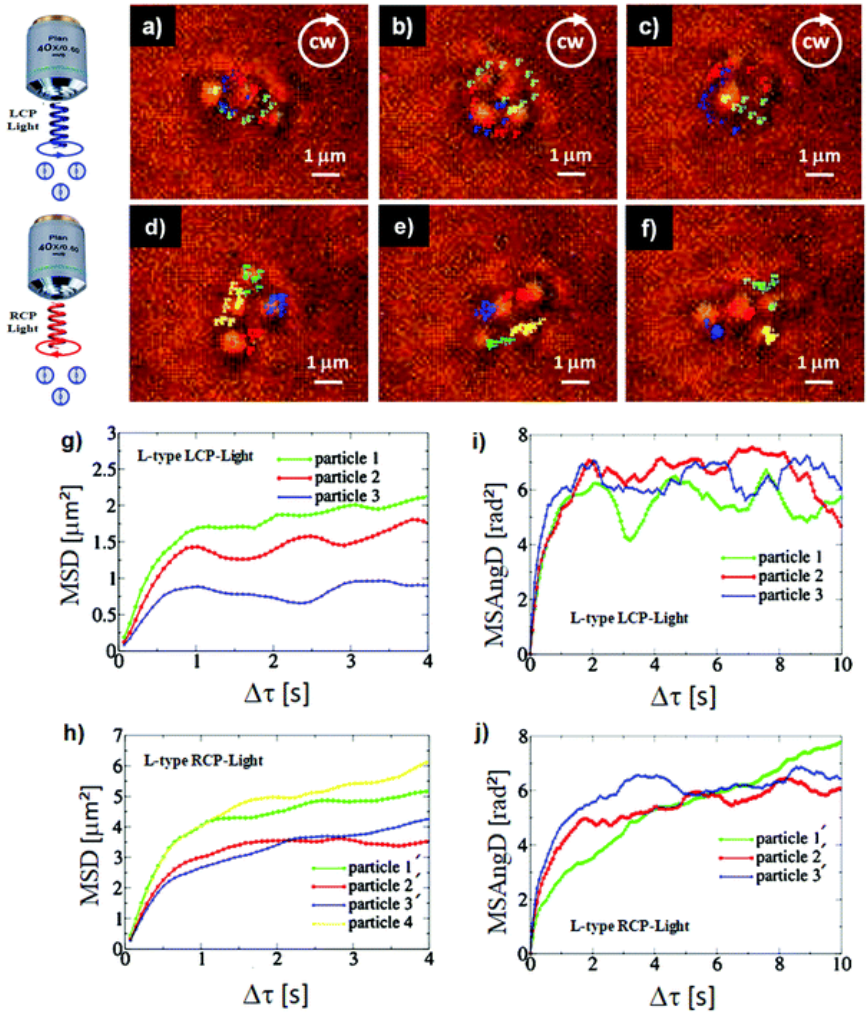

Figure 2.6. Three types of chiral particles; each frame shows the last 15 steps in time (Δt = 0.071 s), indicating the position of each particle by color: green (particle 1), red (particle 2) and blue (particle 3). (a)–(c) Image sequence for LCP light at t_a = 10.2 s; t_b = 21.8 s, and t_c = 31.1 s (see Video 3, link in the text), clockwise rotation (cw) and mean orbital radius r = 1.15 ± 0.18 µm. (d)–(f) Mean square displacement graphic for each particle; image sequence for the same particles now illuminated by RCP light at t_d = 10.2 s, t_e = 21.3 s, and t_f = 31.0 s (see Video 4, link in the text). Mean square displacement graphics for each particle with (g) LCP and (h) RCP light and their corresponding mean square angular displacement graphics (i) and (j).

For the three R-type CMPs, the situation is reversed, i.e. no rotational motion occurs when they are illuminated with LCP light and instead of collective motion, a thermal-like diffusion is observed (figure 2.7a–c, sequence from video Video_5.mp4 at the link https://drive.google.com/drive/folders/1ckO2wfEhVpV5GMVElV41S0VvoMvYzUxb?usp=sharing), while RCP light now induces a collective vortical rotation in the ccw sense (figure 2.7d–f, sequence from video Video_6.mp4 at the link

https://drive.google.com/drive/folders/1ckO2wfEhVpV5GMVElV41S0VvoMvYzUxb?usp=sharing).

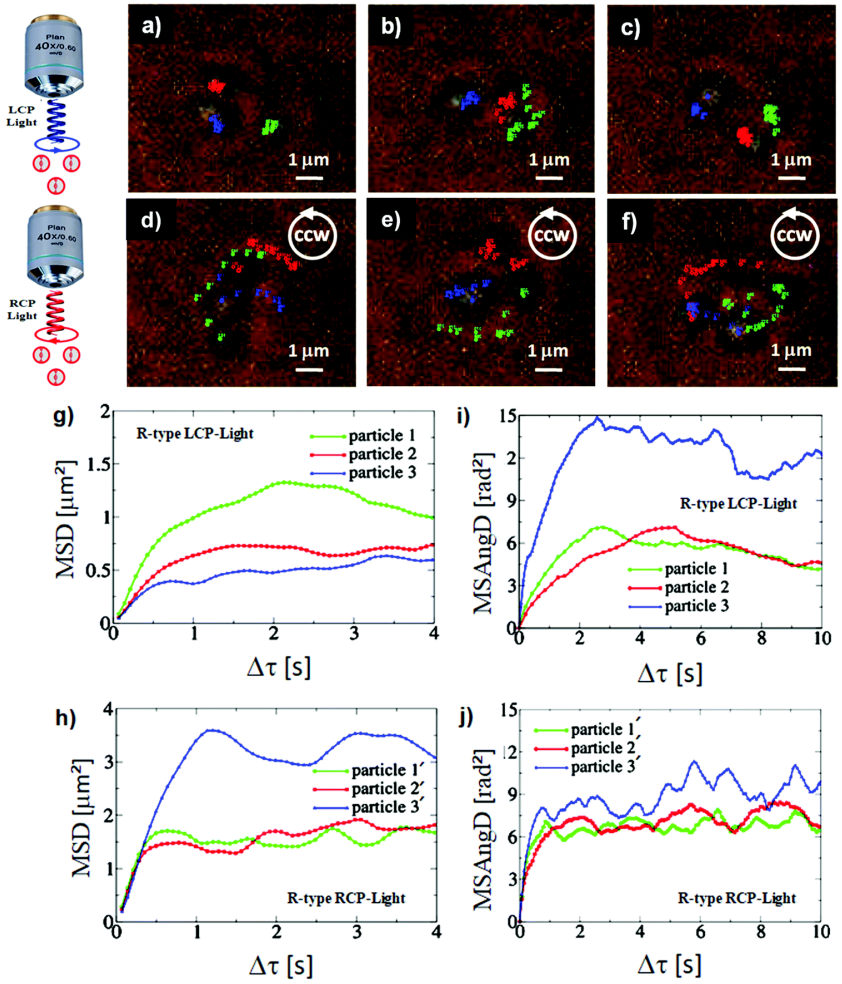

Figure 2.7 Three R-type chiral particles; each frame shows the last 15 steps in time ($\Delta t = 0.071$ s), indicating the position of each particle by color: green (particle 1), red (particle 2) and blue (particle 3). (a)–(c) Image sequence for LCP light at $t_a = 10.1$ s; $t_b = 19.7$ s, and $t_c = 26.6$ s, (see Video 5, link in the text). (d)–(f) Mean square displacement graphic for each particle; image sequence for the same particles now illuminated by RCP light at $t_d = 10.8$ s, $t_e = 19.6$ s, and $t_f = 26.8$ s (see Video 6, link in the text), counterclockwise rotation (ccw) and mean orbital radius $r = 1.47 \pm 0.28$ µm. Mean square displacement graphics for each particle with (g) LCP and (h) RCP light and their corresponding mean square angular displacement graphics (i) and (j).

The same investigations have been performed employing suspensions of NMPs (figures 2.8a–c and 2.8d-f, sequence from videos Video_7.mp4 and Video_8.mp4 at the link https://drive.google.com/drive/folders/1ckO2wfEhVpV5GMVElV41S0VvoMvYzUxb?usp=sharing). In the case of NMPs, no cooperative motion is observed for each circular polarization state of light (LCP or RCP). These results clearly reveal the

essential nature of the coupling between the chirality of the particles and the circular polarization of light for the emergence of a cooperative phenomenon, namely collective rotational motion.

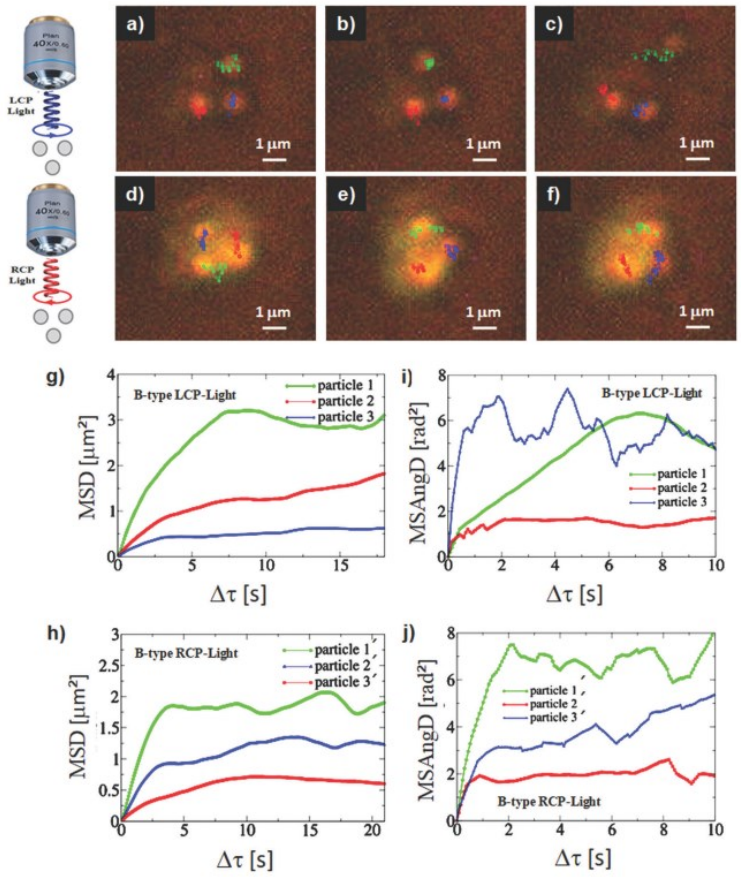

Figure 2.8. Three B-type non-chiral particles; each frame shows the last 15 steps in time (Dt = 0.071 s), indicating the position of each particle by color: green (particle 1), red (particle 2) and blue (particle 3). (a)–(c) Image sequence for LCP light at t_a = 10.1 s, t_b = 20.3 s, and t_c = 30.6 s (see Video 7, link in the text). (d)–(f) Mean square displacement graphic for each particle; image sequence for the same particles now illuminated by RCP light at t_d = 9.6 s, t_e = 20.2 s, and t_f = 29.8 s (see Video 8, link in the text). Mean square displacement graphics for each particle with (g) LCP and (h) RCP light and their corresponding mean square angular displacement graphics (i) and (j).

In the absence of illumination, the particles of any type (L-CMPs, R-CMPs or NMPs), diffuse in water with an expected Stokes-Einstein diffusion coefficient:

$$D_B = \frac{k_B T}{6\pi\eta a} \qquad \text{(eqn. 2.12).}$$

T and η are the temperature and viscosity of the fluid, respectively, and k_B is the Boltzmann constant; for the particles considered here ($a \sim 0.5$ µm), $D_B \simeq 0.4$ µm^{2}s^{-1} at room temperature.

From single trajectory analysis [47], the mean-squared displacement (MSD), or $\langle r^2(\Delta\tau)\rangle$ [32,39], as function of time lag Δt is obtained for the particles considered in the present study. Graphics (g) to (j) of figures 2.6–2.8 show the effects of the coupling between the particle chirality and circularly-polarized light on the diffusive properties of the particles. The primed numbers in both the MSD and MSAngD graphs are for labeling purposes only, since the particles are indistinguishable; therefore, particle 1 is not the same as particle 1', and so on. However, in our experimental implementation we have a polydisperse particle collection, resulting in similar sizes but slightly different levels of chiral coupling with light. We observe that for both types of chiral particles, light-polarization defines the time dependence of the MSD in two aspects. The first refers to the effective diffusion coefficient of the particles, which can be extracted from the slope of the MSD in the linear regime (short-time regime, $\Delta t < 1s$), and differs from the characteristic value of 0.4 $\mu m^2 s^{-1}$ of thermal Brownian motion. NMPs, on the other hand, show a different trend in the MSD, mainly due to the lack of chiral photo-activation.

The other aspect featured in the MSD refers to a stationary-like regime ($\Delta t \geq 1s$), which is characteristic of confined motion. In this time regime, two subtle features of the MSD are revealed. On one hand, oscillations around a well-defined saturation value (as shown in figures 2.6g–2.7h) encode the information of the intermittent circular motion performed by the particles when the collective dynamics, due to the coupling between the particle chirality and the polarization of circularly-polarized light, is turned on. These oscillations are well distinguished from the smooth fluctuations around the saturation value observed in the absence of such coupling (see figures 2.6h–2.7g). These fluctuations are observed in the MSD of a variety of confined particles [48,49] and might originate from the method of calculation of the MSD, as a single

trajectory for each particle is used for computation. The time average on a time window in this regime gives the average distance of the particles from the trap center and must be interpreted differently depending on the case under consideration. For the cases of L-type CMPs illuminated with LCP light and R-type CMPs illuminated with RCP light, this distance corresponds to the radius of the particles' orbital motion, which is somewhat larger than one particle's diameter. In figure 2.6a–c it can be noted that the L-type CMPs that perform circular motion (those under LCP light) are more confined than those illuminated with RCP light (figure 2.6d–f). For the cases of L-type CMPs illuminated with RCP light and R-type CMPs illuminated with LCP light, this average distance corresponds to the traveling distance of the particles that diffuse under illumination. For the B-type particles (shown in figure 2.8), a conspicuous difference in the confinement without collective orbital motion is noted.

In addition, the mean squared angular displacements (MSAngD) of the particle trajectories for each type are shown in graphics (i) and (j) in figure 2.6–2.8. The angles (φ_i), given in radians, are determined by the direction of the radius vector of the particle position at the instant $t_i = i\Delta t$ with respect to the particle's center of mass, which defines the origin of the Cartesian system of coordinates. Angles are measured with respect to the x-axis, increasing in the anti-clockwise sense. $\Delta t = 0.071$ s denotes the time lapse between data points. The radius r_i is simply the magnitude of this vector. Thus, for each particle trajectory, the MSAngD at t_i is given by $\overline{\phi_i^2} - \bar{\phi}_i^{\,2}$, where $\overline{\phi_i^2} = \frac{1}{N_j}\sum_j(\phi_{j+i} - \phi_j)^2$ and $\bar{\phi}_i^{\,2} = \frac{1}{N_j}\sum_j(\phi_{j+i} - \phi_j)$, with N_j the number of data points considered to have appropriate statistics [47].

The complex interdependence between the particle structure and the polarization of light is evidenced again in all graphics in figures 2.6–2.8. For the CMPs, when

illuminated with circularly polarized light with the same chirality as the particles, oscillations in the MSAngD are observed coherently with MSD in figures 2.6 and 2.7.

2.3.3 Angular momentum

The activation of chirality can be revealed and assessed by considering that the rotational active fluctuations do not average to zero but to a finite, constant value, which gives a fixed direction of particles rotation. Based on this assumption, in order to support the above experimental observations, the angular momentum per unit of mass, L_z of each particle has been evaluated for all three different particle type suspensions and the two circular polarization states of light.

$L_z^j(i) = x_i^j \frac{\Delta y_i^j}{\Delta t} - y_i^j \frac{\Delta x_i^j}{\Delta t}$ has been calculated for each particle, where $\Delta x_i^j = x_{i+1}^j - x_i^j$, and $\Delta y_i^j = y_{i+1}^j - y_i^j$. Finally, the mean value of the angular momentum for the j^{th} particle (i.e., R-type, L-type or NMPs) for different polarization states of light irradiation (LCP or RCP) has been evaluated as $\overline{L_z^j} = \frac{1}{N-1}\sum_{i=1}^{N} L_z^j(i)$, where N is the total number of steps, and reported in Table 1.

Table 1 Mean angular momentum for circular polarization

Particle type	$\bar{L}_z^j$ (μm² s⁻¹) for RCP	$\bar{L}_z^j$ (μm² s⁻¹) for LCP
$\mathscr{R}$-Particle 1	−0.97 ± 0.05	0.24 ± 0.10
$\mathscr{R}$-Particle 2	−0.67 ± 0.10	0.02 ± 0.08
$\mathscr{R}$-Particle 3	−0.53 ± 0.10	0.09 ± 0.10
$\mathscr{L}$-Particle 1	0.02 ± 0.15	0.78 ± 0.10
$\mathscr{L}$-Particle 2	−0.12 ± 0.12	0.43 ± 0.06
$\mathscr{L}$-Particle 3	−0.05 ± 0.14	0.73 ± 0.08
$\mathscr{L}$-Particle 4	−0.14 ± 0.13	—
B-Particle 1	−0.20 ± 0.08	−0.29 ± 0.08
B-Particle 2	0.01 ± 0.02	−0.04 ± 0.02
B-Particle 3	−0.21 ± 0.06	−0.01 ± 0.04

In the case of the three R-type particles irradiated with RCP light, the angular momentum of each particle is negative (see Table 1), in agreement with the counterclockwise (ccw) cooperative vortical motion. In contrast, when the same three

R-type CMPs are irradiated with LCP light, the angular momentum of each particle is close to zero.

Similarly, the experimental investigations show that each L-type CMPs in suspension irradiated with left circular polarization (LCP) has positive angular momentum (Table 1). When these are irradiated with RCP light, L-type CMPs behave as passive Brownian particles with zero mean angular momentum.

Photo-activated chirality as the propulsion mechanism also manifests itself in collective behavior, i.e. in the formation of rotating collective motion in a non-inertial fluid. The sense of rotation is either clockwise (cw) or counterclockwise (ccw) and the measured mean angular momentum of the particles exhibits the opposite sign for particles with opposite chirality.

Conversely, chiral particles illuminated by light with opposite circular polarization, as well as non-chiral birefringent particles irradiated by any other polarized light, undergo simple thermal random motion with zero measured mean angular momentum. The reported results demonstrate that the circular motion is not merely due to the spin angular momentum transfer from light to matter but relies on the coupling from the activated Brownian microparticles. Based on their chiral supramolecular structure, they take energy from the environment (i.e., scattered light with proper polarization from other particles), converting it into enhanced motion with circular trajectories in 2D and helicoidal trajectories in 3D. No simple transfer of spin angular momentum from light to particles can be responsible for the roto-translational motion; otherwise, it should also be observed for B-type particles illuminated by circularly polarized light [19], and the rotational contribution should be imposed by the light's chirality. However, under the present experimental conditions the electro-magnetic coupling

between the light and the birefringent particles seems to be negligible and does not affect Brownian motion.

The results for chiral particles corroborate the relevance of optical activity in the process. Their spherical shape rules out any involvement of particle shape in the observed roto-translational motion. The absence of the effect upon illuminating the chiral suspension with opposite circular polarization indicates the passive role of the particle.

2.3.4 Optical torque

More evidence that the photo-activated chirality in the propulsion mechanism manifests itself as a cooperative phenomenon, suggests that each particle should take momentum from the surrounding particles. The particles illuminated by light with proper circular polarization interact with each other, imparting forces and torques coming from the scattered/reflected light that, founded on the material's chirality, preserves its handedness. Based on this assumption, we consider the total optical torque on the collective system composed by J irradiated particles, $\overrightarrow{\Gamma_{Total}}$, as the sum of two terms:

$$\overrightarrow{\Gamma_{Total}} = \overrightarrow{\Gamma_{Int}} + \sum_{i=1}^{J} \overrightarrow{\Gamma_{rad}}^{\pm} \qquad \text{(eqn. 2.13).}$$

The first term $\overrightarrow{\Gamma_{Int}}$ is the optical torque due to the interactions of the scattered/reflected light between the J neighbor particles (in our case J = 3 or 4). The second term is the radiation torque due to the direct transfer of SAM from the light to each particle. As reported in ref. 42 and 43, depending on the particle chirality, opposite circularly polarized light propagates. Circularly polarized light with same helicity and wavelength within the selective reflection band can be strongly reflected from the particle preserving its helicity upon reflection, in contrast to a conventional mirror.

The reflectance can reach a value of 100% and depends on the particle's size, specifically on the ratio of a/p [42,44]. Based on the chiral reflectance, the radiation torque on a single particle in the plane perpendicular to the rotation axis is given by:

$$\overrightarrow{\Gamma_{rad}} = \frac{P}{\omega}\{R^{\pm}(1 \pm sin2\varphi)\}\hat{z} \qquad \text{(eqn. 2.14)}$$

where + refers to a left-handed and - to a right-handed particle, P is the power of the beam and ω is the angular frequency of the radation; φ is the ellipticity angle of the light (φ = 0 or π/2 indicates a linearly polarized beam and φ = ±π /4 indicates circularly polarized light, LCP or RCP, respectively).

Figure 2.9 shows the expected optical torque on a single particle according to eqn. 14. The reflectance has been calculated by exploiting the material's parameters for a particle with radius a = 500 nm and pitch p = 330 nm at λ = 488 nm, obtaining a value of $R^{\pm}$ = 0.10 calculated from $R = \left| tanh \frac{\sqrt{2}\pi(n_{\parallel}^2 - n_{\perp}^2)a}{3\lambda(n_{\parallel}^2 - n_{\perp}^2)^{1/2}} \right|^2$ (according to ref.43)

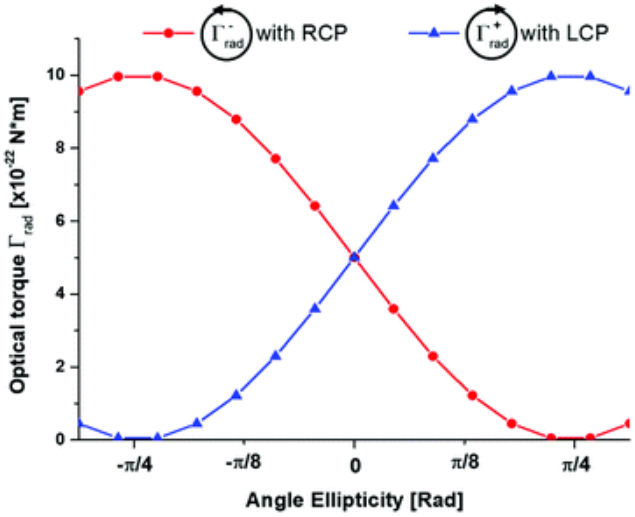

Figure 2.9 Optical torque on a single particle $\overrightarrow{\Gamma_{rad}}$ with opposite reflectivities R^+, R^- versus ellipticity angle φ. With radius a = 500 nm and pitch p = 330 nm at λ = 488 nm, P = 20 μW and $R^{\pm}$ = 0.10.

$\overrightarrow{\Gamma_{total}}$ can be evaluated from the experimental data by employing the method reported in ref. 39 for a single particle, extending it to the case of J particles. The absolute value of the torque is found from the auto- and cross-correlation functions of the particle's coordinates. According to ref. 39, we firstly consider a spherical particle on which an external torque is exerted. It will rotate around the $\hat{z}$ axis with constant angular velocity Ω, whose value results from the balance between the external torque applied to the sphere and the drag torque: $\overrightarrow{\Gamma_{drag}} = \vec{r} \times \overrightarrow{F_{drag}} = -\gamma\vec{r} \times \vec{v} = \gamma\vec{r} \times (\vec{r} \times \vec{\Omega})$, where $\vec{r}$ is the sphere's position, $\vec{v}$ is its linear velocity, γ = 6πaη is the friction coefficient. Hence, the force acting on the sphere from the torque source is given by $\vec{F} = (\gamma\vec{r} \times \vec{\Omega})$, which depends on the position of the spherical particle. A time average of the torque exerted on the particle can be expressed as

$$\langle\vec{\Gamma}\rangle = \langle\gamma\vec{r} \times (\vec{r} \times \vec{\Omega})\rangle = \gamma\langle\Omega r^2\rangle = \gamma\Omega\langle r^2\rangle \qquad \text{(eqn. 2.15)}$$

where $\langle r^2 \rangle$ is the mean square displacement (MSD) of the particle in the plane orthogonal to the torque.

Based on the above considerations, the torque due to particle interactions has been evaluated from eqn.2.13. In the case of R(L)-type particles, illuminated with R (L) circular polarization, the exerted radiation torque is $\sum_{i=1}^{J} \overrightarrow{\Gamma_{rad}}^{\pm} = 3\overrightarrow{\Gamma_{rad}}^{\pm}$ for 3 identical particles, where $\overrightarrow{\Gamma_{rad}}^{\pm}$ = (1.75 ± 0.20) × 10^{-21} Nm is evaluated from eqn. 2.14 for a particle with radius *a* = 500 nm.

From the data extracted by the sequence in figure 2.7d-f (R-type CMPs in RCP light) the rotation period T and the orbital radius, $r_{orb,}$ of each particle is obtained: T_1 = 3.1 ± 0.3 s, r_{orb1} = 1.3 ± 0.1 μm (green), $\langle r_1^2 \rangle = 1.56\ \mu m^2$; T_2 = 2.6 ± 0.3 s, r_{orb2} = 1.5 ± 0.2 μm (red), $\langle r_2^2 \rangle = 1.66\ \mu m^2$; T_3 = 2.4 ± 0.3 s, r_{orb3} = 1.6 ± 0.3 μm (blue), $\langle r_3^2 \rangle = 3.28\ \mu m^2$. According to eqn. 2.15 these values are used to evaluate the total torque

$\overrightarrow{\Gamma_{Total}} = \overrightarrow{\Gamma_1} + \overrightarrow{\Gamma_2} + \overrightarrow{\Gamma_3}$ exerted on the particle system. The measured value of $\overrightarrow{\Gamma_{Total}}$ is larger than that due to the direct transfer of SAM from light, giving a non-negligible value for the interaction torque of $\overrightarrow{\Gamma_{Int}} = (6.24 \pm 0.50) \times 10^{-19}$ Nm.

The observed effect shows some similarities with an interesting phenomenon recently postulated [50,51] but with a limited number of experimental demonstrations, where the optical torque can be strongly controlled and even switched from positive to negative [12]. One of these experiments exploits mesoscale optical matter consisting of arrays of interacting silver nanoparticles in circularly polarized optical beams. Depending on the light wavelength, number of interacting particles, inter-particle separation, geometry and symmetry of the array, physical parameters such as the size, shape and material of the particles, the system offers great tunability of the experienced optical torque. The physical origin of the effect lies in the fields scattered by the particles that exert a recoil optical torque. In the present case, due to the chiral reflection from the particles, torque amplification could be produced by the interference of the scattered/reflected fields.

2.3.5 Model and numerical simulations

In order to determine the parameters that regulate the motion of the system, a model based on the Langevin equations has been proposed by Prof. F. J. Sevilla in [45]. The single-particle trajectories, $\overline{r}(t) = (x(t), y(t))$, of active rotational motion induced by the coupling between the particle chirality and the handedness of the circularly-polarized light, can be simulated by a simple model expressed by:

$$\frac{d}{dt}\vec{r}(t) = \Lambda\vec{\Omega} \times \left[\hat{v_s}(t) \times \hat{\Omega}\right] - \mu\vec{r}(t) + \xi_N(t) \qquad \text{eqn. 2.16a,}$$

$$\frac{d}{dt}\hat{v_s}(t) = \vec{\Omega} \times \hat{v_s}(t) \qquad \text{eqn. 2.16b.}$$

The coupling between light and the particle chirality is contained in the angular velocity $\vec{\Omega}$. On one hand, it models the propelling "force" through the first term of eqn.2.16a, where Λ is a parameter of the model that gives the particle swimming speed via $\Lambda\Omega$. On the other hand, it rotates the swimming direction eqn.2.16b denoted by the vector $\hat{v_s}(t)$, giving rise to rotational motion. Ω is set to zero when the particle chirality is opposite to the rotation sense of the circularly polarized light, since no coupling is observed.

The second term on the right-hand side of eqn.2.16a accounts for the optical trapping force and is modeled by a linear restitutive force. μ is the ratio of the restitution coefficient divided by the particle mobility, which accounts for the surrounding fluid viscosity defined as the ratio of the diffusion coefficient to the thermal energy, i.e., $\mu = \frac{D_B}{k_B T}$. $\xi_N(t)$ are modeled as three-dimensional vectors with Gaussian white noise components, i.e., their entries satisfy $< \xi_N(t) > = 0$ and $< \xi_{N\mu}(t)\xi_{N\upsilon}(s) > = 2D_B\delta(t-s)\delta_{\mu,\upsilon}$; where greek sub-indices denote vector components. As before, D_B is the diffusion coefficient due to thermal fluctuations of surrounding fluid.

We restrict both eqns. 2.16 to the case when the motion occurs on the plane and therefore consider $\vec{\Omega} = \Omega\hat{k}$, where $\hat{k}$ is a unit vector that points perpendicularly to the plane of motion. $\vec{\Omega}$ gives the angular velocity of the swimming vector that emerges as a consequence of the coupling between the particle's chiral structure (R or L) and the light polarization (RCP or LCP). In the plane of motion, $\hat{v_s}(t) = [\cos\theta(t), \sin\theta(t), 0]$, thus the set of eqns. 2.16 can be rewritten as:

$$\frac{d}{dt}x(t) = \Lambda\Omega\cos\theta(t) - \mu x(t) + \xi_{Nx}(t) \qquad \text{(eqn. 2.17a),}$$

$$\frac{d}{dt}y(t) = \Lambda\Omega\cos\theta(t) - \mu y(t) + \xi_{Ny}(t) \qquad \text{(eqn. 2.17b)},$$

$$\frac{d}{dt}\theta(t) = \Omega \qquad \text{(eqn. 3.17c)}.$$

If the positions are scaled with length Λ and time with Ω, it is possible identify two independent ratios: $Pe = \Lambda^2\Omega/D_B$, which measures the effects of thermal fluctuations against those of the propelling mechanism and can be identified with the Péclet number; and the ratio μ/Ω which characterizes the effects of the optical trapping intensity.

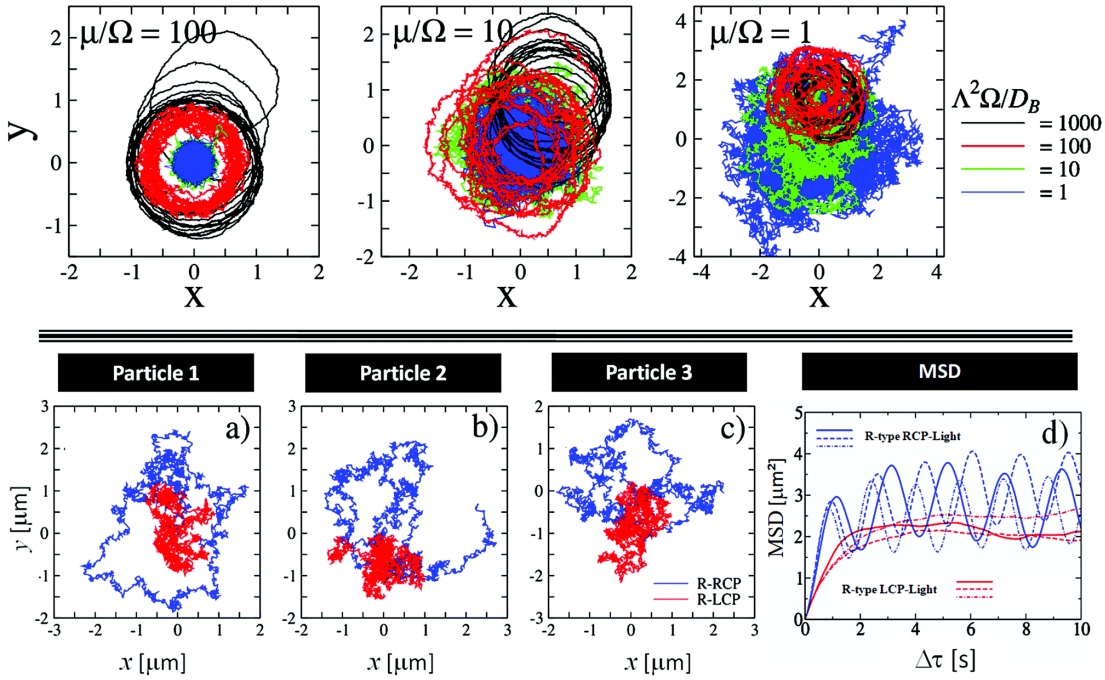

Figure 2.10 Top: Trajectories obtained from numerical integration of eqn. (2.16a) for particles moving counterclockwise for different values of the trapping parameter μ/Ω:100 (strongly trapped particles), 10 (mildly trapped particles), 1 (weakly trapped particles). In each case, different values of the Péclet number $\Lambda^2\Omega/D_B$ are considered, namely 1000 (black lines), 100 (red lines), 10 (green lines), and 1 (blue lines). Bottom: (a)–(c) Trajectory numerical simulations using our experimentally obtained data for each of the three R-type particles with RCP & LCP light; (d) corresponding MSD graphics.

In the upper panels of figure 2.10, the simulated trajectories obtained from the numerical integration of eqn. 2.16a for different values of *Pe* and μ/Ω are presented.

In particular, the case for R-type particles coupled with RCP light is presented (the same as presented in figure 2.7d-f. When the propulsion is apparent, i.e. for large values of *Pe*, well-defined circular trajectories are observed (see black and red lines in figure 2.10 for *Pe* = 1000 and 100, respectively). On the contrary for low Péclet values, the coupling between the light polarization decreases. For (*Pe* = 1 and 10 blue and green lines in figure 2.10), the particle motion is dominated by thermal fluctuations and the optical trapping effect, since propulsion is negligible. Thus, motion is highly trapped for $\mu/\Omega = 100$ and the trajectories become practically Brownian for $\mu/\Omega = 1$.

For comparison and validation of the theoretical model (eqn. 2.16), the trajectory was simulated for R-type particles (see lower panels of figure 2.10) by using the experimental data obtained for each of the three particles. From the data when particles are irradiated by RCP light, trajectories that exhibit circular motion (blue lines) are obtained. $\Lambda\Omega$ is evaluated from the periods of the orbits of the particle trajectories: $\Lambda\Omega_1 = \Lambda 2\pi/T_1 = 2.0\ \mu ms^{-1}$, $\Lambda\Omega_2 = \Lambda 2\pi/T_2 = 2.4\ \mu ms^{-1}$, $\Lambda\Omega_3 = \Lambda 2\pi/T_3 = 2.6\ \mu ms^{-1}$, where $\Lambda = 0.667\ \mu m$. From the experimental particle trajectories, for which the particle chirality is opposite to the circular polarization of light, μ^{-1} is estimated as ~ 0.9 s. For the same three particles when illuminated with LCP light, we have $\mu/\Omega = 0$. The simulated trajectories look predominantly Brownian (red lines). From the simulated trajectories we have also computed the MSD as function of time (shown in figure 2.10d), where the oscillatory behavior due to circular motion is markedly clear for particles irradiated with RCP light (blue lines). The obtained curves from the simulations of each particle exhibit an analogous trend and a similar number of oscillations during the same time interval $\Delta\tau$ as presented in figure 2.7g and h. Indeed, considering the measured rotation frequencies in the range of 0.4–0.3 s^{-1}, their values are compatible with the number of oscillations as observed in both MSD (experimental data and simulation) graphs in the

stationary-like regime, i.e. 2 - 2.5 oscillations in the time interval $1s \leq \Delta\tau \leq 4\,s$. When the particles are irradiated with LCP light, the simulated smooth fluctuations around the saturation value of Brownian motion are also observed (red lines). These results reveal the two polarization dependent behaviors.

CONCLUSION

In conclusion, it is investigated the remote switching of spherical Brownian particles from a passive status to a collective organized chiral-active status just by means of circular light polarization. The experiment was performed using polymeric particles based on chiral chemical compounds with a spherical shape in order to avoid phenomena connected to the breaking of left–right symmetry due to mass or shape anisotropies. This method enables the identification of the presence of opposite chiral structures, since the material's structural helicity determines the clockwise or counterclockwise sense of rotation in a circular trajectory. Spherical birefringent microparticles have been also investigated in order to compare the role of the active chiral particles with respect to non-chiral Brownian particles by spin angular momentum transfer from light. Moreover, the capability to generate flexible highly localized light fields by using suitable optical elements (microscope objectives, lenses, waveplates, filters, etc.) can simplify active behaviors, such as collaborative tasks among small groups of microswimmers. The reported findings have the potential to add new reversible capabilities and enhanced functionalities activated by the polarized light states to applications involving controlled micro- and nanomotors, chiral sorting [52,53] and transport phenomena in colloidal systems.

References

1. Ashkin, A. Acceleration and Trapping of Particles by Radiation Pressure. Phys. Rev. Lett. 1970, 24 (4), 156–159. https://doi.org/10.1103/PHYSREVLETT.24.156.
2. Dholakia, K.; Čižmár, T. Shaping the Future of Manipulation. Nat. Photonics 2011, 5 (6), 335–342. https://doi.org/10.1038/nphoton.2011.80.
3. Spesyvtseva, S. E. S.; Dholakia, K. Trapping in a Material World. ACS Photonics 2016, 3 (5), 719–736. https://doi.org/10.1021/ACSPHOTONICS.6B00023.
4. Corsetti, S.; Dholakia, K. Optical Manipulation: Advances for Biophotonics in the 21st Century. 2021, 26 (7), 070602 https://doi.org/10.1117/1.JBO.26.7.070602.
5. Gao, D.; Ding, W.; Nieto-Vesperinas, M.; Ding, X.; Rahman, M.; Zhang, T.; Lim, C. T.; Qiu, C. W. Optical Manipulation from the Microscale to the Nanoscale: Fundamentals, Advances and Prospects. Light Sci. Appl. 2017, 6 (9), e17039–e17039. https://doi.org/10.1038/lsa.2017.39.
6. Leach, J.; Mushfique, H.; Di Leonardo, R.; Padgett, M.; Cooper, J. An Optically Driven Pump for Microfluidics. https://doi.org/10.1039/b601886f.
7. Williams, I.; Oğuz, E. C.; Speck, T.; Bartlett, P.; Löwen, H.; Patrick Royall, C. Transmission of Torque at the Nanoscale. Nat. Phys. | 2016, 12. https://doi.org/10.1038/NPHYS3490.

8. Glückstad, J.; Palima, D. Light Robotics-Structure-Mediated Nanobiophotonics. 2017.
9. Aubret, A.; Martinet, Q.; Palacci, J. Metamachines of Pluripotent Colloids. Nat. Commun. 2021, 12 (1), 1–9. https://doi.org/10.1038/s41467-021-26699-6.
10. Zhang, S.; Elsayed, M.; Peng, R.; Chen, Y.; Zhang, Y.; Peng, J.; Li, W.; Chamberlain, M. D.; Nikitina, A.; Yu, S.; Liu, X.; Neale, S. L.; Wheeler, A. R. Reconfigurable Multi-Component Micromachines Driven by Optoelectronic Tweezers. Nat. Commun. 2021, 12 (1), 1–9. https://doi.org/10.1038/s41467-021-25582-8.
11. Zhang, S.; Nan, F.; Neale, S. L. Light-Driven Microrobots: Mechanisms and Applications. Field-Driven Micro Nanorobots Biol. Med. 2022, 91–111. https://doi.org/10.1007/978-3-030-80197-7_4.
12. Han, F.; Parker, J. A.; Yifat, Y.; Peterson, C.; Gray, S. K.; Scherer, N. F.; Yan, Z. Crossover from Positive to Negative Optical Torque in Mesoscale Optical Matter. Nat. Commun. 2018, 9 (1), 1–8. https://doi.org/10.1038/s41467-018-07376-7.
13. Padgett, M.; Bowman, R. Tweezers with a Twist. Nat. Photonics 2011, 5 (6), 343–348. https://doi.org/10.1038/nphoton.2011.81.
14. Brzobohaty´1, O.; Brzobohaty´1, B.; Karásek, V.; Chvátal, L.; Zemánek, P. Experimental Demonstration of Optical Transport, Sorting and Self-Arrangement Using a “Tractor Beam.” 2013. https://doi.org/10.1038/NPHOTON.2012.332.

15. Woerdemann, M.; Alpmann, C.; Esseling, M.; Denz, C. Advanced Optical Trapping by Complex Beam Shaping. Laser Photon. Rev. 2013, 7 (6), 839–854. https://doi.org/10.1002/LPOR.201200058.
16. Rubinsztein-Dunlop, H.; Forbes, A.; Berry, M. V.; Dennis, M. R.; Andrews, D. L.; Mansuripur, M.; Denz, C.; Alpmann, C.; Banzer, P.; Bauer, T.; Karimi, E.; Marrucci, L.; Padgett, M.; Ritsch-Marte, M.; Litchinitser, N. M.; Bigelow, N. P.; Rosales-Guzmán, C.; Belmonte, A.; Torres, J. P.; Neely, T. W.; Baker, M.; Gordon, R.; Stilgoe, A. B.; Romero, J.; White, A. G.; Fickler, R.; Willner, A. E.; Xie, G.; McMorran, B.; Weiner, A. M. Roadmap on Structured Light. J. Opt. 2016, 19 (1), 013001. https://doi.org/10.1088/2040-8978/19/1/013001.
17. Yang, Y.; Ren, Y. X.; Chen, M.; Arita, Y.; Rosales-Guzmán, C. Optical Trapping with Structured Light: A Review. 2021, 3 (3), 034001. https://doi.org/10.1117/1.AP.3.3.034001.
18. Bruce, G. D.; Rodríguez-Sevilla, P.; Dholakia, K. Initiating Revolutions for Optical Manipulation: The Origins and Applications of Rotational Dynamics of Trapped Particles. 2020, 6 (1). https://doi.org/10.1080/23746149.2020.1838322.
19. Friese, M. E. J.; Nieminen, T. A.; Heckenberg, N. R.; Rubinsztein-Dunlop, H. Optical Alignment and Spinning of Laser-Trapped Microscopic Particles. Nat. 1998, 394 (6691), 348–350. https://doi.org/10.1038/28566.

20. Nieminen, T. A.; Heckenberg, N. R.; Rubinsztein-dunlop, H. Optical Measurement of Microscopic Torques. J. Mod. Opt. 2001, 48 (3), 405–413. https://doi.org/10.1080/09500340108230922.
21. Sun, Q.; Dholakia, K.; Greentree, A. D. Optical Forces and Torques on Eccentric Nanoscale Core-Shell Particles. ACS Photonics 2021, 8 (4), 1103–1111. https://doi.org/10.1021/ACSPHOTONICS.0C01825.
22. Ramli, R. A.; Laftah, W. A.; Hashim, S. Core-Shell Polymers: A Review. RSC Advances. The Royal Society of Chemistry September 28, 2013, pp 15543–15565. https://doi.org/10.1039/c3ra41296b.
23. Galogahi, F. M.; Zhu, Y.; An, H.; Nguyen, N. T. Core-Shell Microparticles: Generation Approaches and Applications. Journal of Science: Advanced Materials and Devices. Elsevier B.V. 2020, December 1, pp 417–435. https://doi.org/10.1016/j.jsamd.2020.09.001.
24. Li, W.; Zhang, L.; Ge, X.; Xu, B.; Zhang, W.; Qu, L.; Choi, C. H.; Xu, J.; Zhang, A.; Lee, H.; Weitz, D. A. Microfluidic Fabrication of Microparticles for Biomedical Applications. Chemical Society Reviews. Royal Society of Chemistry August 7, 2018, pp 5646–5683. https://doi.org/10.1039/c7cs00263g.
25. Yow, H. N.; Routh, A. F. Formation of Liquid Core-Polymer Shell Microcapsules. Soft Matter. The Royal Society of Chemistry October 17, 2006, pp 940–949. https://doi.org/10.1039/b606965g.
26. Liu, Y.; Zhang, W.; Wang, H. Synthesis and Application of Core-Shell Liquid Metal Particles: A Perspective of Surface Engineering.

Mater. Horizons 2021, 8 (1), 56–77. https://doi.org/10.1039/D0MH01117G.

27. Shahabadi, V.; Madadi, E.; Abdollahpour, D. Optimized Anti-Reflection Core-Shell Microspheres for Enhanced Optical Trapping by Structured Light Beams. Sci. Rep. 2021, 11 (1), 4996. https://doi.org/10.1038/s41598-021-84665-0.
28. Zhang, Y. J.; Radjenovic, P. M.; Zhou, X. S.; Zhang, H.; Yao, J. L.; Li, J. F. Plasmonic Core–Shell Nanomaterials and Their Applications in Spectroscopies. Advanced Materials. John Wiley and Sons Inc 2021, p 2005900. https://doi.org/10.1002/adma.202005900.
29. Pietro Gucciardi, S. G.; Gillibert, R.; Magazzù, A.; Callegari, A.; Bronte-Ciriza, D.; Foti, A.; Grazia Donato, M.; Maragò, O. M.; Volpe, G.; Lamy de La Chapelle, M.; Lagarde, F.; Gucciardi, P. G. Raman Tweezers for Tire and Road Wear Micro- and Nanoparticles Analysis. Environ. Sci. Nano 2022, 9 (1), 145–161. https://doi.org/10.1039/D1EN00553G.
30. Rubinsztein-Dunlop, H.; Nieminen, T. A.; Friese, M. E. J.; Heckenberg, N. R. Optical Trapping of Absorbing Particles. Elsevier 1998, 30, 469–492.
31. Sato, S.; Harada, Y.; Waseda, Y. Optical Trapping of Microscopic Metal Particles. Opt. Lett. 1994, 19 (22), 1807–1809. https://doi.org/10.1364/OL.19.001807.
32. Jones PH, Maragò OM, Volpe G. Optical Tweezers: Principles and Applications. 2015.

33. Pellizzi, N.; Mazzulla, A.; Pagliusi, P.; Cipparrone, G. Plasmon-enhanced rotational dynamics of anisotropic core-shell polymeric-metallic microparticles. Photonics Research. 2022. https://doi.org/10.1364/PRJ.466396.
34. Neuman, K. C.; Block, S. M. Optical Trapping. Rev. Sci. Instrum. 2004, 75 (9), 2787. https://doi.org/10.1063/1.1785844.
35. Beth, R. A. Mechanical Detection and Measurement of the Angular Momentum of Light. Phys. Rev. 1936, 50 (2), 115–125. https://doi.org/10.1103/PHYSREV.50.115.
36. Simpson, S. H. Inhomogeneous and Anisotropic Particles in Optical Traps: Physical Behaviour and Applications. J. Quant. Spectrosc. Radiat. Transf. 2014, 146, 81–99. https://doi.org/10.1016/J.JQSRT.2014.04.012.
37. Simpson, S. H.; Hanna, S. Computational Study of the Optical Trapping of Ellipsoidal Particles. Phys. Rev. A - At. Mol. Opt. Phys. 2011, 84 (5). https://doi.org/10.1103/PHYSREVA.84.053808.
38. Zhang, C.; Guo, H.; Liu, J.; Zong, Y.; Li, Z.-Y. Ray-Optics Model for Optical Force and Torque on a Spherical Metal-Coated Janus Microparticle. Photonics Res. 2015, 3 (5), 265–274. https://doi.org/10.1364/PRJ.3.000265.
39. Hernández, R. J., Mazzulla, A., Provenzano, C., Pagliusi, P., & Cipparrone, G. (2015). Chiral resolution of spin angular momentum in linearly polarized and unpolarized light. *Scientific reports*, *5*(1), 1-11. https://doi.org/10.1038/srep16926

40. Manzo, C.; Paparo, D.; Marrucci, L.; Jánossy, I. Light-Induced Rotation of Dye-Doped Liquid Crystal Droplets. Phys. Rev. E - Stat. Nonlinear, Soft Matter Phys. 2006, 73 (5). https://doi.org/10.1103/PHYSREVE.73.051707.
41. Lu, D.; Gámez, F.; Haro-González, P. Temperature Effects on Optical Trapping Stability. Micromachines 2021, 12 (8), 954. https://doi.org/10.3390/MI12080954.
42. M. G. Donato, J. Hernandez, A. Mazzulla, C. Provenzano, R. Saija, R. Sayed, S. Vasi, A. Magazzù, P. Pagliusi, R. Bartolino, P. G. Gucciardi, O. M. Maragò and G. Cipparrone, Polarization-dependent optomechanics mediated by chiral microresonators. *Nat Commun* **5,** 3656 (2014). https://doi.org/10.1038/ncomms4656
43. Hernández, R. J., Provenzano, C., Mazzulla, A., Pagliusi, P., Viola, M., & Cipparrone, G. (2016). Cholesteric solid spherical microparticles: chiral optomechanics and microphotonics. *Liquid Crystals Reviews*, *4*(1), 59-79. https://doi.org/10.1080/21680396.2016.1193065
44. Volpe, G., & Petrov, D. (2006). Torque detection using Brownian fluctuations. *Physical review letters*, *97*(21), 210603. https://doi.org/10.1103/PhysRevLett.97.210603
45. Hernández, R. J., Sevilla, F. J., Mazzulla, A., Pagliusi, P., Pellizzi, N., & Cipparrone, G. (2020). Collective motion of chiral Brownian particles controlled by a circularly-polarized laser beam. *Soft Matter*, *16*(33), 7704-7714. https://doi.org/10.1039/C9SM02404B

46. Hernández, R. J., Sevilla, F. J., Mazzulla, A., Pagliusi, P., Pellizzi, N., & Cipparrone, G. (2021). Correction: Collective motion of chiral Brownian particles controlled by a circularly-polarized laser beam. *Soft Matter*, *17*(11), 3250-3253. https://doi.org/10.1039/D1SM90036F
47. Qian, H., Sheetz, M. P., & Elson, E. L. (1991). Single particle tracking. Analysis of diffusion and flow in two-dimensional systems. *Biophysical journal*, *60*(4), 910-921. https://doi.org/10.1016/S0006-3495(91)82125-7
48. Miramontes, O., DeSouza, O., Paiva, L. R., Marins, A., & Orozco, S. (2014). Lévy flights and self-similar exploratory behaviour of termite workers: beyond model fitting. *PloS one*, *9*(10), e111183. https://doi.org/10.1371/journal.pone.0111183
49. Jiang, H. R., Yoshinaga, N., & Sano, M. (2010). Active motion of a Janus particle by self-thermophoresis in a defocused laser beam. *Physical review letters*, *105*(26), 268302. https://doi.org/10.1103/PhysRevLett.105.268302
50. Chen, J., Ng, J., Ding, K., Fung, K. H., Lin, Z., & Chan, C. T. (2014). Negative optical torque. *Scientific reports*, *4*(1), 1-7. https://doi.org/10.1038/srep06386
51. Nieto-Vesperinas, M. (2015). Optical torque on small bi-isotropic particles. Optics letters, 40(13), 3021-3024. https://doi.org/10.1364/OL.40.003021
52. Cao, T., Mao, L., Qiu, Y., Lu, L., Banas, A., Banas, K., Simpson R. E. & Chui, H. C. (2019). Fano Resonance in Asymmetric Plasmonic Nanostructure: Separation of Sub-10 nm Enantiomers. Advanced

Optical Materials, 7(3), 1801172. https://doi.org/10.1002/adom.201801172

53. Cao, T., & Qiu, Y. (2018). Lateral sorting of chiral nanoparticles using Fano-enhanced chiral force in visible region. *Nanoscale*, *10*(2), 566-574. https://doi.org/10.1039/C7NR05464E

Chapter 3: Chiral Microparticles Photonics

INTRODUCTION

The core polymeric MPs have been demonstrated as good candidates for Bragg onion microresonators [1] and, properly doped with a fluorescent dye, for omnidirectional lasing [2,3]. The spherulitic structure has been investigated for several years [4-6]. Indeed, this helicoidal structure gives rise to a photonic bandgap (PBG) and an omnidirectional Bragg reflection of light in a spectral region related to its periodicity. PBG occurs in the wavelengths range between $\lambda_1 = n_o p$ and $\lambda_2 = n_e p$, where p is the pitch of the helicoidal structure, while n_o and n_e are the ordinary and extraordinary refractive indices of the polymer, respectively. By adding a proper fluorescent dye as gain medium and under an external optical pumping, lasing can be achieved [7]. Due to the band structure, the fluorescent emission is suppressed in the Bragg reflection band, and it is enhanced at the band edges. Laser light is circularly polarized according to the right- or left-handed Bragg resonator [8-10].

3.1 Background

To have a laser emission, a cavity and a gain material are needed. The cavity confines the radiation by internal reflection on a micrometric length and defines the possible modes within it. The gain material amplifies these modes and if the balance between gains and losses is positive, lasing operation is possible. A particular class of these devices is that of distributed feedback (DFB) lasers, where the whole resonator consists of a periodic structure in the laser gain medium, which acts as a distributed Bragg reflector in the wavelength range of laser action. Cholesteric liquid crystal (CLC) has a molecular arrangement that rotate around an axis making a helical

structure, which has periodic modulation of the refractive index. If the helical structure periodicity matches the radiation wavelength in the material (depending on the refractive index), a specific component of light can be reflected, see figure 1.9 spectra in the chapter 1. The position of the band gap and thus the color due to selective reflection depends on the materials parameters and on the helix pitch p. Such dependence can be written as

$$p = \frac{2\lambda_B}{n_o + n_e} \qquad \text{(eqn. 3.1)}$$

where λ_B is the wavelength corresponding to the middle of the band gap and, n_o and n_e are the ordinary and extraordinary refractive indices perpendicular and parallel to the molecular director, respectively.

The CLC is therefore working as a one-dimensional photonic crystal and has a photonic bandgap. By introducing a gain material as for example a fluorescent dye, laser emission can be obtained. The dye doped CLC acts at the same time as an optical cavity and a gain material. By pumping the CLC with an external pulsed laser with proper wavelength, single line lasing is achieved in the direction of the helical axis. The laser wavelength is located on one of the two edges of the PBG, where the photonic density of states is largest. The photon lifetime can explain this lasing mode and threshold condition [11]. In the middle of the PBG, since the propagation of photons is forbidden, the lasing is not possible and even the spontaneous emission is suppressed. On the other hand, for wavelengths outside the PBG, the photons just escape the structure because the CLC does not reflect this radiation. However, on the edge of the PBG the spontaneous emission is not suppressed on a larger extent and the structure still has enough reflectivity, thus the photon lifetime is longest. Therefore,

the optical radiation path inside the structure is also longer and as well the gain is largest. This kind of laser action is known as Bragg mode.

Another type of laser emission possible in microcavities consisting of a transparent circular or spherical object such as a disk, sphere or torus is known as whispering gallery mode (WGM). If the refractive index of the microcavity is greater than the index of the outside medium, the radiation can be trapped inside the sphere as a consequence of multiple total internal reflections and circulates close to the surface. After one circulation, if the light comes to the same point in phase, the resonant condition is obtained [7].

3.2 Lasing in polymeric microresonators

Lasing from dye doped CMPs with the AuNPs shell is investigated with the aim to explore how the photonic performances of these microresonators are affected by the nanometric metallic shell [12]. To make the microlasers, the reactive mesogen RMS03-001C is mixed with 24.5 wt% ZLI-811 chiral dopant and with 0.4 wt% of the fluorescent dye UVITEX (from NIOPIK, Russia), in order to have proper overlap between the PBG and the dye emission fluorescence spectrum [3]. The UVITEX emission spectrum is reported in figure 3.1.

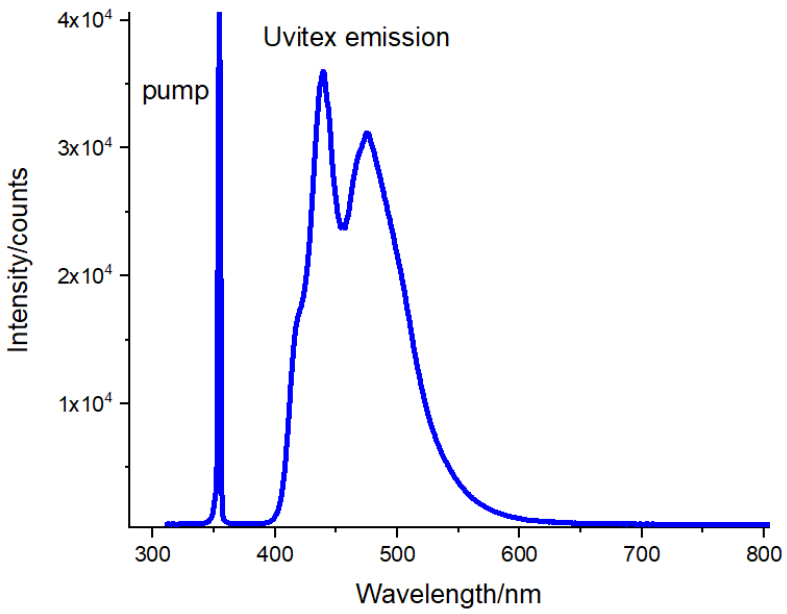

Figure 3.1 Uvitex emission spectrum in reactive mesogen RMS03-001C.

The photonic features of the undoped CMPs used in this experiment are reported in figure 1.10 in the chapter 1. The PBG edge is chosen to match with the UVITEX peak emission in order to maximize the laser operation.

The UVITEX was selected in order to limit the losses due to CMPs with and without gold shell. In fact, as described in figure 3.2, the cholesteric core has a strong absorption in the ultraviolet region, while the gold shell shows a plasmonic absorption peak as described in the chapter two. Moreover, gold exhibits a non-zero reflectivity in the blue regions [13], which contributes to reduce losses at the interface.

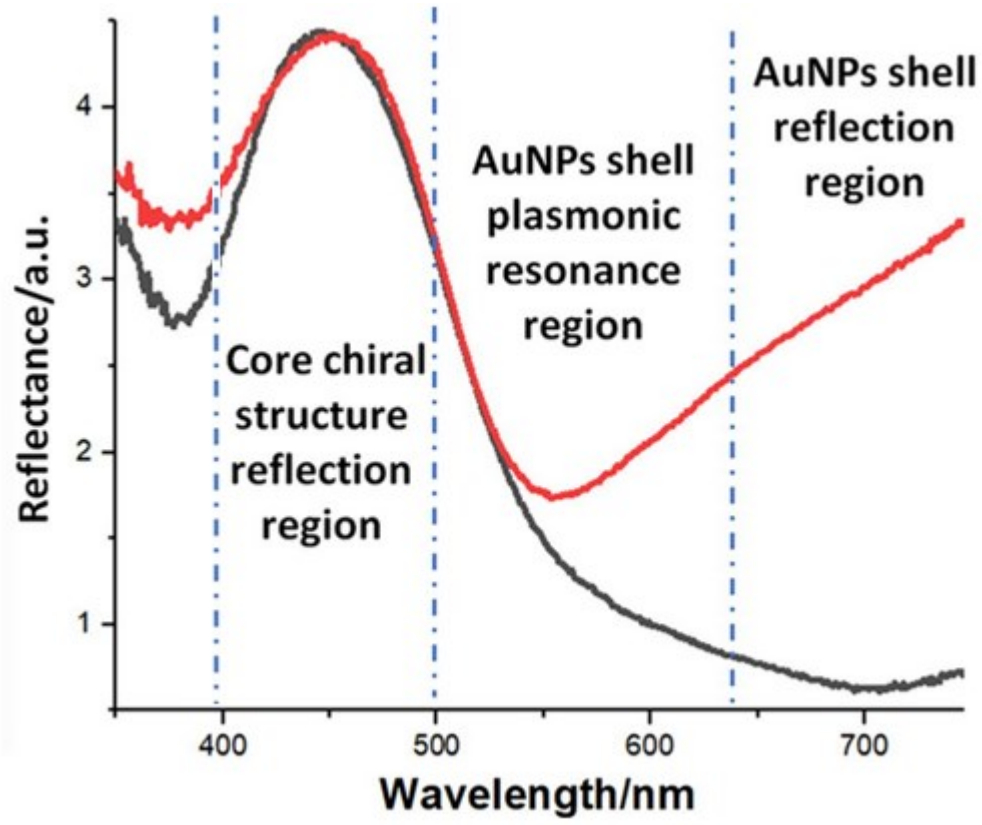

Figure 3.2 Reflection spectra of a collection of CMPs on a glass substrate with (red line) and without (black line) AuNPs shell are reported. The concentration of chiral dopant was chosen to best highlight the different photonic characteristics, due to the materials and structures constituting the CMPs.

A Q-switched Nd-YAG laser (Continuum, Surelite II) with a pulse width of 6 ns, operating at 355 nm (3rd harmonic of the fundamental wavelength) is used to pump the dye doped CMPs, through a 10 cm focal length lens to obtain a laser beam cross section of about 1 mm^2 on the specimen. The lasing experiment is performed on MPs collected on a glass substrate after water evaporation. A fiber-coupled spectrometer (AVASPEC-2048L, Avantes) with spectral resolution of 2 nm acquires the emission spectrum from the MPs by a fiber through a 20× objective. MPs are also monitored by a CCD camera that acquires images coming from a beamsplitter placed after the 20× objective (see figure 3.3).

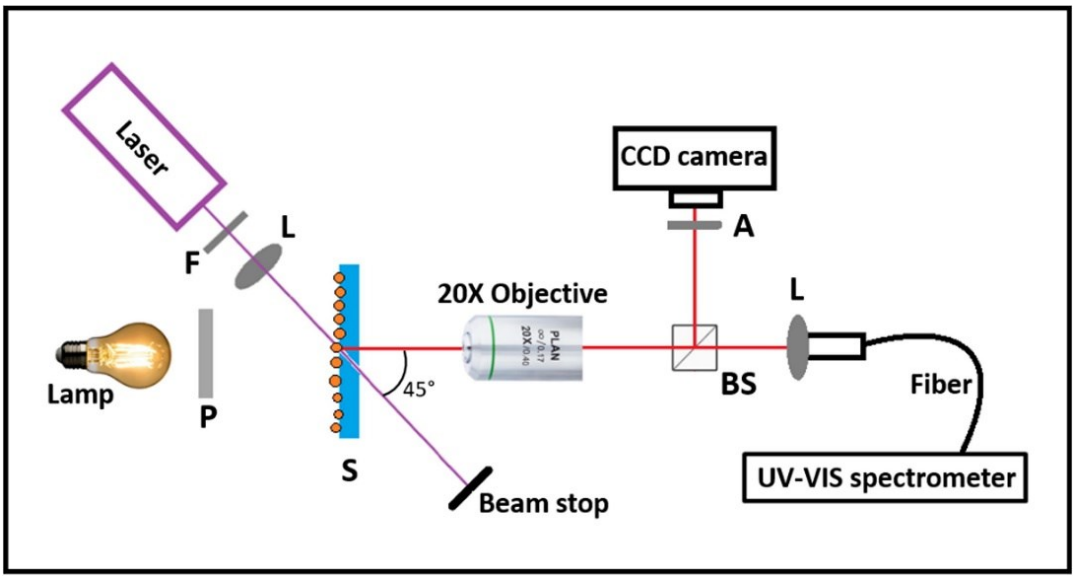

Figure 3.3 Schematic setup for lasing experiment. F: filter, L: lens, P: polarizer, A: analyzer, S: sample, BS: beamsplitter.

3.2.1 Radial Bragg Mode

In figure 3.4, the lasing spectrum from the dye doped core–shell CMPs is reported and compared to the transmission spectrum of an UVITEX doped chiral mesogen polymerized film. Lasing is generated along the radial helical axis and then propagates out of the particles in all directions. The spectrum of the emitted light shows a single laser line at 440 nm, with linewidth comparable to the pump one (the linewidth is limited by the spectrometer resolution). The lasing emission occurs at the resonance located adjacent to the long wavelength edge of the chiral polymer PBG. This feature is foreseen for films or droplets of dye doped cholesteric liquid crystals [14], [7] and proves that the observed lasing can be accounted for the PBG mode resonance of the core. Such result, in fact, is the same of the one obtained for CMPs [1]. It should be mentioned that in polymerized chiral MPs, the frozen helical structure improves the stability of the laser emission with respect to the usual CLC cells or CLC droplets, where stability problems are mainly related to cholesteric texture deformations due to the absorption of the pumping beam.

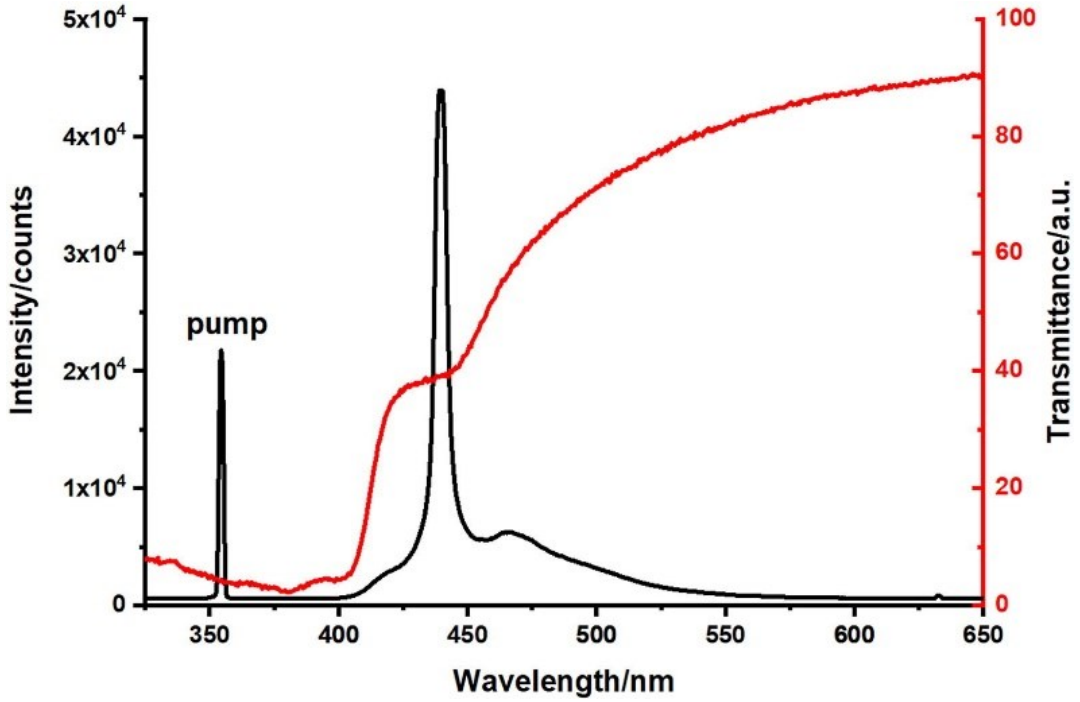

Figure 3.4 Emission intensity spectrum from the CMPs (black line), the pump beam line is also displayed at 355 nm. The fluorescence below the laser peak originates from the MPs that do not exceed the lasing threshold. Transmission spectrum of a 20 μm planar film of the polymerized dye doped chiral mesogen exploited to prepare the core–shell MPs for the lasing experiment (red line).

The threshold behavior of the pump energy density confirms the lasing regime, see Figure 3.5. Indeed, a threshold of about 10 mJ/cm^2 is estimated for both bare and core–shell dye doped CMPs. Nevertheless, some significant differences can be observed. Above the threshold, bare MPs without AuNPs shell cannot withstand pump energy density higher than 20 mJ/cm^2, being them damaged by the first laser pulse above this value, figure 3.5a. On the contrary, the pumping energy density of the core–shell CMPs can be three times higher (60 mJ/cm^2) without affecting lasing emission stability, figure 3.5b.

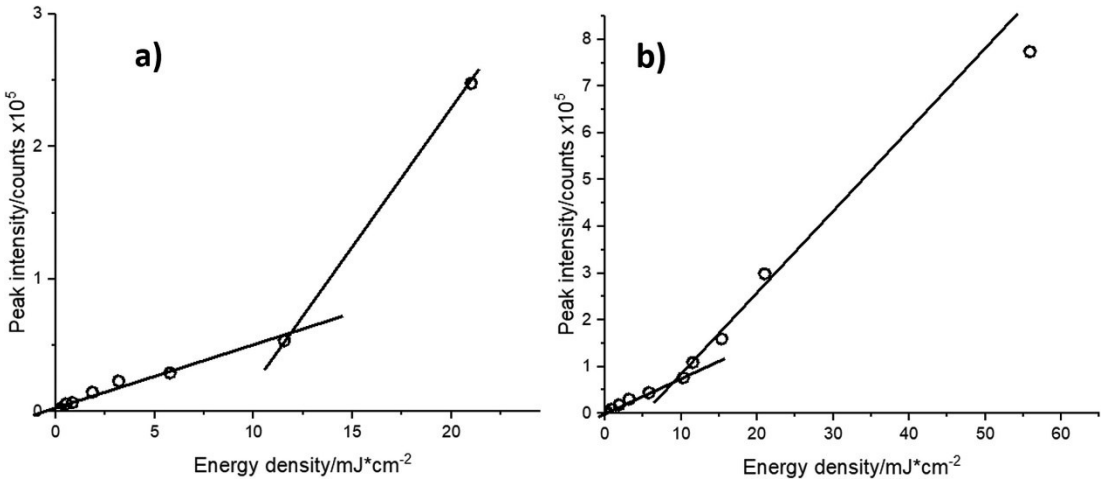

Figure 3.5 Peak intensity versus pump energy density. (a) Bare MPs. (b) MPs with AuNPs shell.

Figure 3.6 shows the emission spectrum at the first pump shot (red) for particles without (3.6a) and with (3.6b) AuNPs shell and the emission spectra at the 15th pump shot (black). Comparison of peak intensities makes evident the different stability of the two kinds of microresonators. Only fluorescence is observed for bare CMPs (figure 3.6a) after 15 pump shots, suggesting that the supramolecular helicoidal structure as well as the dye degrade. For the core–shell CMPs (figure 3.6b) lasing occurs with good efficiency even after 15 shots: laser wavelength, linewidth and peak intensity are preserved.

In the insets of figure 3.6a and b are displayed microscope images of each kind of CMPs after laser pumping below damage threshold. Comparing these images with those of as prepared CMPs (see figure 1.10) no noticeable differences are observed. On the contrary, above the damage threshold, optical images clearly show that the internal Bragg onion structure is lost and the typical Maltese cross as the blue spot disappear, figure 3.6c. In figure 3.6d we report the lasing peak intensities as a function of the n^{th} pump shot at 20 mJ/cm^2 for both kinds of CMPs. A different trend can be easily recognized: for bare CMPs without AuNPs shell the peak intensity decreases

exponentially, while the ones with AuNPs shell show a slow linear decrease and higher values of the peak intensity.

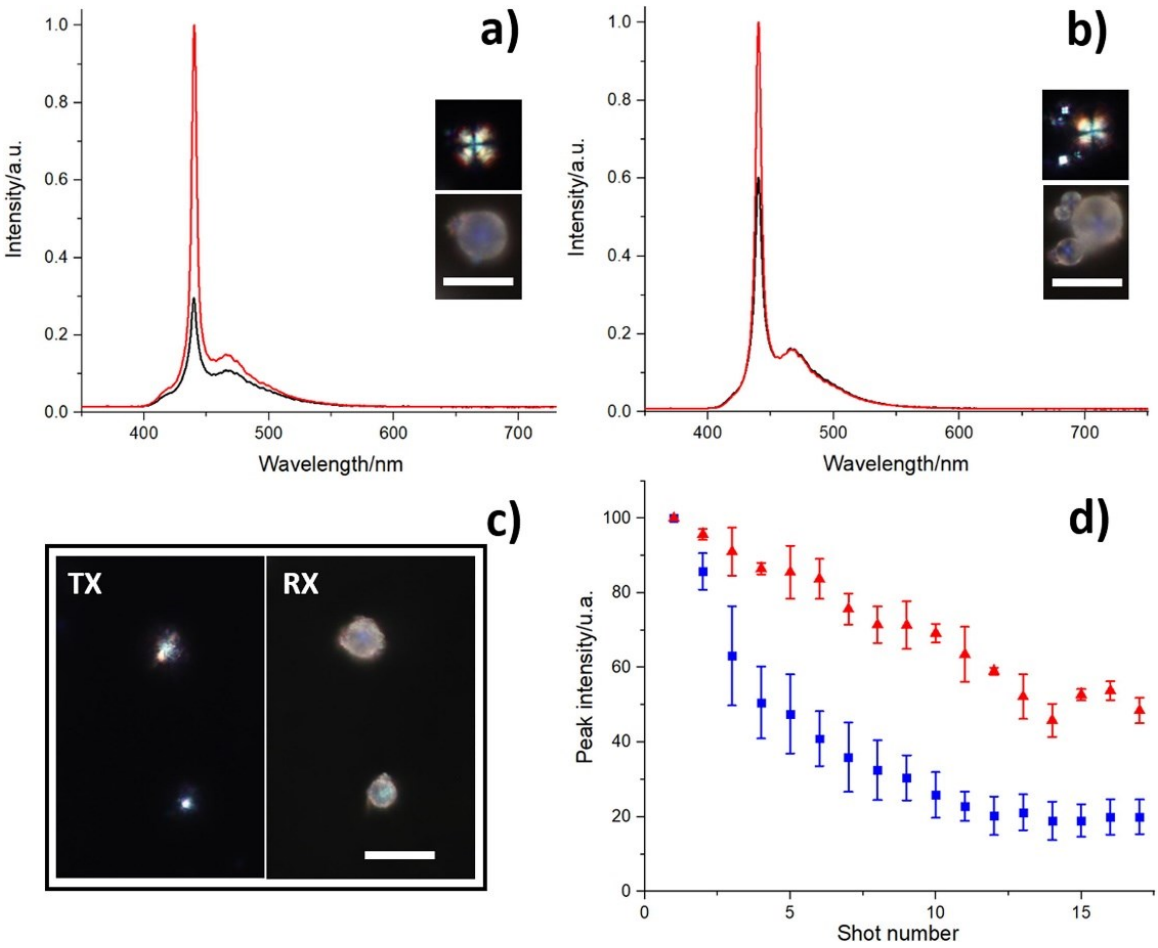

Figure 3.6 Lasing spectra acquired at the first pump pulse (red) and after 15 shots (black): a) dye doped CMPs; b) dye doped CMPs with AuNPs shell. In the inset of a) and b) are shown optical microscope images in transmission (up) and reflection (down) mode of CMPs after lasing. c) Optical microscope images (in transmission TX and reflection RX mode) of CMPs above pump damage threshold. d) Peak intensities versus pump shot repetition: blue squares are dye doped CMPs and red triangles are dye doped MPs with AuNPs shell. White scale bars are 5 μm.

3.2.2 Whispering Gallery Mode (WGM)

Radial Bragg modes are not the only optical modes in such a kind of devices, in fact also whispering gallery mode (WGM) lasing is expected for the circulating light due to total internal reflection occurring at the microresonator spherical interfaces. Indeed, the occurrence of both kind of lasing has been reported in dye doped LC MPs [1].

Nevertheless, while distributed feedback (Bragg) lasing depends on the spatial periodicity of the helicoidal supramolecular arrangement, almost uniform for all the CMPs, WGMs arise as a consequence of the total internal reflection on the surface which causes the light to remain trapped in the microparticle generating a gain in the sphere. The phenomenon depends on the size and on the difference in the refractive indices at the interface; in fact, it occurs since the internal refractive index is greater than the external one. In our case the large MPs size dispersion prevents a clear WGM lasing observation when a collection of MPs is observed, being them hidden within the background fluorescence. Instead, it is possible to observe the WGM emission if the spectrum of a single particle is measured.

For the observation of WGM CMPs containing 19.5% of chiral dopant were prepared, they exhibit a PBG centered at 640nm as shown in Figure 3.7 (black line). When 0.5% of fluorescent dye DCM (4- (dicyanomethylene)-2-methyl-6-(4-dimethylaminostyryl)-4H-pyran, by Exciton) is added to the cholesteric mixture as a gain medium, we obtain as transmission spectrum the blue line in figure 3.7, where is clearly visible how DCM absorption overlay the PBG below 550 nm wavelengths. In the same figure the emission spectrum below and above the lasing threshold are the green and the red lines, respectively, for DCM dye doped CMPs. Above the threshold laser emission modes are indicated by the red arrow for those originating from the Bragg cavity, and by the yellow arrow for the WGMs ones.

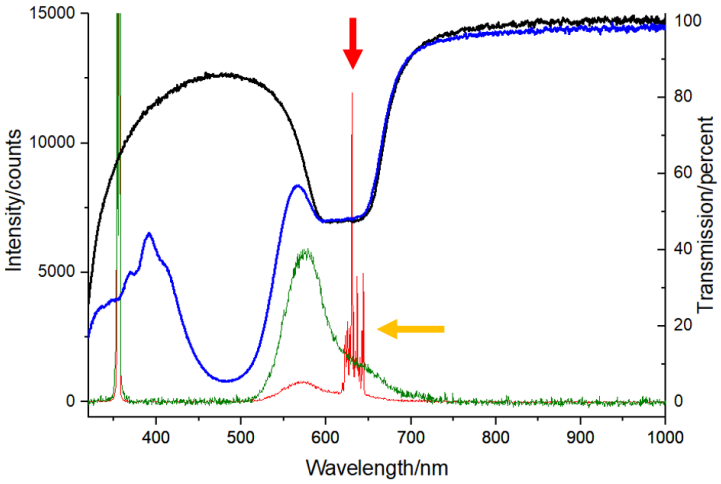

Figure 3.7 The black line is the transmission spectra of cholesteric film with 19.5% of chiral dopant. The blue line is the transmission spectra of DCM dye doped cholesteric. Fluorescence from the doped cholesteric film is the green line, while lasing emissions, from DCM dye doped CMPs is the red line. The peak at 355 nm is the pump laser line. The arrows indicate the laser emission due to Bragg cavity (red) and WGMs (yellow). The spectra are acquired using different sampling times.

Figure 3.8 displays the emission spectrum of a particle in which only WGMs are present. A significant WGMs peculiarity is revealed by the peaks analysis, i.e. they are all equidistant from each other by about 5 nm.

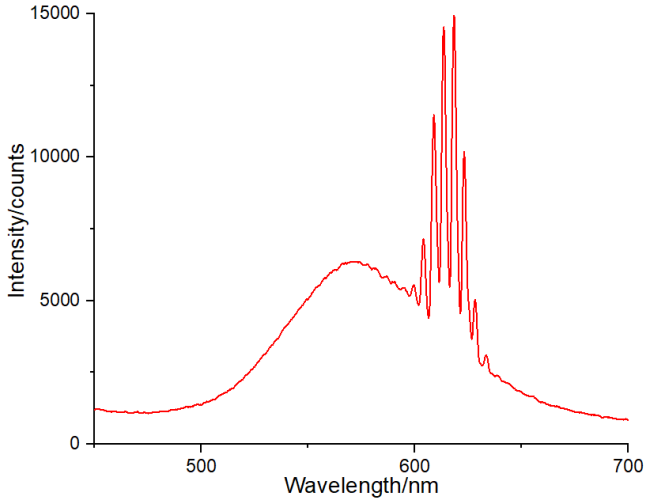

Figure 3.8 Emission spectrum of a particle in which only WGMs are present. Signature of WGMs is the equidistance amongst its peaks (5 nm).

CONCLUSION

The experimental results in figures 3.5 and 3.6 confirm that gold shells improve lasing performances by increasing stability. Such result could be explained by considering the phenomena at the air-gold and gold-polymer interfaces. The gold shell partially screens the UV pumping light due to the increased reflectance at the air interface (up to 35% for bulk gold [14]), lowering the energy that reaches the polymeric core of the MPs. As a consequence, lessening the high temperature related phenomena in the core (distortion of the supramolecular arrangement and/or dye degradation) that generally spoil dye doped cholesteric lasers and limit their applications. However, such effect does not significantly alter the lasing threshold that is almost the same in both cases (see figure3.5). The unchanged threshold could be accounted for by an increased reflectance at the polymer-gold interface of the blue light emitted by the dye within the PBG core material that compensates the reduced energy of the pump on the dye doped core-resonator, establishing the lasing condition. Nevertheless, less pump intensity and lower absorption of the polymer in the blue light region does not produce significant degradation of both the dye and the PGB supramolecular architecture, also at the UV pumping values required for the lasing conditions.

It should be noted that one of the causes that limits practical uses of lasers based on dye doped cholesteric liquid crystal in the shape of films or droplets is connected to the lasing stability and the low sustainable repetition rate. Based on this weakness, the possibility to have output power under quasi-continuous (high repetition rate) or continuous-wave (cw) operation is extremely challenging.

Due to the large flexibility in assembling such kind of soft matter-based lasers, several strategies have been proposed and investigated [15] with the aim to improve stability, however most of them are not applicable to lasers in shape of spherical MPs or

microdroplets. The results reported here suggest alternative strategies deserving to be deeply investigated with the scope to obtain omnidirectional micro-lasers operating under cw excitation. Moreover, thanks to the gold shell, the devices acquire biocompatibility, while due to the helicoidal periodic structure of the PBG material the laser light is circularly polarized, features that make these light sources an interesting tool for practical applications in biomedical fields.

The AuNPs shells modify the optical proprieties of the CMPs and clearly display plasmonic absorbance. However, the capability to control the helical pitch of the internal structures together with the NPs coverage will offer opportunities to investigate resonance phenomena, optical and photonic features.

By combining a core with proper fluorescent dye, photonic properties of our MPs are investigated. They can be used as spherical cavity (Bragg onion resonator) to develop compact-size, low threshold, and single mode microlasers with wide application opportunities in microfluidic and miniaturized lab-on-chip devices. The gold shell provides an effective strategy to further improve lasing stability exploiting the modified reflectance at the air-gold and gold-polymer interfaces, making them suitable for practical application of miniaturized laser sources with circular polarization, omnidirectional emission and possibility of continuous wave operation. The reported application will render them promising candidates for micro-optics and photonics suitable for microfluidic and biomedical application.

References

1. Humar, M., Araoka, F., Takezoe, H., Muševič, I., 2016. Lasing properties of polymerized chiral nematic Bragg onion microlasers. Opt. Express 24, 19237. https://doi.org/10.1364/oe.24.019237
2. Humar, M., Muševič, I., 2010. 3D microlasers from self-assembled cholesteric liquid-crystal microdroplets. Opt. Express 18, 26995. https://doi.org/10.1364/oe.18.026995
3. Cipparrone, G., Mazzulla, A., Pane, A., Hernandez, R.J., Bartolino, R., 2011. Chiral self-assembled solid microspheres: A novel multifunctional microphotonic device. Adv. Mater. 23, 5773–5778. https://doi.org/10.1002/adma.201102828
4. Bouligand, Y., Livolant, F., 1984. Organization of cholesteric spherulites. J. Phys. Paris 45, 1899-1923. https://doi.org/10.1051/jphys:0198400450120189900
5. Seč, D., Porenta, T., Ravnik, M., Žumer, S., 2012. Geometrical frustration of chiral ordering in cholesteric droplets. Soft Matter 8, 11982–11988. https://doi.org/10.1039/c2sm27048j
6. Hernández, R.J., Provenzano, C., Mazzulla, A., Pagliusi, P., Viola, M., Cipparrone, G., 2016. Cholesteric solid spherical microparticles: Chiral optomechanics and microphotonics. Liq. Cryst. Rev. 4, 59–79. https://doi.org/10.1080/21680396.2016.1193065
7. Humar, M., 2016. Liquid-crystal-droplet optical microcavities. Liq. Cryst. 43, 1937-1950. https://doi.org/10.1080/02678292.2016.1221151

8. Kopp, V.I., Fan, B., Vithana, H.K.M., Genack, A.Z., 1998. Low-threshold lasing at the edge of a photonic stop band in cholesteric liquid crystals. Opt. Lett. 23, 1707. https://doi.org/10.1364/ol.23.001707
9. Xiang, J., Varanytsia, A., Minkowski, F., Paterson, D.A., Storey, J.M.D., Imrie, C.T., Lavrentovich, O.D., Palffy-Muhoray, P., 2016. Electrically tunable laser based on oblique heliconical cholesteric liquid crystal. Proc. Natl. Acad. Sci. U. S. A. 113, 12925–12928. https://doi.org/10.1073/pnas.1612212113
10. Park, B., Kim, M., Kim, S.W., Kim, I.T., 2009. Circularly polarized unidirectional lasing from a cholesteric liquid crystal layer on a 1-D photonic crystal substrate. Opt. Express 17, 12323. https://doi.org/10.1364/oe.17.012323
11. Shtykov, N.M., Palto, S.P. Modeling laser generation in cholesteric liquid crystals using kinetic equations. *J. Exp. Theor. Phys.* **118,** 822–830 (2014). https://doi.org/10.1134/S1063776114040074
12. Pellizzi, N., Mazzulla, A., Pagliusi, P., & Cipparrone, G. (2022). Core-shell chiral polymeric-metallic particles obtained in a single step by concurrent light induced processes. Journal of Colloid and Interface Science, 606, 113-123. https://doi.org/10.1016/j.jcis.2021.07.143
13. Palik, E.D., San, B., New, D., London, Y., Toronto, S.T., 1991. Handbook of Optical Constants of Solids II ACADEMIC PRESS, INC. Harcourt Brace Jovanovich, Publishers.

14. Kim, D.S., Lee, W., Lopez-Leon, T., Yoon, D.K., 2019. Self-Regulated Smectic Emulsion with Switchable Lasing Application. Small 15, 1903818. https://doi.org/10.1002/SMLL.201903818

15. Chilaya, G., Chanishvili, A., Petriashvili, G., Barberi, R., De Santo, M.P., Matranga, M.A., 2006. Enhancing cholesteric liquid crystal laser stability by cell rotation. Opt. Express 14, 9939. https://doi.org/10.1364/oe.14.009939

Appendices - Production protocols

BACKGROUND

The principal material of the MPs is a mixture of reactive mesogen RMS03-001, whose molecular structures are shown in Figure A.1. This material has three main features: the first one is the hydrophobicity able to generate a water emulsion with droplet size ranging between 500 nm and 50 μm. The second is the ability to create mesophases which can be nematic or, if suitably mixed with a chiral dopant, give rise to cholesteric superstructures. The third is the UV photopolymerizability due to its composition made of a mixture of acrylate-based liquid crystal monomers as described in [1]. Moreover, the material possesses high transparency. The chiral dopants used to induce the supramolecular arrangement are R811 and S811 [2].

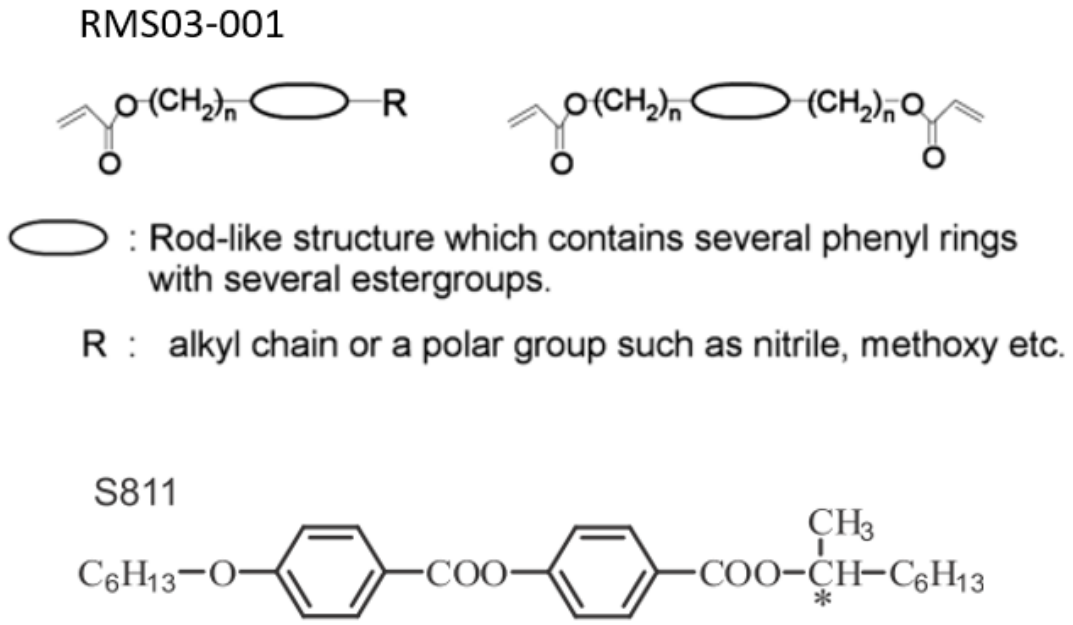

Figure A.1 Structures of reactive mesogen RMS03-001 (up) and left chiral dopant S811 (down) used in this thesis.

In figure A.2, the different steps involved in MPs production are summarized. figure A.2a) shows the PBG of the chiral RMS03-001 in polymerized film. The proper selective reflection is induced by varying the chiral dopant concentration in the reactive mesogen. By suitably shaking this chiral mixture in water an emulsion is produced, whose droplets diameter depends by frequency, temperature and duration

of the process. These droplets exhibit spherical shape and a radial cholesteric structure, which make them optically isotropic (figure A.2b). This emulsion is subsequently photopolymerized by UV exposure, activating the acylate group that freeze the supramolecular structure.

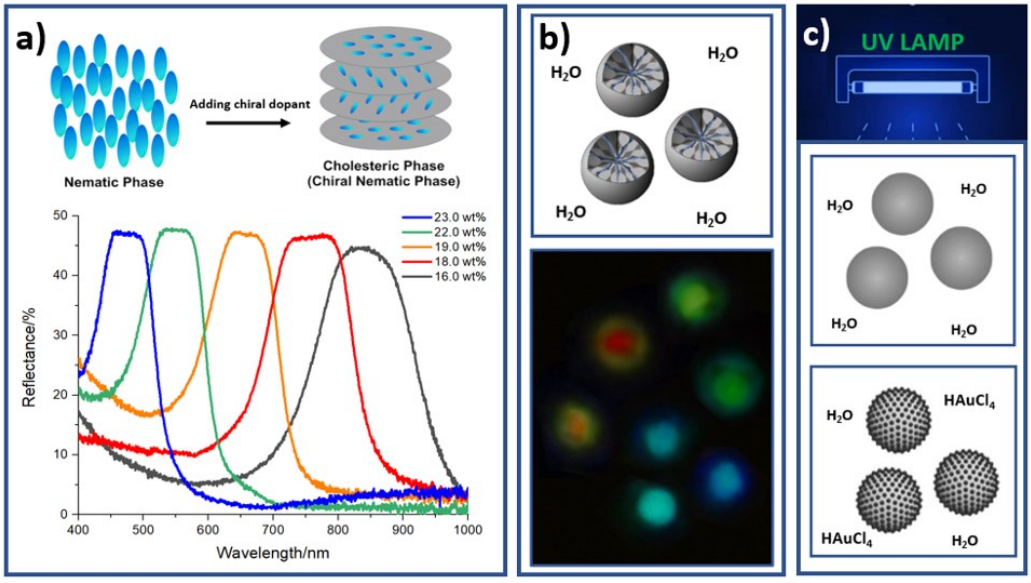

Figure A.2 Schematic a) Reflectance of reactive mesogenic films at different concentration of chiral dopant. b) Radial microdroplets emulsion in water: scheme of the internal supramolecular structure and optical microscope image. c) Polymerization by UV light of MPs in pure water and in $HAuCl_4$ /water solution.

The MPs made by only nematic monomer (without chiral dopant) exhibit ellipsoidal shape. This peculiarity is due to the bipolar internal arrangement of the nematic director, see figure A.3.

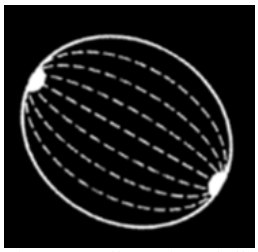

Figure A.3 Illustration of elliptical nematic bipolar microparticle

Three different production methodologies were explored in order to improve the homogeneity of both size and PBG: emulsion by shaking, emulsion by Ouzo effect and photoprecipitation. Each of these techniques allows to have MPs with advantages and drawbacks.

A.1 BARE AND CORE-SHELL PARTICLE EMULSION BY SHAKING

The MPs used in all experiments were produced by emulsion in water. The shaking provides a simple method to obtain defect-free MPs with good homogeneity in terms of PBG but suffers by a large size dispersion. The preparation procedure is summed up as follow:

1- Prepare a mixture of reactive mesogen with the desired concentration of chiral dopant. If a small amount of dye is added to the reactive mixture (0.1-2%) the result will be fluorescent microparticles.

2- Carry out a few cycles of heating and centrifugation in order to homogenize the concentration throughout the mixture. The temperature must be higher than the cholesteric phase transition one. The mixture will change from opaque to transparent.

3- A small quantity of cholesteric mixture (or pure reactive mesogen) (2-5 mg) is placed in a vial of a few ml.

4- Add 1 g of water into the vial.

5- Bring the vial to a temperature above the cholesteric transition temperature.

6- Shake the vial with a bench shaker at 20-30Hz frequency for 30 seconds, this will produce a micro emulsion of cholesteric droplet.

7- In order produce bare and core-shell liquid crystal MPs with identical core proprieties, the emulsion obtained in the previous step is divided in two vials.

8- a) In the vial with bare microparticles add 0.5g of pure water.

b) In the vial with core-shell microparticles add 0.5g of water containing 0.2, 0.5 or 1.0mM of $HAuCl_4$, to obtain the desired final volume concentration (figure A.5a).

9- Put the vial in a hermetic transparent box and purge the internal atmosphere with inert gas. This step is necessary to eliminate the oxygen which, by binding to the acrylate groups, blocks their polymerization.

10- Expose the vials under a uniform UV light with spectrum centered at 350 nm and intensity of 2 $mWcm^{-2}$, for 3-5 hours. An insufficient exposure will not lead to a total polymerization, therefore MPs will coalesce with each other; an

overexposure favors particles clusters and subsequent sedimentation. This process provides the energy necessary for the gold reduction in form of NPs adsorbed on the surface of the liquid crystal micro-droplets. Afterwards, AuNPs are trapped on the surface during the reactive core photopolymerization, forming a shell. This allows a homogeneous covering of all MPs.

11- Purify the MPs obtained by eliminating the supernatant containing uncured residues. After a brief sonication, remove the emulsion by transferring it to a new vial, avoiding transferring the residues deriving from the glass containing clusters of large particles (> 50 μm) that are not uniform as they are statistically rich of structural defects.

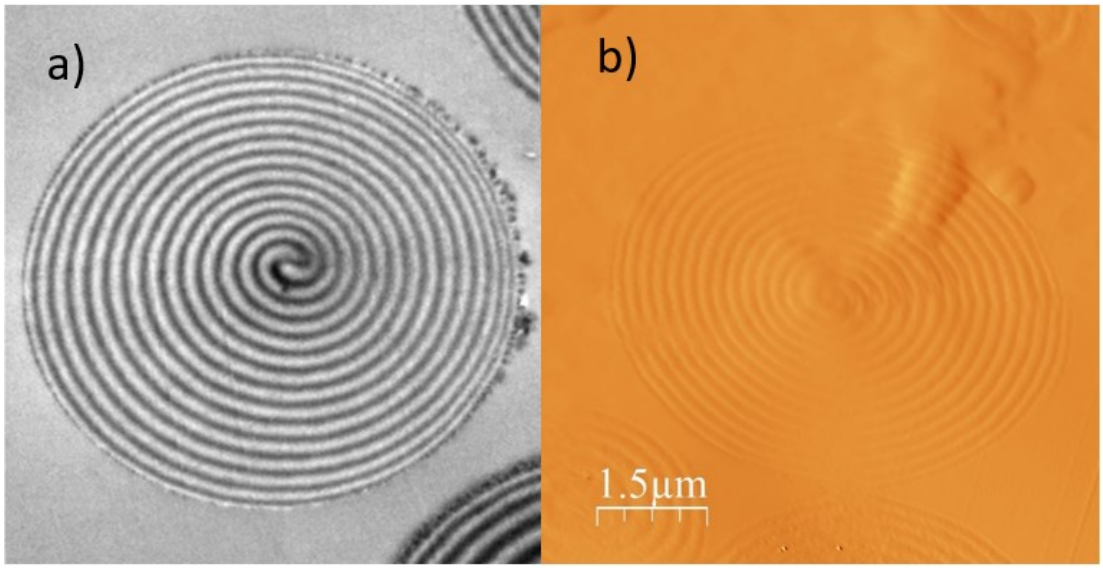

Figure A.3 TEM (a) and AFM (b) thin section image of CMPs, bar scale is the same for a) and b).

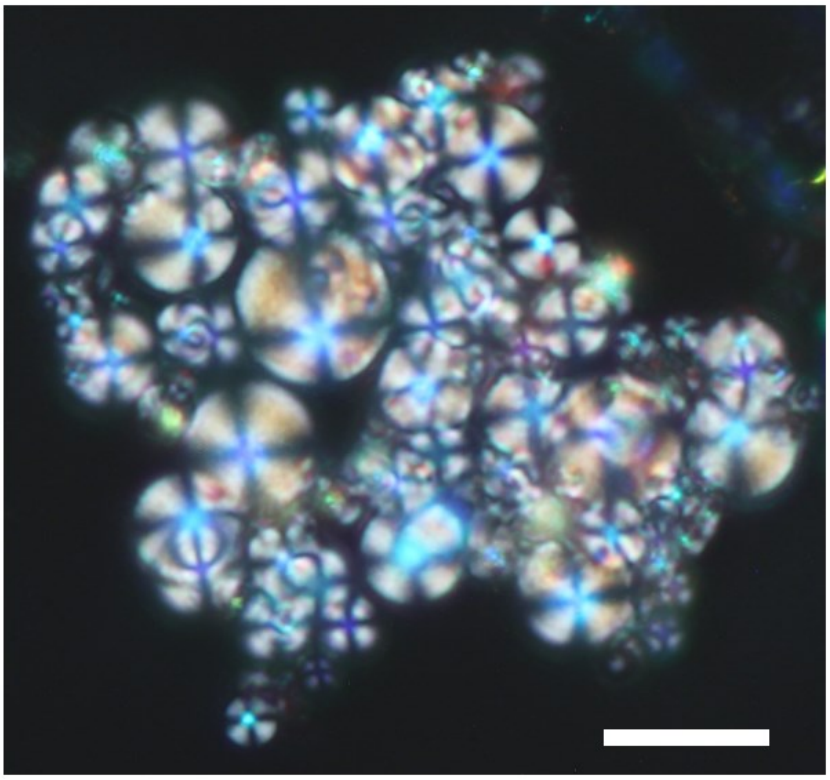

Figure A.4 Optical image of CMPs. In order to highlight all the optical characteristics of the CMPs, the image is the result of the simultaneous acquisition of both reflected and transmitted light. This operation allows to visualize both the selective reflection (blue spot in the center), and the characteristic diffraction (Maltese cross), The acquisition is achieved through crossed polarizers, the scale bar is 10 µm.

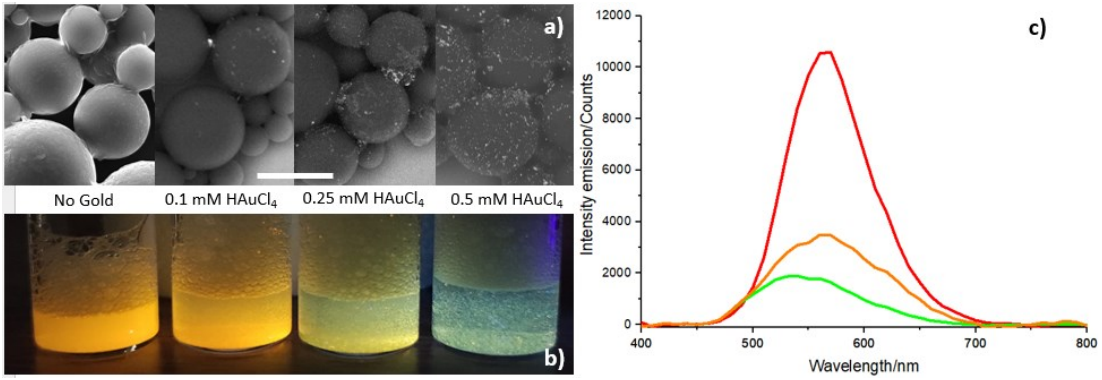

Figure A.5 a) SEM image of DCM dye doped AuCMPs as the concentration of $HAuCl_4$ varies, the scale bar is 10 µm. b) Fluorescence of a solution containing the CMPs in a). c) Emission spectra of the DCM in CMPs; Due to the plasmonic absorption at 560nm of the gold shell, an apparent shift of the emission peak is visible as the $HAuCl_4$ concentration increases (red line: no gold, orange line: 0.25 mM, green line: 0.50 mM).

A.2 PARTICLE EMULSION BY OUZO EFFECT

In order to improve characteristics such as homogeneity of the cholesteric mixture and automation of the process (for example by using microfluidic devices), emulsification by means of the Ouzo effect was explored.

This process involves the use of two solvents, the first one with the ability to dissolves the cholesteric mixture (acetone, ethyl alcohol, etc.) whilst the second not (water).

Similarly to what observed in [3] it is possible to produce a homogeneous dispersion of hydrophobic droplets in water. This is achieved by adding the reactive mesogen dissolved in the solvent into the water. On the one hand, this causes the water to solvate the solvent, and from above generates a supersaturation of the hydrophobic liquid crystal which nucleates in small drops.

The average diameter of the droplets can be controlled by changing the LC-solvent ratio at a given temperature. The numerical density of the droplets formed can be controlled independently of the diameter of the droplets by changing the amount of water added.

The uniformity of chiral doping is improved through the choice of a solvent that perfectly solvates both the reactive mesogen and the chiral molecule.

Furthermore, the reactive chiral mixture has a high intrinsic density which makes it difficult to use it in microfluidic circuits at room temperature. It is possible to overcome this problem by generating the particles starting from a solution whose viscosity is equal to the solvent one. The particles production is as follow:

1. Prepare a mixture of reactive mesogen with the desired concentration of chiral dopant.
2. Achieve a solution of reactive mixture in solvent (2%).
3. Put 30 mg of reactive mesogen solution in a vial.
4. Add 1 g of water to the vial, if the solvent is suitable for the Ouzo effect, the emulsification reaction will be instantaneous, making the solution white and opaque, see figure A.6. The yield in terms of number of emulsified droplets is higher when the solvent miscibility in water is greater.

5. Place the particles solution into a vacuum chamber to extract the solvent. This allows to not interfere with the polymerization and to set the interfacial arrangement of the particles.
6. Put the vial in a hermetic transparent box and purge the internal atmosphere with inert gas.
7. Expose the vial under UV light for 3-5 hours. As described above, this step will lead to the polymerization of the emulsified droplets.
8. Purify from residues and clusters as described in point 11 of the previous protocol.

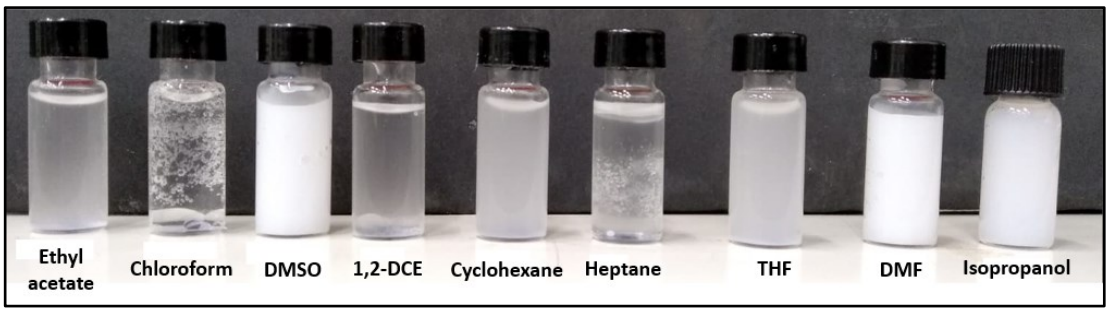

Figure A.6 Photo of emulsions for Ouzo effect using various solvents. Among these only DMSO, THF, DMF and isopropanol allow for uniform emulsification.

Some solvents preserve the chiral structure inside the particles as in the case of Tetrahydrofuran (THF), figure A.7b, this solvent also allows for good monodispersion figure A.7a and regular shape figure A.8.

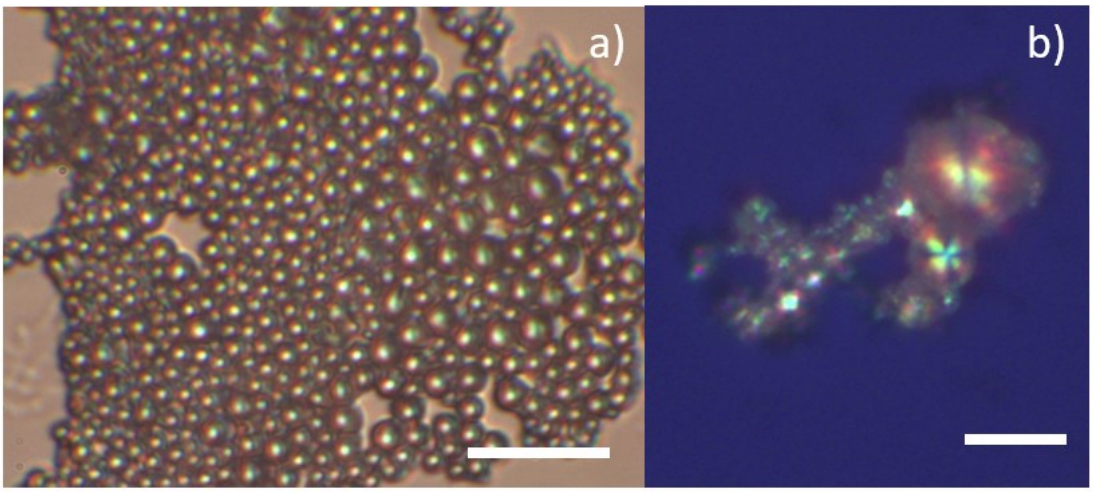

Figure A.7 Microscopic pictures of emulsions for Ouzo effect using THF. a) it is possible to see a uniform distribution of CMPs, the scale bar is 20 µm. In b) image obtained by crossing the polarizers, particles of different sizes have the typical diffraction of the chiral structure, the scale bar is 5 µm.

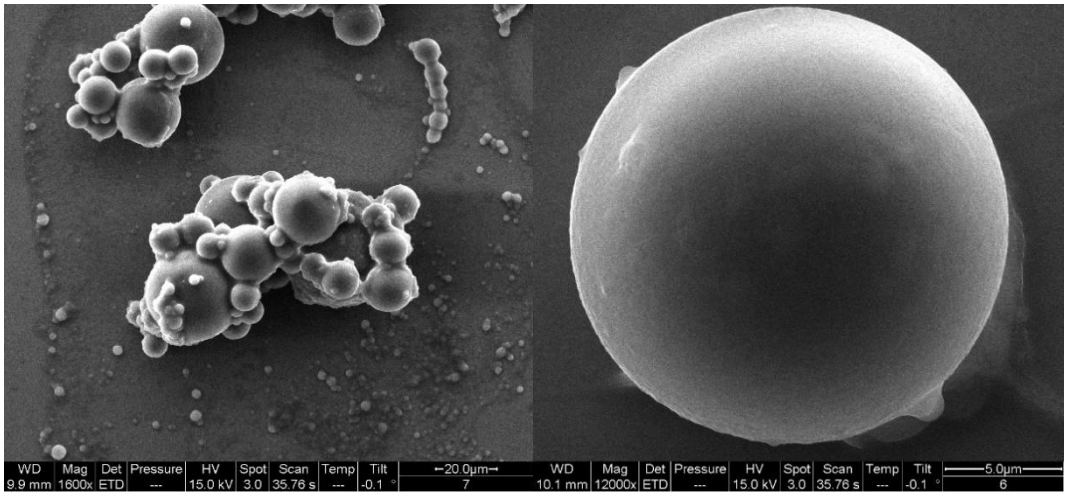

Figure A.8 SEM images of Ouzo emulsification using THF, a total miscible solvent in water.

In figure A.9 the effect of the ethyl acetate solvent is clearly shown. Since its very low solubility in water, it remains trapped in the polymerized particles giving rise to porosity phenomena.

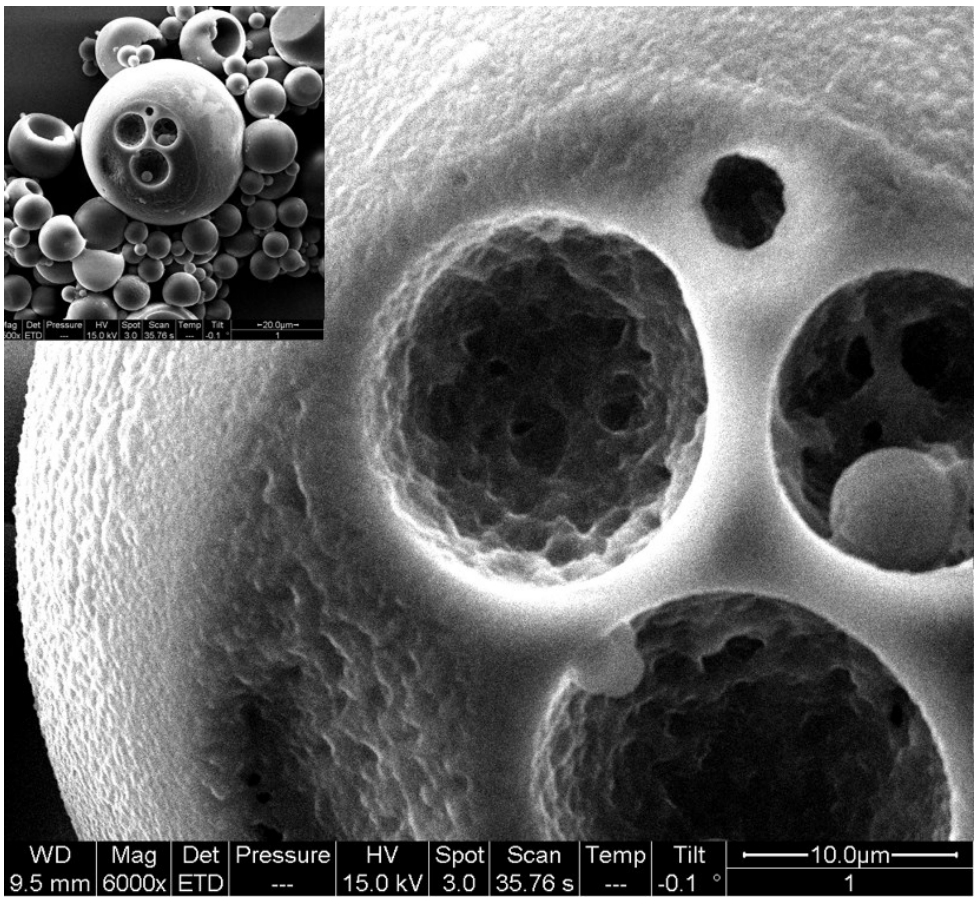

Figure A.9 SEM images of a particle using ethyl acetate, a solvent which has low solubility in water (8.3 g/100 mL at 20 °C).

A.3 NEMATIC PARTICLE BY PRECIPITATION

As seen in general for emulsion methods, it is difficult to obtain monodisperse population without the use of proper microfluidic techniques. By exploiting the photopolymerization capability and the good stability of the polymerized particles into the solvent, these were produced by photoprecipitation. As can be seen in figures A.10 (propylene glycol monomethyl ether acetate, PGMEA, used as solvent) and A.11 (ethyl alcohol) the particles produced by photoprecipitation have a high monodispersion degree. The production routine is listed here:

1. Prepare a solution of reactive mesogen in solvent (2%). Two different solvents were used, PGMEA and ethyl alcohol.
2. Put 1 g of reactive mesogen solution in a vial.
3. Place the vial in a hermetic transparent box and purge the internal atmosphere with inert gas.
4. Expose the vial under a UV light for 30 minutes. In this step free radicals in solution are obtained with consequent precipitation of insoluble nanoparticles. By following a dynamic of nucleation and growth, these initial nuclei will grow uniformly. In this phase it is possible monitoring the formation of precipitates simply following the passage of the solution from transparent to milky
5. The particles thus produced can be uniformly dispersed as for PGMEA, or aggregated in clusters when ethyl alcohol is used. In the latter case the interparticle bonds are weak and by a slight sonication the particles separate. The result is a monodispersion of sub-microparticles, as visible in figures A.10 and A.11. The average size of the distribution depends on the solvent used. The particles observed by polarizing microscopy appear birefringent.

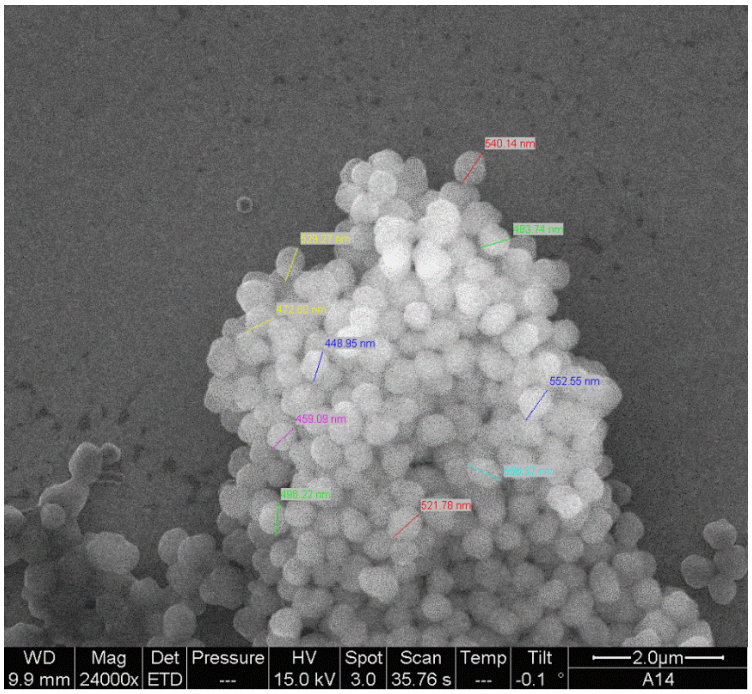

Figure A.10 SEM image of particles produced by photoprecipitation of RMS03-001 in PGMEA. The mean diameter is 510 ± 20 nm.

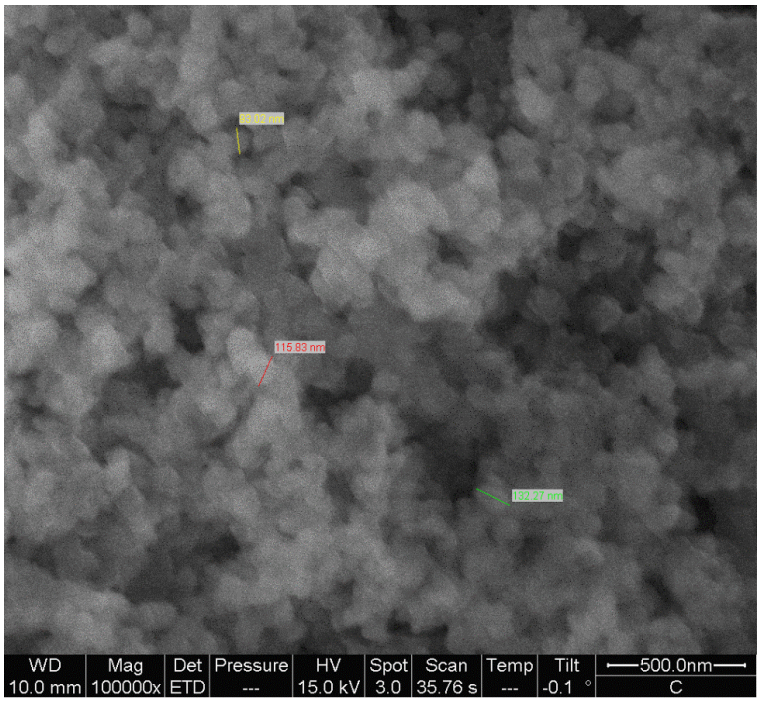

Figure A.11 SEM image of particles produced by photoprecipitation of RMS03-001 in ethyl alcohol. The mean diameter is 107 ± 13 nm.

References

1. Yamahara, M., Nakamura, M., Koide, N., & Sasaki, T. (2007). Relationship between the optical properties of immobilized liquid-crystalline film and polyimide alignment layer. *Molecular Crystals and Liquid Crystals*, *473*(1), 3-14. https://doi.org/10.1080/15421400701432420

2. Mazzulla, A., Cipparrone, G., Hernandez, R. J., Pane, A., & Bartolino, R. (2013). Self-organized chiral microspheres. *Molecular Crystals and Liquid Crystals*, *576*(1), 15-22. https://doi.org/10.1080/15421406.2013.789420

3. Vitale, S. A., & Katz, J. L. (2003). Liquid droplet dispersions formed by homogeneous liquid− liquid nucleation: "The Ouzo effect". *Langmuir*, *19*(10), 4105-4110. https://doi.org/10.1021/la026842o

Summary and Outlook

All the work of the thesis is focused on the engineering of photosensitive particles, both for photonic and optomechanical responses. The versatility offered by photoreactive mesogens, in which the refractive index is easily modulated by varying the supramolacular structure, is exploited to create polymeric microparticles with a well-defined PBG. This type of dielectric structure with a high refractive index is joined to a raspberry-like structured shell formed by gold nanoparticles. Since UV activation is exploited both for the mesogenic core polymerization and the precipitation of gold nanoparticles, the processes take place in a single step, making production and industrialization easier.

In **Chapter 1** all the particles used in the experiments are described and characterized. Furthermore, the detailed particles production protocols are reported in appendix A. The particles produced by coupling a liquid crystalline dielectric core and a gold plasmon shell exhibit photonic crystals properties. The two fundamental aspects of this technology are:

- the ability to obtain a core with different, albeit well controlled, shape, birefringence, supramolecular arrangement and PBG;
- the ease of depositing a nanoparticles-shell with photonic characteristics absent in the dielectric core.

As can be seen from graphs and images of this chapter, the particles possess a visible spectral region with high reflectivity due to the PBG, alongside a region of high plasmonic absorption.

In **Chapter 2** the opto-mechanical properties of birefringent and chiral particles are studied.

The focus of the first part is on the angular momentum transfer when these are exposed to optical tweezers made of a circularly polarized Gaussian beam. It is observed that the transfer of the normal spin momentum, expected for ellipsoidal shaped birefringent particles, changes when a gold nanoshell is present. In fact, bare microparticles are subject to:

- a scattering force that traps them in the center of the beam, due to the refractive indices difference between the internal and the external medium;

- an optical torque that sets them in rotation, which arises from the change in angular momentum brought by the circularly polarized light passing through the birefringent particle. If suitably coated with a nanometric shell made up of gold nanoparticles (raspberry-like structure), the MPs will experience further force, due to the greater reflection from the metallic shell. The latter balance the scattering force and place the particle at a certain distance from the beam center. When the coreshell microparticle is irradiated with circularly polarized light, it acquires an orbital angular momentum.

The second part of the chapter focuses on how bare chiral particles with incomplete selective reflection can display orbital motions when few of them are trapped together. This motion that has a collective nature, is successfully modeled.

In **Chapter 3** the lasing features of these microparticles are pointed out when used as resonant cavities. As already known in literature, dye doped chiral microparticles are versatile emitters of omnidirectional circularly polarized laser radiation. Unfortunately, they suffer by rapid deterioration of both structure and dye. As discussed in the chapter, the use of this shell cavities offers a noticeable improvement against degradation when compared to bare cavities. The reason is the lower effective laser threshold and an improved cavity efficiency.

List of Publication

Publications during the last triennium:

- Pellizzi, N., Mazzulla, A., Pagliusi, P., & Cipparrone, G. (2022). Core-shell chiral polymeric-metallic particles obtained in a single step by concurrent light induced processes. **Journal of Colloid and Interface Science**, 606, 113-123. https://doi.org/10.1016/j.jcis.2021.07.143

- Hernández, R. J., Sevilla, F. J., Mazzulla, A., Pagliusi, P., Pellizzi, N., & Cipparrone, G. (2020). Collective motion of chiral Brownian particles controlled by a circularly-polarized laser beam. **Soft Matter**, 16(33), 7704-7714. https://doi.org/10.1039/C9SM02404B

- Pellizzi, N.; Mazzulla, A.; Pagliusi, P.; Cipparrone, G. Plasmon-enhanced rotational dynamics of anisotropic core-shell polymeric-metallic microparticles. **Photonics Research**, 2022. https://doi.org/10.1364/PRJ.466396.